

**INVERSE OPAL SCAFFOLDS AND PHOTOACOUSTIC  
MICROSCOPY FOR REGENERATIVE MEDICINE**

A Dissertation  
Presented to  
The Academic Faculty

by

Yu Shrike Zhang

In Partial Fulfillment  
of the Requirements for the Degree  
Doctor of Philosophy in the  
Wallace H. Coulter  
Department of Biomedical Engineering

Georgia Institute of Technology  
December 2013

Copyright 2013 © by Yu Shrike Zhang

**INVERSE OPAL SCAFFOLDS AND PHOTOACOUSTIC  
MICROSCOPY FOR REGENERATIVE MEDICINE**

Approved by:

Dr. Younan Xia, Advisor  
Department of Biomedical Engineering  
*Georgia Institute of Technology*

Dr. Lihong V. Wang  
Department of Biomedical Engineering  
*Washington University in St. Louis*

Dr. Johnna S. Temenoff  
Department of Biomedical Engineering  
*Georgia Institute of Technology*

Dr. Thomas H. Barker  
Department of Biomedical Engineering  
*Georgia Institute of Technology*

Dr. Edward A. Botchwey  
Department of Biomedical Engineering  
*Georgia Institute of Technology*

Dr. L. Andrew Lyon  
School of Chemistry  
*Georgia Institute of Technology*

Date Approved: July 15, 2013

## ACKNOWLEDGEMENTS

First of all, I would like to thank my advisor, Professor Younan Xia for all his mentorship over years. Professor Xia has always provided me with valuable guidance and discussions, given me tremendous freedom in realizing research ideas, and encouraged me to share findings with the scientific community. Without him I could never imagine myself to become who I am today with so much achievement. Then I would like to express my gratitude to Professor Dong Qin for her constant support and inspiration in both academia and life, especially the Nano Research Facility (NRF) at Washington University in St. Louis, which had greatly facilitated many of my research projects. I would also like to give my special thanks to Dr. Sung-Wook Choi, now a professor at the Catholic University in the Republic of Korea, who initially introduced to me a great part of the researches that I am going to present in this work.

I am grateful to the tremendous amount of precious opportunities on collaborative efforts that I was able to experience during my doctoral studies. Particularly, I am very much honored that I had the chance to work with Professor Lihong V. Wang in the Department of Biomedical Engineering at Washington University in St. Louis, on photoacoustic tomography/microscopy, a beautiful imaging modality that he and his group have developed and perfected during the past decade. It was him who brought me into the arena of biomedical imaging, which has intrigued and inspired me so much ever since. I was also very fortunate to meet Professor Stavros Thomopoulos in the Department of Orthopaedic Surgery at Washington University School of Medicine, our

long-time collaborator, who has been a smart, patient, and encouraging mentor to me from our first acquaintance a couple of years ago.

Following these, I would like to thank all my 50 plus colleagues during the past five years for their interdisciplinary support. Specifically, I would like to thank Xin Cai, Dr. Yu Wang, Dr. Junjie Yao, Chi Zhang, Dr. Li Li, Dr. Chulhong Kim, Dr. Song Hu, Dr. Lidai Wang, and other members from the Wang lab for photoacoustic imaging, Dr. Jingwei Xie and Dr. Jianhua Zhou for general biomedical engineering, Dr. Eun Chul Cho, Dr. Yucai Wang, Dr. Weiyang Li, and Miaoxin Yang for nanomedicine, Dr. Guorong Sun, Dr. Rui Deng, and Dr. Min Suk Shim for polymer chemistry, Justin Lipner from the Thomopoulos lab for mechanical tests, Jenny Lynch for micro-computed tomography, Dr. Matthew MacEwan for animal surgery, as well as many staff members at various core facilities without whom the efficiency of my researches would have been greatly reduced, including Kristy Wendt and Kate Nelson from NRF at Washington University for electron microscopy and microtomy, Kris Hyrc and Gary London from the Alafi Neuroimaging Laboratory at Washington University School of Medicine and Andrew Shaw from the Parker H. Petit Institute for Bioengineering & Bioscience at Georgia Institute of Technology for confocal/multi-photon microscopy and Nanozoomer Digital Pathology, Bill Coleman and Marlene Scott from the Histology Core at Washington University School of Medicine, and Jim Linders from the Machine Shop at Washington University for his delicate machining techniques. Special thanks are given to administrative assistants Karen Teasdale, Lori Williams, and Hang (Josie) Liu at Washington University in St. Louis, and Shannon Sullivan, Denna Cummings and Xin (Grace) Zhao at Georgia Institute of Technology, for their generous help on various

departmental and lab matters; to Professor Shelly Sakiyama-Elbert who allowed me to freely use her fluorescence microscope for years; to Professor Donald Elbert, and Dr. Evan Scott, Mike Nichols, Casey Donahoe, Peter Nyugen, and Megan Flake in the Elbert lab who had given me warm welcome during the first few months that I ever spent in the United States; and to all the smart and diligent undergraduate students who had worked with me: Jennifer Wang from Duke University, Kevin Regan from Bates College, and Rachel Parker from Clemson University.

I am also thankful to my thesis committee, including my advisor Professor Younan Xia, as well as reading members Professors Lihong V. Wang, Johnna Temenoff, Thomas Barker, Edward Botchwey, and Andrew Lyon. They have offered warm discussions and earnest suggestions since their serving on my committee, all of which made it possible for me to satisfactorily complete the thesis work to be presented below.

Finally, I would like to express my deep appreciation to my family members and soul mate. Thank you my dear father Zhongping Zhang and mother Qingzhou Sheng who have given me your selfless and endless love during the past twenty-seven years by allowing me to pursue ideas and life out of my own curiosity. Thank you all my family members for your tolerance, patience, care, and love. At last, I would like to thank Wenying Liu, for your company, love, and support over years, and more importantly, confidence and prospect for our future.

# TABLE OF CONTENTS

	Page
ACKNOWLEDGEMENTS	iii
LIST OF FIGURES	viii
LIST OF ABBREVIATIONS	xi
SUMMARY	xiv
<u>CHAPTER</u>	
1 Introduction	1
Inverse opal scaffolds	1
Photoacoustic microscopy	5
2 Fabrication, advantages and functionalization of PLGA inverse opal scaffolds	7
Introduction	7
Fabrication of PLGA inverse opal scaffolds	9
Advantages of inverse opal scaffolds over non-uniform scaffolds	12
Precise control over physical properties of PLGA inverse opal scaffolds	18
Functionalization of PLGA inverse opal scaffolds	23
Summary	35
Experimental	36
3 Inverse opal scaffolds as a well-defined system	43
Introduction	43
The effect of pore size on progenitor cell differentiation <i>in vitro</i>	45
The effect of pore size on neovascularization <i>in vivo</i>	49
Summary	61
Experimental	62

4	Photoacoustic microscopy for tissue engineering and regenerative medicine	67
	Introduction	67
	Photoacoustic microscopy	69
	Photoacoustic microscopy of melanoma cells	73
	Photoacoustic microscopy of cells containing no pigments <i>in vitro</i>	79
	Photoacoustic microscopy of neovascularization <i>in vivo</i>	92
	Photoacoustic microscopy of scaffold degradation <i>in vitro</i> and <i>in vivo</i>	101
	Summary	114
	Experimental	115
5	Summary and future directions	122
	Inverse opal scaffolds for regenerative medicine	122
	Photoacoustic microscopy for regenerative medicine	126
	APPENDIX A: Fabrication and size parameters of inverse opal scaffolds	130
	APPENDIX B: Catalog information of materials and chemicals	131
	APPENDIX C: Related papers and manuscripts	132
	APPENDIX D: Copyright information	134
	REFERENCES	136
	VITA	154

## LIST OF FIGURES

	Page
Figure 1.1	2
Figure 1.2	3
Figure 1.3	4
Figure 1.4	6
Figure 2.1	10
Figure 2.2	11
Figure 2.3	12
Figure 2.4	14
Figure 2.5	16
Figure 2.6	17
Figure 2.7	19
Figure 2.8	20
Figure 2.9	21
Figure 2.10	25
Figure 2.11	26
Figure 2.12	27
Figure 2.13	28
Figure 2.14	30
Figure 2.15	31
Figure 2.16	33
Figure 2.17	34
Figure 3.1	46

Figure 3.2	47
Figure 3.3	48
Figure 3.4	50
Figure 3.5	51
Figure 3.6	53
Figure 3.7	54
Figure 3.8	56
Figure 3.9	57
Figure 3.10	60
Figure 4.1	70
Figure 4.2	71
Figure 4.3	74
Figure 4.4	75
Figure 4.5	76
Figure 4.6	77
Figure 4.7	80
Figure 4.8	82
Figure 4.9	83
Figure 4.10	85
Figure 4.11	86
Figure 4.12	88
Figure 4.13	89
Figure 4.14	90
Figure 4.15	93
Figure 4.16	94

Figure 4.17	95
Figure 4.18	96
Figure 4.19	97
Figure 4.20	99
Figure 4.21	100
Figure 4.22	103
Figure 4.23	104
Figure 4.24	105
Figure 4.25	106
Figure 4.26	107
Figure 4.27	108
Figure 4.28	109
Figure 4.29	111
Figure 4.30	112
Figure 4.31	113
Figure 5.1	123
Figure 5.2	124
Figure 5.3	127

## LIST OF ABBREVIATIONS

1D	one-dimensional
2D	two-dimensional
3D	three-dimensional
10xSBF	10-times concentrated simulated body fluid
ALP	alkaline phosphatase
$\alpha$ -MEM	alpha Minimum Essential Medium
ANOVA	analysis of variance
AR-PAM	acoustic-resolution photoacoustic microscopy
ATCC	American Type Culture Collection
BME	$\beta$ -mercaptoethanol
$\beta$ -TCaP	$\beta$ -tricalcium phosphate
ccp	cubic close packed
CLSM	confocal laser scanning microscope
DAB	diaminobenzidine
DAPI	4',6-diamidino-2-phenylindole
DDI	5,5'-dibromo-4,4'-dichloro-indigo
DMEM	Dulbecco's Modified Eagle's Medium
EB	embryoid body
ECM	extracellular matrix
EGM	endothelial growth medium
ESC	embryonic stem cell
FBS	fetal bovine serum
FDA	Food and Drug Administration

FITC	fluorescein isothiocyanate
GFP	green fluorescent protein
HAc	acetic acid
HAp	hydroxyapatite
HRP	horseradish peroxidase
LIF	leukemia inhibitory factor
LSD	least significant difference
LSM	laser scanning microscopy
MAP	maximum amplitude projection
micro-CT	micro-computed tomography
MRI	magnetic resonance imaging
MSCs	mesenchymal stem cells
MTT	3-(4,5-dimethylthiazol-2-yl)-2,5-diphenyltetrazolium bromide
NIH	National Institute of Health
O.C.T.	optimal cutting temperature
OCT	optical coherence tomography
OR-PAM	optical-resolution photoacoustic microscopy
OR-PAM-FCM	OR-PAM and fluorescence confocal microscopy
OR-PAM-OCT	OR-PAM and OCT
P/S	penicillin/streptomycin
PAAm	polyacrylamide
PAM	photoacoustic microscopy
PAT	photoacoustic tomography
PBS	phosphate buffered saline
PCR	polymerase chain reaction

PDMS	polydimethylsiloxane
PEG	polyethylene glycol
PET	positron emission tomography
PHEM	poly(2-hydroxyethyl methacrylate)
PI	propidium iodide
PI	propidium iodide
PLGA	poly(D,L-lactic- <i>co</i> -glycolic acid)
pNPP	p-nitrophenyl phosphate
PS	polystyrene
PVC	polyvinyl chloride
SBF	simulated body fluid
SEM	scanning electron microscopy
SW-PAM	subwavelength-resolution photoacoustic microscopy
TCPs	tissue culture plates
X-gal	5-bromo-4-chloro-indolyl- $\beta$ -D-galactopyranoside

## SUMMARY

This research centers on the fabrication, engineering, and characterization of the inverse opal scaffolds, a novel category of three-dimensional (3D) porous scaffolds made of biocompatible and biodegradable polymers, for applications in tissue engineering and regenerative medicine. The unique features of the inverse opal scaffolds include a well-ordered structure, uniform and finely tunable pore sizes, high interconnectivity, and great reproducibility.

The first part of this work focuses on the fabrication and functionalization of inverse opal scaffolds based on poly(D,L-lactic-*co*-glycolic acid) (PLGA), a U.S. Food and Drug Administration (FDA) approved biodegradable material. The advantages of the PLGA inverse opal scaffolds are also demonstrated by comparing with their counterparts with spherical but non-uniform pores.

The second part of this work shows two examples where the PLGA inverse opal scaffolds were successfully used as a well-defined system to investigate the effect of pore size of a 3D porous scaffold on the behavior of cell and tissue growth. Specifically, I have demonstrated that *i*) the differentiation of progenitor cells *in vitro* was dependent on the pore size of PLGA-based scaffolds and the behavior of the cells was determined by the size of individual pores where the cells resided in, and *ii*) the neovascularization process *in vivo* could be directly regulated by a combination of different pore and window sizes of PLGA inverse opal scaffolds when they were implanted in a mouse model.

The last part of this work deals with the novel application of photoacoustic microscopy (PAM), a volumetric imaging modality recently developed, to tissue engineering and regenerative medicine, in terms of non-invasive imaging and quantification of cells and tissues grown in PLGA inverse opal scaffolds, both *in vitro* and *in vivo*. Furthermore, the capability of PAM to monitor and quantitatively analyze the degradation of the scaffolds themselves was also demonstrated.

# CHAPTER 1

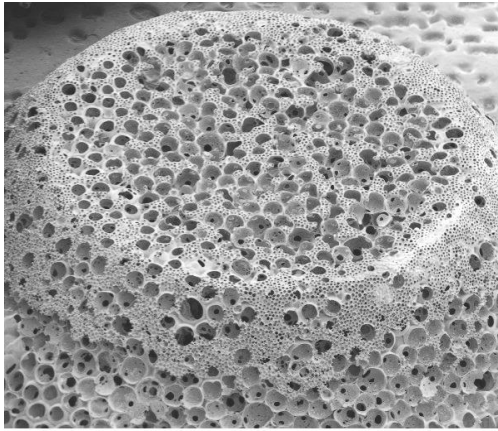
## INTRODUCTION

Tissue engineering and regenerative medicine use the combination of materials science, life sciences, medicine, and engineering to maintain, regenerate, or enhance tissue and organ functions after traumas or diseases [1-4]. Despite the tremendous progress achieved during the past few decades, two major fundamental challenges have persisted throughout. One of them is the development of suitable substrates to which the cells, tissues and extracellular matrix (ECM) molecules can adhere and respond to in a well-controlled manner. To this end, I will discuss in Section 1.1 a well-defined three-dimensional (3D) scaffolding system, the inverse opal scaffolds, including their history, applications, and my contributions. Another challenge is the development of high-capacity imaging modalities that can be used to non-invasively characterize engineered tissue constructs, especially when samples with thickness greater than several hundred micrometers are involved. In Section 1.2, I will present discussions on the solution to this issue through the use of a novel volumetric imaging modality, the photoacoustic microscopy (PAM).

### 1.1. Inverse Opal Scaffolds

For applications in tissue engineering and regenerative medicine, 3D porous scaffolds are usually advantageous in facilitating the transport of metabolites such as oxygen, nutrients, and wastes, to and from cells residing in the bulk of the scaffolds [5]. Despite many years of research, the use of 3D porous scaffolds has been largely limited to those fabricated by stochastic porogen methods (*e.g.*, salt leaching, gas foaming) that result in foams with disordered structures, as well as limited interconnectivity (Figure

1.1). Although several enabling techniques based on microfabrication have been developed for generating 3D porous scaffolds with uniform, well-controlled structures and architectures [6-8], the fabrication processes are usually complicated and time consuming, and therefore they are not readily available to the majority of biomedical engineers.



— 500  $\mu\text{m}$

**Figure 1.1.** A representative scanning electron microscopy (SEM) image showing a 3D porous scaffold with non-uniform pores.

From the historical perspective, one type of 3D porous structures termed inverse opals, have long been exploited for their applications in photonic crystals [9-12]. They are typically fabricated by a three-step process (Figure 1.2): *i*) monodispersed colloidal particles are packed into a cubic close packed (ccp) lattice and processed under thermal treatment to induce the necking between adjacent particles; *ii*) a scaffolding material is infiltrated into the void space of the lattice and cured by either freeze-drying or cross-linking; and *iii*) the original lattice is selectively sacrificed, leaving behind an inverse opal structure. These inverse opal scaffolds possess well-controlled pore sizes on the scale of nanometers to micrometers, a long-range ordered periodic structure, and uniform interconnecting windows. More importantly, they can be conveniently fabricated over

large areas/volumes and in large quantities by templating against lattices of colloidal particles with uniform sizes.

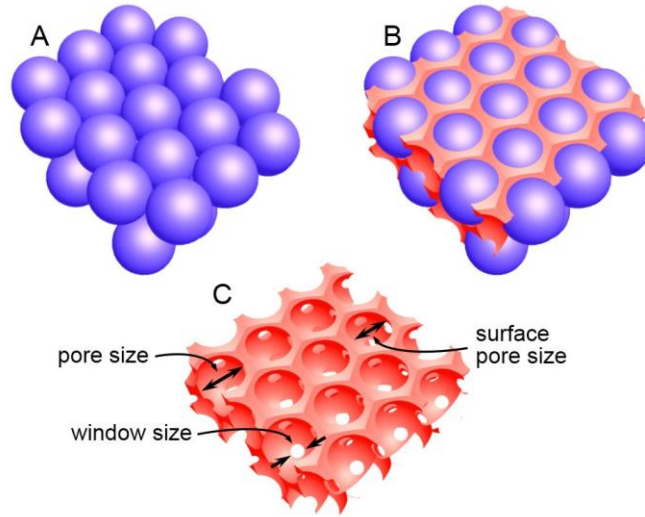


**Figure 1.2.** Schematics showing the typical fabrication process of an inverse opal scaffold.

In a pilot paper published in 2001, Ma and co-workers adopted a similar approach, and fabricated 3D porous scaffolds of biomaterials with relatively monodispersed pore sizes on the scale of a few hundred micrometers that are suitable for cell culture and tissue infiltration [13], marking the debut of inverse opal scaffolds in tissue engineering and regenerative medicine. During the last decade, inverse opal scaffolds have been used in a wide variety of applications spanning from the culture of immune cells [14, 15], the study on cell migration [16, 17], the formation of cell bodies [18-20], neovascularization [21, 22], and bone [23-25], cartilage [26, 27], and neural tissue engineering [28], among others [29-33]. In terms of materials, most of the inverse opal scaffolds up to date are fabricated from non-degradable materials or those with slow, uncontrollable degradation rates, such as chitosan, polyethylene glycol (PEG), polyacrylamide (PAAm), poly(2-hydroxyethyl methacrylate) (PHEM), and inorganic

sodium silicate and  $\beta$ -tricalcium phosphate ( $\beta$ -TCaP). Unfortunately, inverse opal scaffolds made of biodegradable materials have been rarely reported before [23, 30, 34].

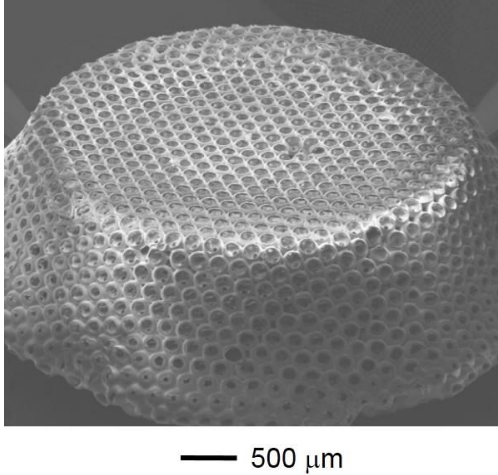


**Figure 1.3.** A representative SEM image showing a PLGA inverse opal scaffold with a uniform pore size of 200  $\mu\text{m}$ .

In my work, I have conducted a systematic study on the fabrication, functionalization, and applications of inverse opal scaffolds made from poly(D,L-lactide-co-glycolide) (PLGA, Figure 1.3). PLGA is a biocompatible polymeric material approved by U.S. Food and Drug Administration (FDA). It has relatively strong mechanical strength and more importantly, its degradation profile can be finely tuned from anywhere between a few months to a couple of years [35, 36]. The PLGA inverse opal scaffolds can be fabricated by templating against gelatin microspheres with uniform sizes produced using a custom-made fluidic device. The physical properties of the PLGA inverse opal scaffolds, including the pore size, the surface pore size, the window size, and the mechanical strength can be precisely controlled by adjusting the fabrication conditions. The matrix and/or the pores of the PLGA inverse opal scaffolds can also be easily functionalized with a number of different biomaterials such as mineral or polymer microstructures. In addition, for the first time, I have demonstrated the superior

performances of the PLGA inverse opal scaffolds as compared to their counterparts with spherical but non-uniform pores. The details of these studies will be discussed in Chapter 2. In Chapter 3, I will further elaborate on a few examples on the use of PLGA inverse opal scaffolds as a well-defined system to study the effects of different sizes on the behaviors of cells *in vitro* and tissues *in vivo*, which can hardly be achieved using scaffolds with non-uniform structures.

## 1.2. Photoacoustic Microscopy

Once a tissue construct has been engineered, it is usually necessary to evaluate the construct regarding a number of properties, such as cell viability, cell distribution, cell proliferation, and the production/spatial arrangement of ECM molecules. However, it has always been a challenge to image and characterize these 3D samples in a non-invasive and chronological manner. For example, conventional (confocal) optical microscopy and multi-photon microscopy with high resolution are hindered by their shallow penetration depth (up to approximately 500  $\mu\text{m}$ ) due to the strong optical scattering by biological tissues; magnetic resonance imaging (MRI) and X-ray micro-computed tomography (micro-CT) can penetrate deep, but they are limited by relatively low resolution (approximately 100  $\mu\text{m}$ ) and the use of ionizing irradiation, respectively. By contrast, PAM is a newly developed imaging modality that forms 3D images based on the collection of ultrasonic signals generated by an optically absorbing object when irradiated with a pulse or intensity-modulated laser (Figure 1.4) [37-39]. To date, PAM has been extensively used in label-free imaging of blood vessels *in vivo* by taking advantage of the intrinsic optical contrast of hemoglobin present in red blood cells, as well as in imaging exogenous contrasts such as metal nanoparticles and organic dyes [40, 41]. There have been essentially no prior report on the use of PAM in tissue engineering and regenerative medicine. In fact, comparing to other commonly used optical imaging modalities, PAM is

highly suited for non-invasive characterization of engineered 3D tissue constructs thanks to the much weaker scattering of ultrasound than photons in biological tissues and thus the much deeper penetration depth than pure optical imaging. Importantly, PAM can maintain relatively high and adjustable spatial resolution spanning multiple scales from organelles (submicron) in single cells to entire organs (several centimeters) [38, 39].

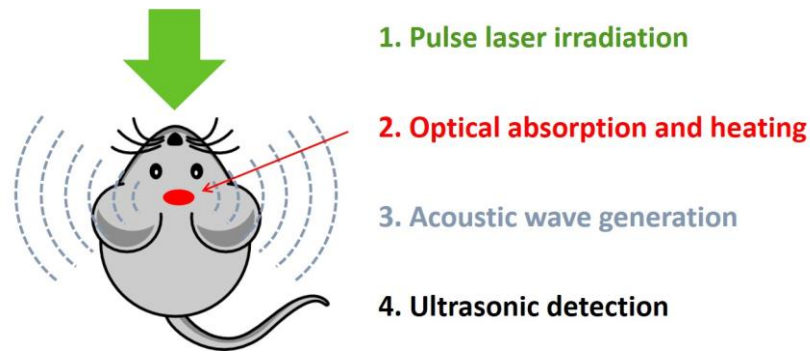


**Figure 1.4.** A schematic showing the principle of PAM.

In my work, I have pioneered the applications of multiscale PAM in tissue engineering and regenerative medicine to non-invasively monitor 3D samples based on PLGA inverse opal scaffolds, which will be elaborated in Chapter 4. Demonstrations will include *in vitro* imaging of melanoma cells containing natural dark pigments that enabled label-free PAM, as well as other normal pigment-free cell types whose absorption contrasts were enhanced by several staining techniques, such as the 3-(4,5-dimethylthiazol-2-yl)-2,5-diphenyltetrazolium bromide (MTT) staining and the colorimetric cytochemistry. The development of blood vessels inside PLGA inverse opal scaffolds *in vivo* in nude mice could also be non-invasively monitored and quantitatively analyzed instead of the conventional, invasive histology processing. Finally, the application of PAM in regenerative engineering will be further exemplified in a demonstration where the degradation of PLGA inverse opal scaffolds doped with an organic dye, MTT formazan, was non-invasively monitored by PAM.

## **CHAPTER 2**

# **FABRICATION, ADVANTAGES AND FUNCTIONALIZATION OF PLGA INVERSE OPAL SCAFFOLDS**

### **2.1. Introduction**

As discussed in Chapter 1, inverse opal scaffolds can be fabricated by templating against lattices of uniform microspheres. However, it is not always easy to obtain the templating microspheres made of desired sacrificial materials and/or with uniform sizes that are sufficiently large for subsequent biomedical applications. For example, spherical particles with uniform sizes of approximately 50–2000 nm can be conveniently produced using techniques such as dispersion polymerization for polystyrene (PS) beads [42, 43], or the Stöber process for silica beads [44-46]. But the pores of the inverse opal scaffolds fabricated from these particles would be too small for cells and tissues to penetrate. While microspheres with sizes on the scale of millimeters are also easily obtainable and commercially available, the pores of the resulting scaffolds would then, on the contrary, be too large for cells to respond. In fact, for many of the inverse opal scaffolds previously reported to have pore sizes ranging from a few tens to hundreds of micrometers, the microspheres had to be obtained by repeated sieving of samples with non-uniform sizes [13, 21, 34]. Therefore, the resulting inverse opal scaffolds typically did not have perfectly monodispersed pore sizes and structure.

To this end, I have adopted a novel and yet simple approach based on a custom-made fluidic device to fabricate microspheres with uniform sizes of low coefficient of variance [47]. Using such a fluidic device, I was able to efficiently fabricate uniform microspheres from biocompatible materials that are either hydrophilic (*e.g.*, gelatin, chitosan, and alginate) or hydrophobic (*e.g.*, PLGA and PS). The size of these

microspheres could be easily adjusted anywhere in the range of about 20–1000  $\mu\text{m}$  by using different combinations of parameters for the fluidic device.

On the other hand, despite many years of research on inverse opal scaffolds for tissue engineering and regenerative medicine, the major focus has been given on their direct applications [18, 22, 23, 26, 28, 30, 31, 48]. There are few previous reports elaborating on the advantages of the inverse opal scaffolds, or how the physical properties of the inverse opal scaffolds can be precisely engineered. Actually, these two subjects are very important in forming the fundamental arguments why the inverse opal scaffolds are indeed a better choice than non-uniform scaffolds for applications in tissue engineering and regenerative medicine.

In this Chapter, I will firstly discuss in Section 2.2 the production of uniform gelatin microspheres using a fluidic device and the fabrication of PLGA inverse opal scaffolds by templating against lattices of gelatin microspheres. In Sections 2.3, I will present a few studies that compared the PLGA inverse opal scaffolds with their counterparts which have spherical but non-uniform pores, in terms of reproducibility among different batches of fabrication, diffusion of macromolecules, *in vitro* cell distribution, and *in vivo* neovascularization. In Section 2.4, I will elaborate on the important issue that how the physical properties, including the pore size, the surface pore size, and the window size of a PLGA inverse opal scaffold, could be individually, finely tuned by adjusting the fabrication conditions. Such precision in the control over the physical properties of a scaffold can otherwise, never be achieved for scaffolds with non-uniform pores and structures. Finally, I will show in Section 2.5 that, both the polymer backbone and the pore space of the PLGA inverse opal scaffolds could be conveniently functionalized by a variety of biomaterials, including mineral nanoparticles and polymer microstructures. Such functionalization could thus provide the inverse opal scaffolds with a broad capability for their use in different applications in tissue engineering and regenerative engineering.

## 2.2. Fabrication of PLGA Inverse Opal Scaffolds

The fabrication of PLGA inverse opal scaffolds is dependent on the successful production of gelatin microspheres with uniform diameters, which can be realized by using a custom-designed fluidic device. Figure 2.1A shows a schematic of the fluidic device [47]. The device is constructed by firstly inserting a bent syringe needle (shown in dark gray) into a glass microcapillary (pink), which is then inserted into a poly(vinyl chloride) (PVC) tube (yellow). In a typical process, the inner discontinuous phase is comprised of gelatin aqueous solution and is injected via the syringe needle, whereas the outer continuous phase is toluene containing Span<sup>®</sup> 80 (approximately 3 vol.%) as the surfactant and is injected via the PVC tube. The uniform droplets of gelatin will then form at the tip of the syringe needle, flow along the glass microcapillary and are collected in a tall beaker containing the continuous phase in an iced water bath under gentle magnetic stirring. The gelatin droplets are stirred for 12–36 h to allow water to completely evaporate, and the solidified gelatin microspheres are collected by filtrating/washing against a filter paper with methanol and are usually stored in methanol until use.

The size of the gelatin microspheres is dependent on several parameters. The first set of parameters include the flow rates of the two phases. The size of the droplets increased when the flow rate of the inner discontinuous phase (gelatin aqueous solution) was increased. On the contrary, the size of the droplets decreased with increasing flow rate for the outer continuous phase (toluene plus Span<sup>®</sup> 80) due to an increased shear stress. The second set of parameters are the diameters of the syringe needle and the glass microcapillary, which are both positively correlated with the size of the gelatin microspheres produced. Thirdly, the concentration of the gelatin solution is also of importance: the higher the concentration is, the larger the gelatin microspheres are. By multiplexing these parameters, gelatin microspheres with desired sizes can be obtained. Figure 2.1B shows gelatin microspheres with uniform sizes of approximately 100, 200,

300, and 500  $\mu\text{m}$  made with the following combinations of parameters: 5, 10, 10, and 10 wt.% gelatin solutions, 30G, 26G, 26G, and 23G needles, and glass microcapillaries with inner diameters of 400, 500, 700, and 1500  $\mu\text{m}$ ; the flow rates were maintained constant at  $0.05 \text{ mL min}^{-1}$  for the inner discontinuous phase and  $0.2 \text{ mL min}^{-1}$  for the outer continuous phase in all cases.

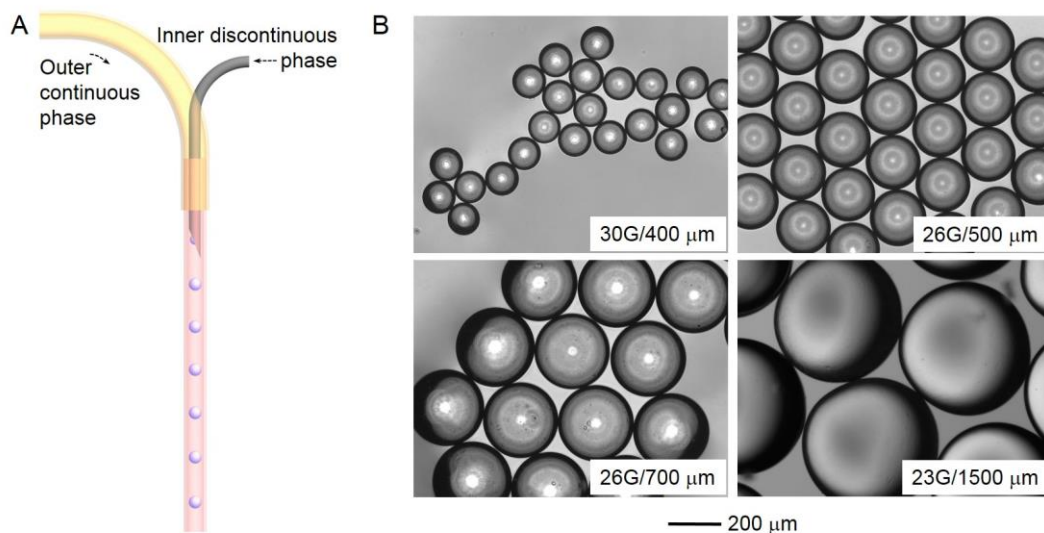


**Figure 2.1.** A) A schematic showing the fluidic device used for fabricating gelatin microspheres. The device is made of a syringe needle (dark gray), a glass microcapillary (pink) and a PVC tube (yellow). The inner discontinuous phase is an aqueous solution of gelatin at a specific concentration and the outer continuous phase is toluene containing approximately Span-80<sup>®</sup> (3 vol.%). The flow rates of the two phases are independently adjusted with syringe pumps. B) Transmission optical micrographs showing gelatin microspheres with uniform sizes of approximately 100, 200, 300, and 500  $\mu\text{m}$  that were fabricated by using combinations of needles and glass microcapillaries with different sizes (as indicated in the images). The concentrations of gelatin solution were 5, 10, 10, and 10 wt.%, respectively, and the flow rates were maintained at  $0.05 \text{ mL min}^{-1}$  for the inner discontinuous phase and  $0.2 \text{ mL min}^{-1}$  for the outer continuous phase in all cases.

The PLGA inverse opal scaffolds could then be fabricated by templating against lattices of gelatin microspheres with uniform sizes. Figure 2.2 shows SEM images of a typical fabrication process step-by-step (also refer to Figure 1.2 in Chapter 1). The gelatin microspheres were firstly packed into a ccp lattice and treated at an elevated temperature of over 60 °C in methanol to induce the necking between adjacent gelatin microspheres (Figure 2.2A). The lattice was then carefully retrieved and placed on a filter paper to allow methanol to evaporate completely. The scaffolding material, PLGA, was dissolved in 1,4-dioxane, which at the same time is a non-solvent for gelatin. Such a solution was infiltrated into the void space of the gelatin lattice, with extra solution being removed by wiping against a filter paper. The lattice containing PLGA solution was immediately transferred to a freezer at -20 °C for at least 2 h and then freeze-dried overnight (Figure 2.2B). The pellet was subsequently immersed in ethanol under mild vacuum until all the air bubbles trapped inside had been removed. Finally, the gelatin lattice was selectively removed by immersing the pellet in a water bath heated at 43 °C under gentle stirring for 3–4 h, leaving the PLGA inverse opal scaffold with uniform pore sizes and a well-ordered structure (Figure 2.2).

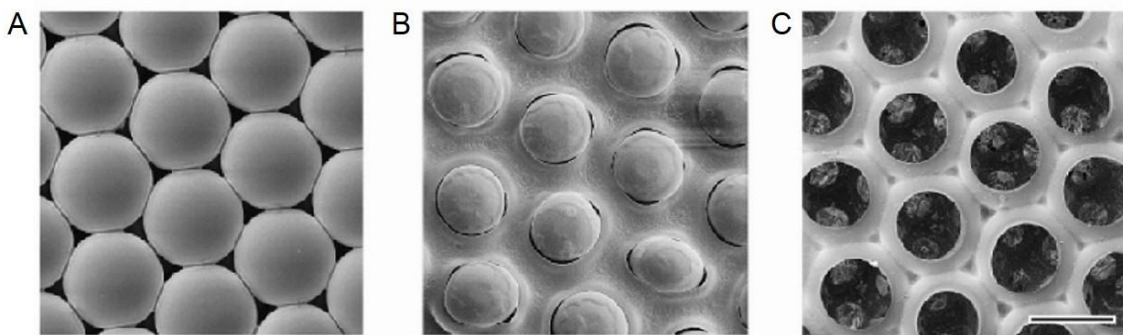


**Figure 2.2.** SEM images showing the samples involved in a typical fabrication process of a PLGA inverse opal scaffold: A) a ccp lattice of gelatin microspheres, B) a lattice filled with a PLGA solution in 1,4-dioxane followed by freeze-drying, and C) a PLGA inverse opal scaffold. Scale bar: 200  $\mu\text{m}$ .

### 2.3. Advantages of Inverse Opal Scaffolds over Non-uniform Scaffolds

In order to exemplify the advantages of the PLGA inverse opal scaffolds, I chose a class of control scaffolds that are also composed of spherical pores but with random pore sizes and limited interconnectivity [49]. The fabrication process for these non-uniform scaffolds was very similar to that for inverse opal scaffolds except that the templating gelatin microspheres had different sizes in the range of approximately 20–300  $\mu\text{m}$ . The gelatin microspheres with polydispersed sizes were produced using the same fluidic device as described earlier by continuously changing the flow rates during fabrication. Therefore, these non-uniform scaffolds can be considered as an ideal counterpart to the inverse opal scaffolds, whereas they also nicely represent the large variety of scaffolds with random structures fabricated using stochastic porogen methods.

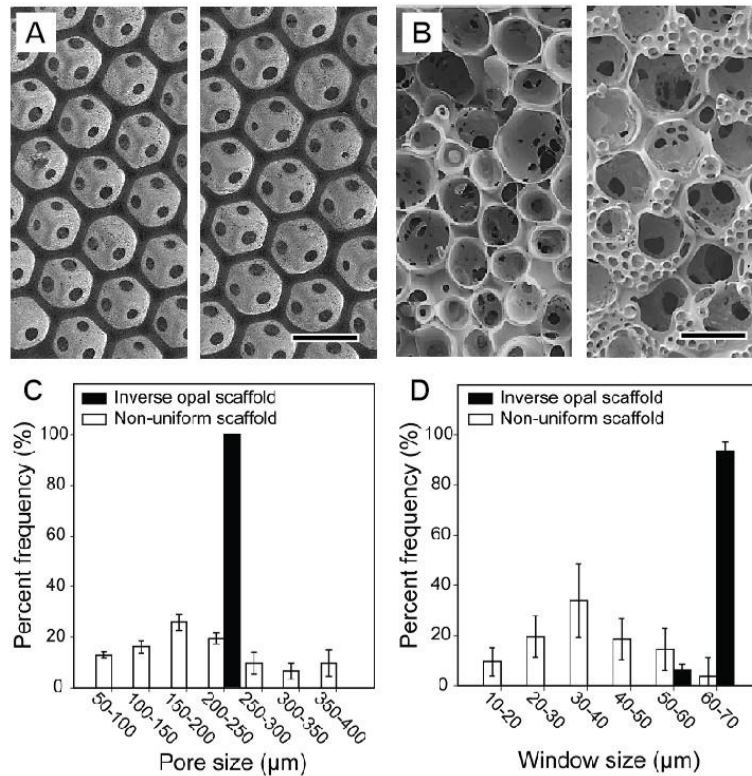


**Figure 2.3.** A, B) SEM images showing (A) PLGA inverse opal scaffolds and (B) PLGA non-uniform scaffolds fabricated in two separate batches. Scale bars: 200  $\mu\text{m}$ . C, D) Quantitative

*evaluation of the distribution of (C) pore size and (D) window size for PLGA inverse opal scaffolds (pore size: 205  $\mu\text{m}$ ) and non-uniform scaffolds (average pore size: 202  $\mu\text{m}$ ).*

One of the most important advantages of the inverse opal scaffolds lies in their extraordinary reproducibility. Figure 2.3A shows SEM images of PLGA inverse opal scaffolds from two different batches of fabrication. As expected, due to the unique ccp packing of the templating gelatin microspheres, the inverse opal scaffolds could be readily reproduced with minimum variations in pore size and structure. By contrast, the structures of the two PLGA non-uniform scaffolds were hardly comparable at all, although the average pore sizes of the scaffolds could still be maintained approximately on the same order (Figure 2.3B). In another comparison, two sets of scaffolds were fabricated: PLGA inverse opal scaffolds with a pore size of 205  $\mu\text{m}$ , and PLGA non-uniform scaffolds with an average pore size of approximately 200  $\mu\text{m}$ . As seen from the quantitative analyses (Figure 2.3, C and D), the inverse opal scaffolds had pores with a single size of 205  $\mu\text{m}$  and an average window size of  $66 \pm 7 \mu\text{m}$ ; however, the non-uniform scaffolds exhibited a wide distribution in pore sizes (average pore size:  $202 \pm 94 \mu\text{m}$ ) and a relatively small average size ( $36 \pm 22 \mu\text{m}$ ) of interconnecting windows, both of which were at the same time also variable among different batches of fabrication. In a sense, even the ultimate tissues to be engineered with the scaffolds do not necessarily require great homogeneity, the use of uniform scaffolds with reproducible physical properties would, at least, enable biomedical engineers to faithfully reproduce their results across experimental groups. The high reproducibility will also be significant when applying these tissue-engineered constructs to clinical settings, where the generation of on-shelf products with consistent quality is a prerequisite.

In addition to the reproducibility, I next examined the diffusion of macromolecules through the scaffolds. Fast diffusion is one of the most critical capabilities that a 3D scaffold should provide in order to maintain high viability for the

cells residing in the bulk of the scaffold. A custom-made flow device was constructed using two 50-mL centrifuges tubes and a fixation ring for the scaffold (Figure 2.4A). Fluorescein isothiocyanate (FITC)-dextran with a molecular weight of 40 kDa was used as a model macromolecule whose size resembles those of common bio-macromolecules. As depicted in Figure 2.4B, while the diffusion rate of FITC-dextran for the PLGA inverse opal scaffolds (pore size: 205  $\mu\text{m}$ ) was nearly comparable to that for the control where no scaffolds were present, the rate dropped by nearly a half for the PLGA non-uniform scaffolds (average pore size: 202  $\mu\text{m}$ ).

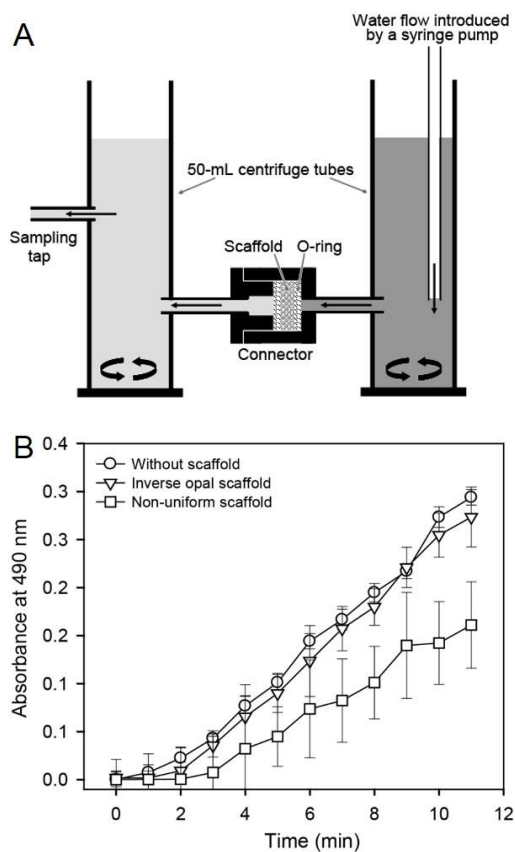


**Figure 2.4.** A) A Schematic showing a custom-made flow device for testing the diffusion of macromolecules through a scaffold. B) A plot showing the diffusion rates of FITC-dextran through PLGA inverse opal scaffolds, non-uniform scaffolds, and control without any scaffolds ( $n = 3$  in all cases).

Such difference in the diffusion rate of FITC-dextran for the scaffolds could be attributed to the much higher interconnectivity in the structure of the inverse opal scaffolds as provided by their uniform windows between all adjacent pores (Figure 2.3). In comparison, for the non-uniform scaffold, while some adjacent pores had large interconnecting windows, many regions only possessed very small windows or even no interconnectivity at all (Figure 2.3), leading to hindered transport of macromolecules through these pores as well as the entire scaffold. It is further noted that the standard deviation ( $n = 3$ ) for the non-uniform scaffolds at each time point was remarkably larger than that for the inverse opal scaffolds, again indicating better reproducibility in structure for the inverse opal scaffolds than the non-uniform scaffolds.

The inverse opal scaffolds should also facilitate the diffusion and/or the migration of cells because of their uniform structure and high interconnectivity. To test this hypothesis, I seeded NIH/3T3 fibroblasts in the PLGA inverse opal scaffolds and non-uniform scaffolds and compared the distribution of the cells at 7 days post seeding via a spinner flask. Figure 2.5, A and B shows superimposed fluorescence/bright-field optical micrographs of cells grown in an inverse opal scaffold and a non-uniform scaffold, respectively. The top half of each scaffold was cut off to expose the middle plane of the scaffold (about 500–700  $\mu\text{m}$  from the surface of the scaffold). It could be observed that, while the inverse opal scaffold supported homogeneous distribution of cells across the entire volume of the scaffold due to its uniform interconnecting windows that facilitated the transport of cells at the time of seeding and the subsequent migration of cells during culture, cell distribution was entirely random in the non-uniform scaffold, presumably due to the limited interconnectivity in certain regions of the non-uniform scaffold that prevented efficient cell seeding and migration. The quantitative analyses of cell distribution in each scaffold are shown in Figure 2.5, C and D.

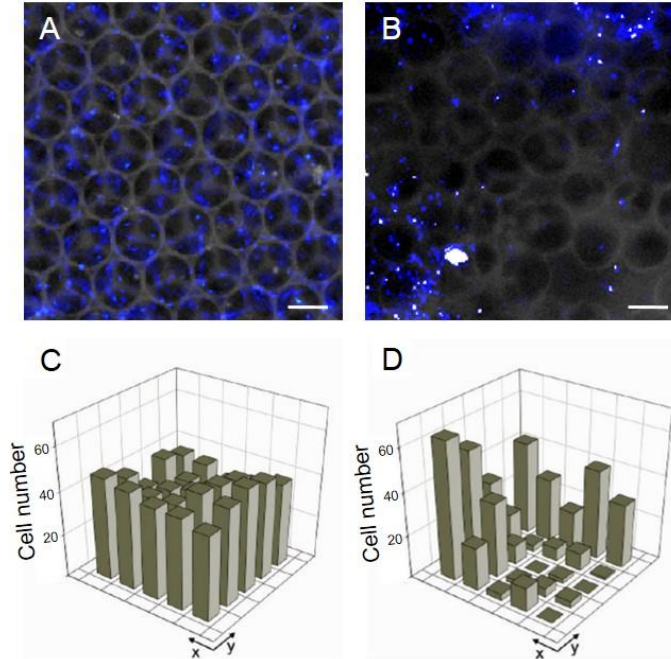


**Figure 2.5.** A, B) Fluorescence micrographs showing the distribution of NIH/3T3 fibroblasts in a PLGA inverse opal scaffold and a PLGA non-uniform scaffold, respectively, after 7 days of culture. The nuclei of the cells were stained in blue. Scale bars: 200  $\mu\text{m}$ . C, D) Quantitative analysis showing the distribution of the cells in the two types of scaffolds, respectively.

Besides *in vitro* experiments, I also compared the effect of uniformity of the scaffolds *in vivo*. In a preliminary assessment, PLGA inverse opal scaffolds with a pore size of 200  $\mu\text{m}$  and non-uniform scaffolds with an average pore size of approximately 200  $\mu\text{m}$  were implanted subcutaneously at the dorsal sides of nude mice [50]. At 4 weeks post implantation, the ingrowth of blood vessels into the scaffolds were examined and representative photographs are shown in Figure 2.6, A and B. Similar to the results from *in vitro* cell distribution, the blood vessels could develop and completely infiltrate the entire volume of the inverse opal scaffold, thanks to the high interconnectivity between adjacent pores that supported the invasion of blood vessels (Figure 2.6A). For the non-uniform scaffold (Figure 2.6B), although top right corner was well-vascularized, very few

blood vessels could be observed in the remaining region (bottom left), which again, could be attributed to the low interconnectivity of the pores in such a region.

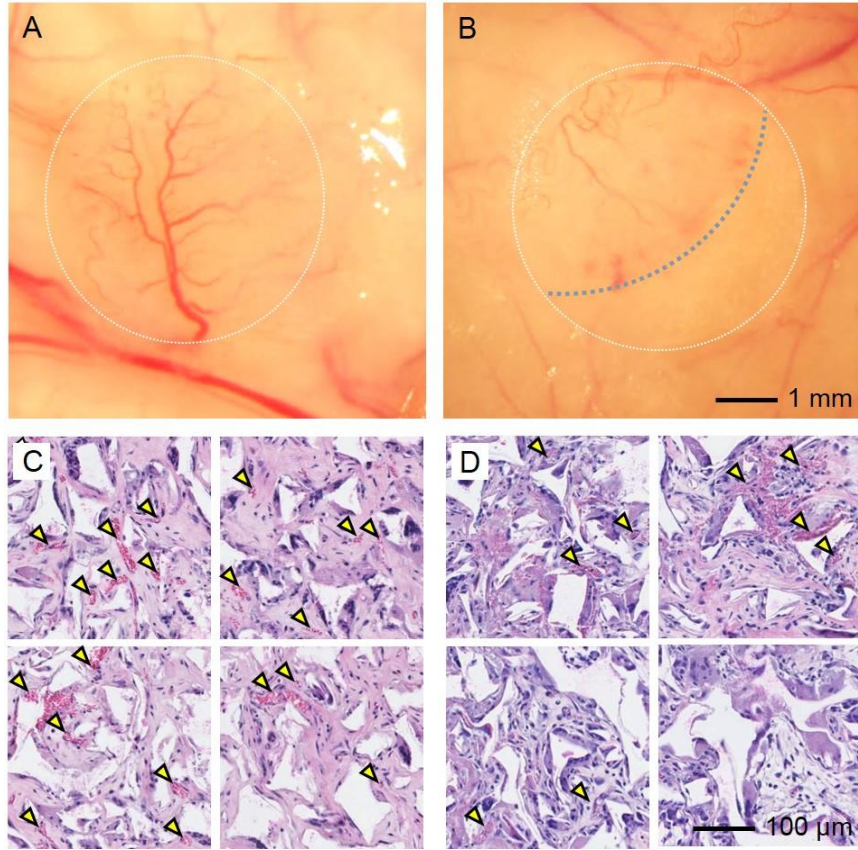


**Figure 2.6.** A, B) Photographs showing the gross appearance of blood vessels developed in a PLGA inverse opal scaffold and a PLGA non-uniform scaffold, respectively, at 4 weeks post subcutaneous implantation at the dorsal sides of nude mice. The white dotted circle in each image shows the boundary of the scaffold, and the blue dotted line delineates the boundary between the regions with extensive and poor neovascularization in a non-uniform scaffold. C, D) Bright-field transmission optical micrographs showing representative hematoxylin and eosin stained tissues from four corners of a section for a PLGA inverse opal scaffold and a PLGA non-uniform scaffold, respectively, at 4 weeks post implantation. Yellow arrowheads indicate blood vessels.

The difference in the distribution of neovasculature was further confirmed by microscopic examinations via histology analyses. Tissue sections at about 200 μm from

the top surface of the scaffolds were obtained and stained with hematoxylin and eosin. Each tissue/scaffold section was divided into four equal sectors and representative micrographs showing sections from an inverse opal scaffold and a non-uniform scaffold are presented in Figure 2.6, C and D, respectively. The inverse opal scaffold contained about the same amount of blood vessels with inter-vascular distances of approximately 100–200  $\mu\text{m}$  in each sector of the section, since all the pores in the entire scaffold had large interconnecting windows with a uniform size that allowed for efficient penetration of blood vessels. In comparison, it was found that for the non-uniform scaffold, while the top two sectors of the section contained a few blood vessels, the sector from the bottom-left corner only had two small vessels and there were essentially no blood vessels present in the sector from the bottom-right corner, indicating the limited interconnectivity for the pores within these two regions. The heterogeneous development of blood vessels in the non-uniform scaffolds may therefore result in volumes with poor neovascularization where inter-vascular distances far exceed the diffusion limits of 200  $\mu\text{m}$ , leading to impaired tissue viability and functions due to limited local availability of oxygen and nutrients [51, 52].

#### **2.4. Precise Control over Physical Properties of PLGA Inverse Opal Scaffolds**

One of the most significant features of the inverse opal scaffolds is that their pore sizes and related physical properties can be finely tuned. Nevertheless, there still lacks systematic studies in this sub-field despite the decade-long application of inverse opal scaffolds to tissue engineering and regenerative medicine. Therefore, in the current section I will present a systematic evaluation on how the pore/window/surface pore sizes of PLGA inverse opal scaffolds can be individually and precisely engineered by employing different combinations of fabrication conditions [53].

The most obvious and direct control is that over the pore size of the scaffolds. It is clear that the pore size of the resulting PLGA inverse opal scaffolds can be regulated simply by changing the diameter of the gelatin microspheres used as the templates. For example, Figure 2.7, A–D, shows SEM images of PLGA inverse opal scaffolds with pore sizes of 79, 147, 223, and 312  $\mu\text{m}$ , respectively, fabricated by templating against gelatin microspheres with corresponding sizes. Under constant fabrication conditions (annealing: 70  $^{\circ}\text{C}$  for 1 h; PLGA solution: 18 wt.%), all four types of scaffolds had roughly the same percentages of window size and surface pore size comparing to their respective pore sizes (Figure 2.7, A–D, insets).

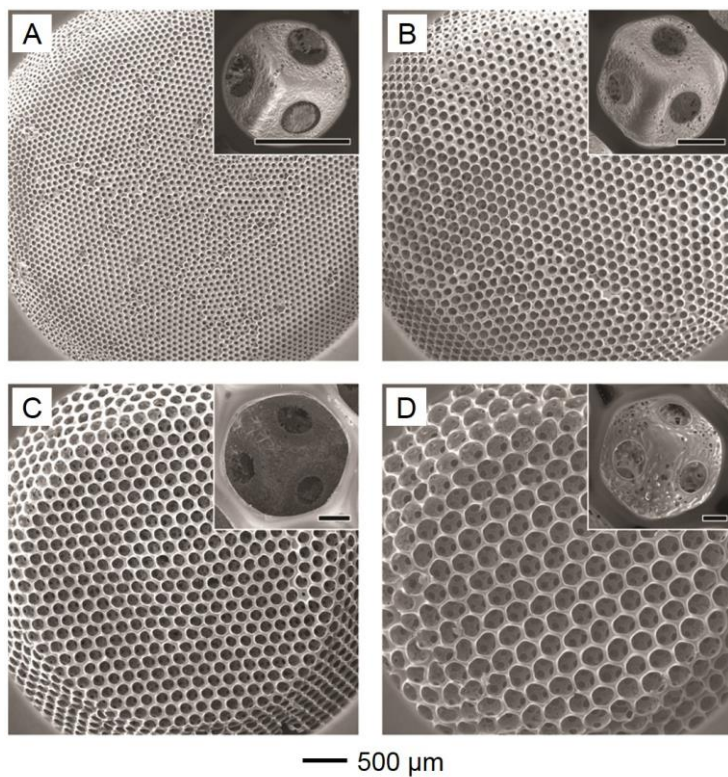


**Figure 2.7.** SEM images showing PLGA inverse opal scaffolds with uniform pore sizes of (A) 79, (B) 147, (C) 223, and (D) 312  $\mu\text{m}$ . The insets show magnified views of individual pores on the surface of the respective scaffolds; scale bar: 50  $\mu\text{m}$ . The annealing of gelatin microspheres was conducted at 75  $^{\circ}\text{C}$  for 1 h and an infiltration solution of 18 wt.% PLGA in 1,4-dioxane was used in all cases.

The other two controls are those over the window size and the surface pore size. I firstly investigated the capability to individually engineer the window size of a PLGA inverse opal scaffold. Uniform gelatin microspheres with a diameter of 190  $\mu\text{m}$  were used for this study. As shown in Figure 2.8, A–C, a significant increase in the window size was observed when the annealing temperature was elevated. At a constant annealing time of 3 h, the window size increased from approximately 25  $\mu\text{m}$  at 65  $^{\circ}\text{C}$  to approximately 43  $\mu\text{m}$  at 80  $^{\circ}\text{C}$  and approximately 66  $\mu\text{m}$  at 100  $^{\circ}\text{C}$ , corresponding to 13%, 23% and 35%, respectively, of the pore size (Figure 2.8D).

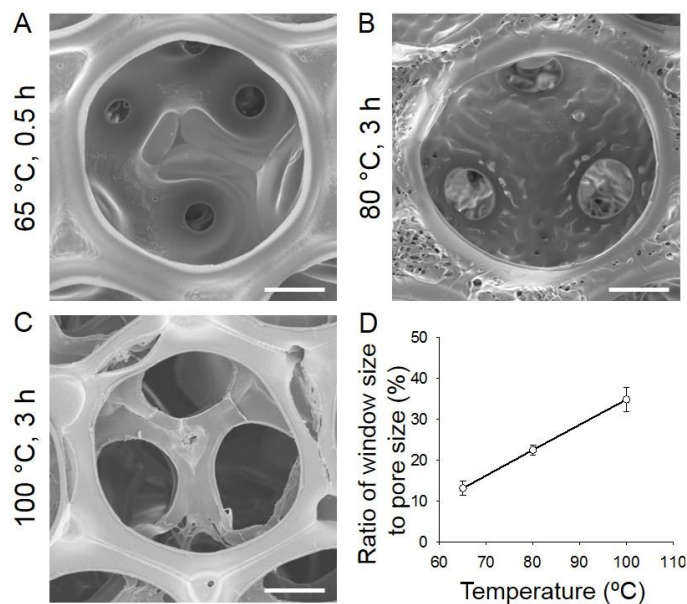


**Figure 2.8.** A–C) SEM images showing PLGA inverse opal scaffolds fabricated by annealing gelatin microspheres for 3 h at (A) 65  $^{\circ}\text{C}$ , (B) 80  $^{\circ}\text{C}$  and (C) 100  $^{\circ}\text{C}$ . Scale bars: 50  $\mu\text{m}$ . D) The ratio of window size to pore size as a function of annealing temperature. An infiltration solution of 18 wt.% PLGA in 1,4-dioxane was used in all cases.

The difference in window size can be attributed to a balance between the viscoelasticity and the intrinsic force originated from the surface tension (the Laplace

pressure) of the gelatin microspheres [54-57]. While dried gelatin has a glass transition temperature ( $T_g$ ) of 150–200 °C, this temperature is significantly reduced when the content of water in gelatin is increased [58]. In my case, the gelatin microspheres typically contained about 20–30 wt.% water, making the  $T_g$  of these microspheres to fall into the estimated range of 60–120 °C. At an annealing temperature of 65 °C, the microspheres would still be too hard for the surface tension to take effect in the annealing process when the phase transition of gelatin just started to occur. As the annealing temperature was elevated, the gelatin microspheres would become soft enough and the intrinsic forces of surface tension could result in prominent deformation for the microspheres and therefore the necking between adjacent ones, leading to the formation of much larger window sizes. It is worth noting that although the window size differed under different annealing conditions for the gelatin microspheres, the surface pore size largely remained constant at approximately 160  $\mu\text{m}$  (Figure 2.8, A–C), due to the same PLGA solution (18 wt.% in 1,4-dioxane) used to fabricate these scaffolds.

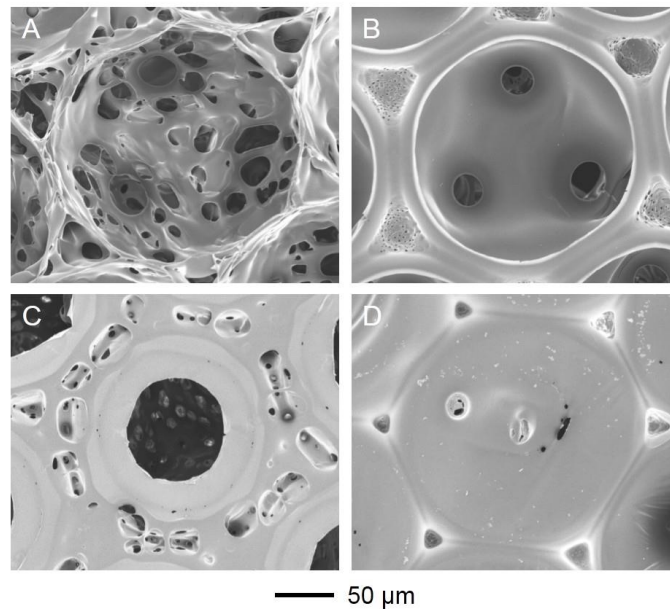


**Figure 2.9.** SEM images showing PLGA inverse opal scaffolds fabricated by infiltrating the lattices of gelatin microspheres with (A) 10 wt.%, (B) 18 wt.%, (C) 25 wt.%, and (D) 30 wt.%

*PLGA solutions in 1,4-dioxane. The annealing of gelatin microspheres was conducted at 65 °C for 3 h in all cases.*

I next investigated the capability to engineer the surface pore size of a PLGA inverse opal scaffold, using the same batch of uniform gelatin microspheres with a diameter of 190  $\mu\text{m}$ . In the fabrication procedure for inverse opal scaffolds, the excess PLGA solution on the surface of a templating gelatin lattice is removed by wiping against a filter paper. The polymer solution remaining in the meniscus among adjacent microspheres then solidifies to generate the surface pores. It is thus assumed that the surface pore size should be highly dependent on the concentration or the viscosity of the infiltrating PLGA solution in 1,4-dioxane. Indeed, as shown in Figure 2.9, the surface pore size decreased as the concentration of the PLGA solution increased, when annealing of the gelatin microspheres was conducted at 65 °C for 3 h in all cases. At a concentration of 10 wt.%, the surface pores essentially had the same size as the pore size in the bulk (Figure 2.9A), due to the inability of the excess solution to form the meniscus between adjacent microspheres at such a low viscosity. It was further noticed that, at the concentration of 10 wt.%, the wall of the scaffolds became highly porous due to the lack of sufficient polymer to fill the entire void volume after freeze-drying. At concentrations of 18 wt.% and 25 wt.%, the surface pore sizes were approximately 162  $\mu\text{m}$  and 73  $\mu\text{m}$ , respectively, corresponding to 85% and 38% of the pore size in the bulk (Figure 2.9, B and C). By contrast, at a concentration of 30 wt.% or higher, the surface of most pores became completely sealed by the polymer, resulting in disappearance of the surface pores (Figure 2.9D). In fact, it was rather difficult to infiltrate a 30 wt.% PLGA solution into a gelatin lattice in comparison to the 10 wt.% and 18 wt.% solutions, which could fill a lattice almost instantly.

It was then found that, the difference in the pore/window sizes could affect the mechanical strength of the inverse opal scaffolds. The mechanical properties of a 3D

porous scaffold are also of great importance in affecting its application because ideally, the mechanical properties of the scaffold should match those of the tissue to be engineered for optimal regeneration. As the pore size of an inverse opal scaffold increased from 108  $\mu\text{m}$  to 190  $\mu\text{m}$  and 330  $\mu\text{m}$  (window sizes: 14  $\mu\text{m}$ , 25  $\mu\text{m}$ , and 44  $\mu\text{m}$ , respectively; all 13% of the pore sizes), their compressive modulus decreased from 412 kPa to 361 kPa and 313 kPa, which might be attributed to the slight reduction in the scaffolding materials when the pore size was increased. With the same pore size of 190  $\mu\text{m}$ , the compressive modulus was lower (315 kPa *versus* 361 kPa) for scaffolds with larger window sizes (66  $\mu\text{m}$  *versus* 25  $\mu\text{m}$ ), presumably also due to the reduction in the scaffolding materials. It should be pointed out that, in the current system with PLGA, the change in the compressive modulus caused by the difference in the pore/window sizes of the scaffolds was relatively small and fell within the same order. Nevertheless, the results should still be of great value considering that such alterations in mechanical properties may be more pronounced when scaffolds with larger variance in pore/window sizes and/or scaffolds made from other materials (*e.g.*, hydrogels) are involved.

## **2.5. Functionalization of PLGA Inverse Opal Scaffolds**

In spite of their uniform structure and pore sizes, the as-prepared PLGA inverse opal scaffolds still cannot suffice the needs of all applications. For example, while the compressive moduli (a few hundred kPa) of pristine PLGA inverse opal scaffolds are on a scale similar to that of native cartilage, it is far lower than those of bony tissues and much higher than those of soft tissues. Hence, functionalization of the inverse opal scaffolds is sometimes more necessary than simply a decoration. In this section, I will introduce two distinctive methods for functionalization of PLGA inverse opal scaffolds: in the backbones with mineral nanoparticles; and in the pores with polymer

microstructures. In addition to the specific applications described in this section, these approaches can also be generalized and exploited in a variety of other similar utilizations.

### **2.5.1 Functionalization of PLGA Inverse Opal Scaffolds in the Backbones**

In an initial demonstration, I have developed an approach for fabrication of composite inverse opal scaffolds containing both PLGA and mineral for potential applications to bone tissue engineering [59]. The composite inverse opal scaffolds are well-suited for such applications because it has been shown that, scaffolds with a porosity greater than 70% and highly interconnected pores of over 100  $\mu\text{m}$  in diameters are preferred in order to support sufficient penetration of cells and blood vessels for optimal regeneration of trabecular bones (porosity: 50–90%) [60]. On the other hand, native bones are composed of a mixture of approximately 60–70% inorganic and 30–40% organic materials by dry weight [61]. While the organic component mainly contains type I collagen, the inorganic component is generally recognized as bioapatite [62], a biologically produced mineral analog of natural hydroxyapatite (HAp). Therefore, impregnating hydroxyapatite/apatite components into the backbones of polymeric scaffolds have been demonstrated to improve the osteo-conductivity and/or the osteo-inductivity of the scaffolds by mimicking the native bone in its structure and composition [60, 63-65]. Stem cells and osteoprogenitor cells could then efficiently adhere, proliferate, and differentiate on these composite scaffolds [66-70]. Moreover, the apatite layer exposed on the surface of the scaffolds would also promote their integration with native bones upon implantation [60, 64].

To fabricate composite inverse opal scaffolds, 1,4-dioxane containing PLGA and spherical hydroxyapatite nanoparticles (200 nm in size; 50 wt.% to PLGA) was used as the infiltration agent. All other procedures were kept the same for fabricating regular PLGA inverse opal scaffolds. The resulting composite scaffolds are termed the

PLGA/HAp inverse opal scaffolds. Another type of composite scaffolds were fabricated by further depositing bone-like apatite onto the surface of the PLGA/HAp scaffolds using simulated body fluid (SBF) [71-74], and are referred to as apatite-coated PLGA/HAp inverse opal scaffolds.

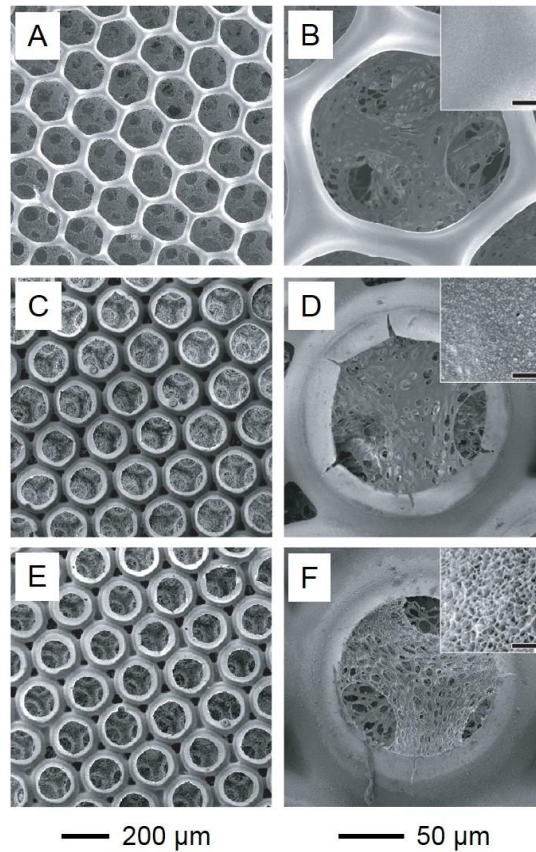


**Figure 2.10.** SEM images showing (A, B) plain PLGA inverse opal scaffolds, (C, D) PLGA/HAp composite inverse opal scaffolds, and (E, F) apatite-coated PLGA/HAp composite inverse opal scaffolds. The insets in (B, D, and F) show magnified images of the surfaces of the three types of scaffolds, respectively; scale bars: 2.5 μm.

Figure 2.10 shows representative SEM images of the PLGA, PLGA/HAp, and apatite-coated PLGA/HAp inverse opal scaffolds. All the scaffolds contained uniform and spherical pores of 213 μm in diameter (Figure 2.10, A, C and E). The PLGA/HAp

scaffold had dense, small HAp nanoparticles on the surface (Figure 2.10D, inset) and the apatite-coated PLGA/HAp scaffold displayed a large amount of apatite crystals deposited on the surface (and thus increased surface roughness, Figure 2.10F, inset), whereas the PLGA scaffold only showed a very smooth surface (Figure 2.10B, inset). More importantly, the addition of mineral could significantly increase the mechanical properties of the PLGA-based inverse opal scaffolds. As indicated in Figure 2.11, in comparison to the relatively low compressive modulus on the order of several hundred kPa for the PLGA scaffolds, the PLGA/HAp scaffolds had a much higher modulus of  $1,744.7 \pm 68.6$  kPa and the modulus was further increased to  $1,952.8 \pm 54.1$  kPa by apatite coating (*i.e.*, for apatite-coated PLGA/HAp scaffolds), both of which had approached that of small cancellous bones.

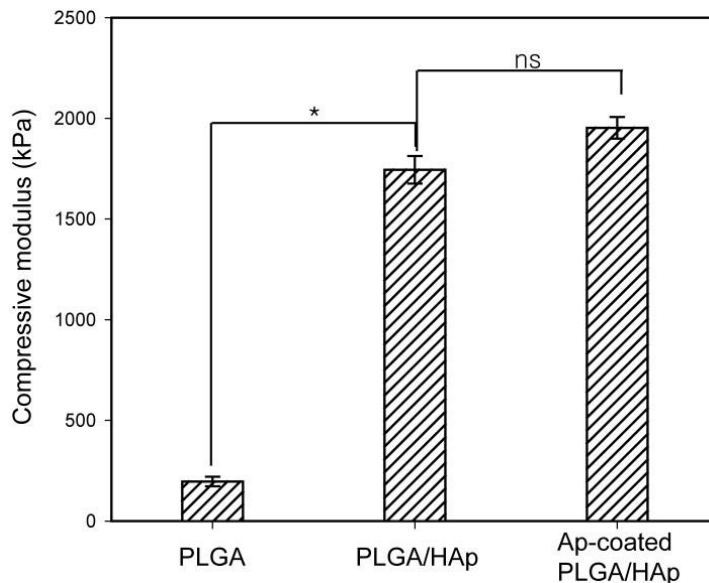


**Figure 2.11.** Compressive moduli of PLGA, PLGA/HAp, and apatite (Ap)-coated PLGA/HAp inverse opal scaffolds ( $n = 3$  in all cases). \*Statistical significance; ns: no statistical significance.

The effect of mineral functionalization was subsequently investigated by culturing MC3T3-E1 preosteoblasts in the scaffolds in an osteogenic differentiation medium. As

shown in Figure 2.12, the cells proliferated fast initially in the PLGA scaffolds, but the proliferation rate was slowed down over time. In contrast, the cells in the apatite-coated PLGA/HAp scaffolds showed a nearly constant proliferation rate throughout the 4-week period. This may indicate that cells in the apatite-coated PLGA/HAp scaffolds were more devoted to differentiating than proliferating. The cells in the PLGA/HAp scaffolds showed a proliferation behavior similar to that of the cells in the apatite-coated PLGA/HAp scaffolds. These results are consistent with a study performed by Shu *et al.*, who showed enhanced differentiation but decreased cell growth for osteoblasts seeded on HAp discs placed in a differentiation medium [75].

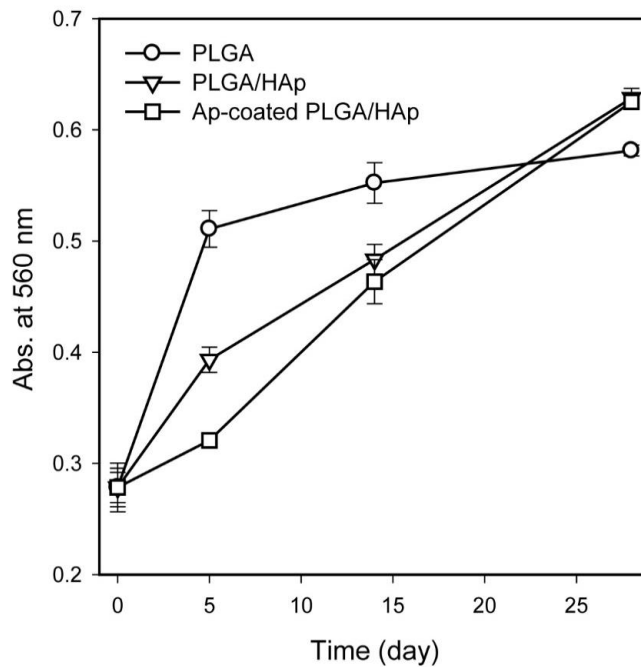


**Figure 2.12.** Proliferation of the MC3T3-E1 preosteoblasts cultured in PLGA, PLGA/HAp, and apatite-coated PLGA/HAp inverse opal scaffolds.

Figure 2.13 shows representative SEM images of the cells in different scaffolds at 4 weeks of culture. Most of the pores around the perimeter of the PLGA scaffold were occluded by the cells and secreted ECM (Figure 2.13A), presumably restricting the

diffusion of macromolecules in the culture medium into the center of the scaffolds [76]. On the contrary, a large number of nodule-like mineral (indicated by arrows) were observed in the pores of the apatite-coated PLGA/HAp scaffold (Figure 2.13C). The mineralization of the cells in the PLGA/HAp scaffolds showed an intermediate profile in between the other two types of scaffolds (Figure 2.13B). These observations are likely related with the rough and stiff surfaces of the PLGA/apatite composite scaffolds, which provided a favorable environment for the proliferation and differentiation of osteogenic cells [77-80].

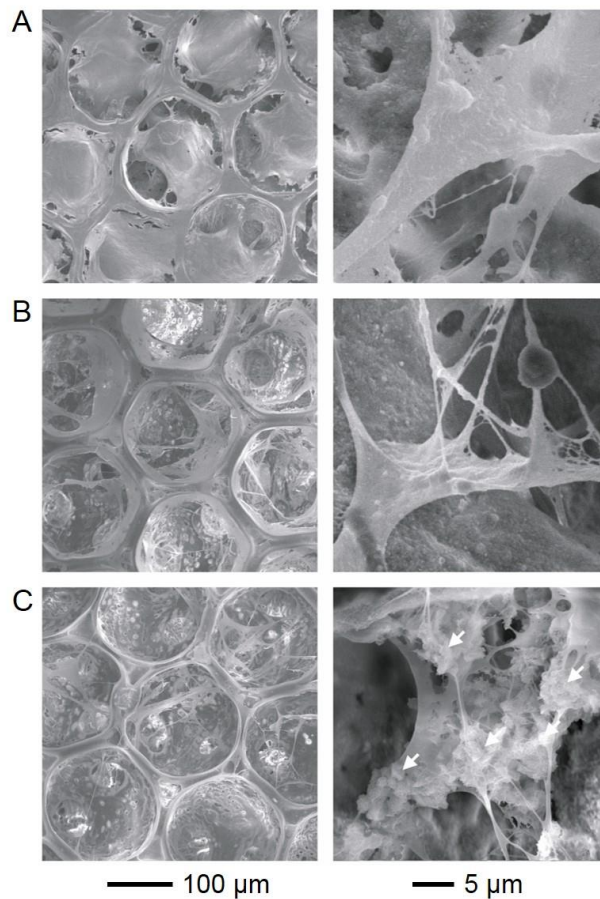


**Figure 2.13.** SEM images of the cells cultured in (A) PLGA, (B) PLGA/HAp, and (C) apatite-coated PLGA/HAp scaffolds for 28 days. The arrows in the images indicate the mineral produced by the cells.

Importantly, such an approach to functionalize PLGA inverse opal scaffolds in the backbones could be conveniently adapted and extended to other applications. For example, similar to mineral, bioactive molecules including growth factors could be encapsulated into the backbone of a scaffold by directly dissolving the molecules in the infiltration solution. In order to modulate the release kinetics of bioactive molecules, growth factors may be firstly loaded within polymer nanoparticles followed by secondary encapsulation in the backbone of a scaffold [81, 82]. Alternatively, it is also feasible to immobilize growth factors onto the surface of a PLGA inverse opal scaffold by taking advantage of the heparin-binding capability of certain growth factors (*e.g.*, basic fibroblast growth factor, vascular endothelial growth factor). Specifically, heparin is firstly covalently conjugated onto the surface of a PLGA inverse opal scaffold via carbodiimide reaction. Then the scaffold with surface-bound heparin is incubated in a solution containing the target growth factor(s) to allow the molecules to bind to heparin for controlled release [83, 84].

### **2.5.2 Functionalization of PLGA Inverse Opal Scaffolds in the Pores**

Besides the functionalization of PLGA inverse opal scaffolds in the backbones, the pores of the scaffolds can also be modified. As a matter of fact, such modification is sometimes more necessary than just an ornament. When the pore size (*e.g.*, >100–200  $\mu\text{m}$ ) of an inverse opal scaffold is much larger than the lateral dimension (typically, 20–150  $\mu\text{m}$ ) of a stretching cell (Figure 2.14), the cell would actually experience a local microenvironment similar to a two-dimensional (2D) substrate, and tends to attach and stretch along the wall of the pore. As such, the cell(s) would not be able to efficiently utilize the entire void space associated with the pore.

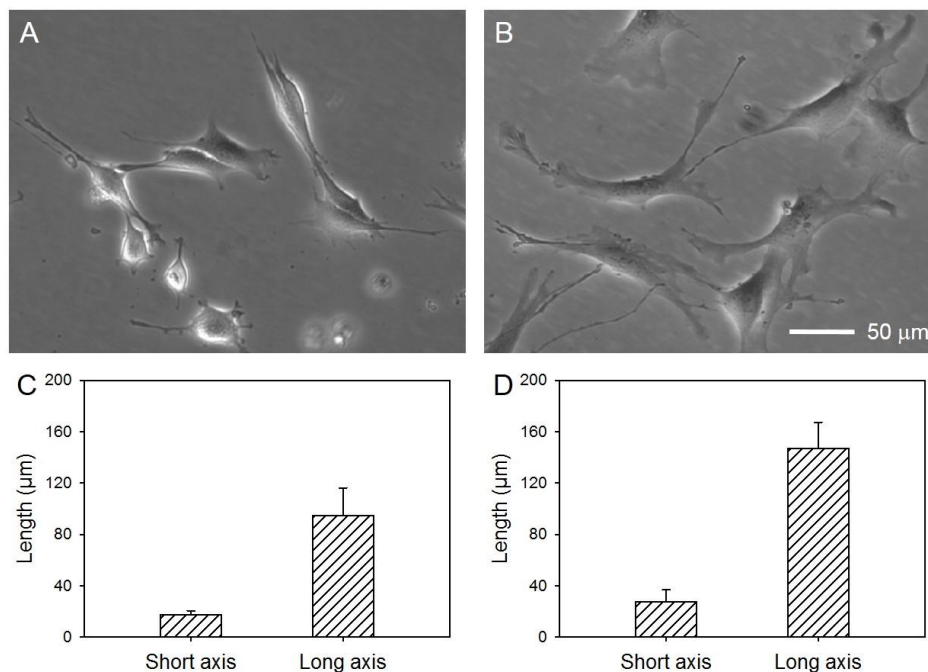


**Figure 2.14.** A, B) Phase contrast images showing NIH/3T3 fibroblasts and MC3T3 preosteoblasts cultured on the bottom of Petri dishes. C, D) Quantitative analysis showing the lengths of the short and long axes for the two different types of cells.

I have addressed this issue by functionalizing the pores of an inverse opal scaffold with another polymer solution using a simple dual-step process: infiltration and freeze-drying. In doing so, a truly 3D microenvironment was created inside the void space of a pore to promote cellular attachment and proliferation [85]. Specifically, chitosan was chosen as a material for the infiltration process because of its unique fibrous structure that develops during a freeze-drying process, as well as its biocompatible and biodegradable features [86]. Moreover, chitosan does not require the application of a cross-linker to retain its solid structure since it is only soluble in an acidic solution, not in a typical cell culture medium or a body fluid with neutral pH.

Figure 2.15A shows a transmission bright-field micrograph of an as-prepared PLGA inverse opal scaffold with a uniform pore size of 200 μm and Figure 2.15B shows a transmission bright-field micrograph of a PLGA scaffold after it had been

functionalized with chitosan (PLGA-CS). It is clear that all the pores were filled with chitosan microstructures. The SEM images in Figure 2.15, C and D, show enlarged views of individual pores in the PLGA and the PLGA-CS scaffolds, respectively. After freeze-drying, chitosan evolved into fibrous microstructures that randomly filled the entire void space of a pore. These fibrous structures efficiently reduced the distance between the opposite surfaces of a pore from hundreds of micrometers to a few tens of micrometers to match the lateral dimensions of a stretching cell. To validate the structure in the central region of the scaffolds, the scaffolds were vertically cut from the middle portion. As expected, the PLGA scaffold had uniform pore structures and windows (Figure 2.15E) while all the pores inside the PLGA-CS scaffold were completely filled with chitosan microstructures (Figure 2.15F).

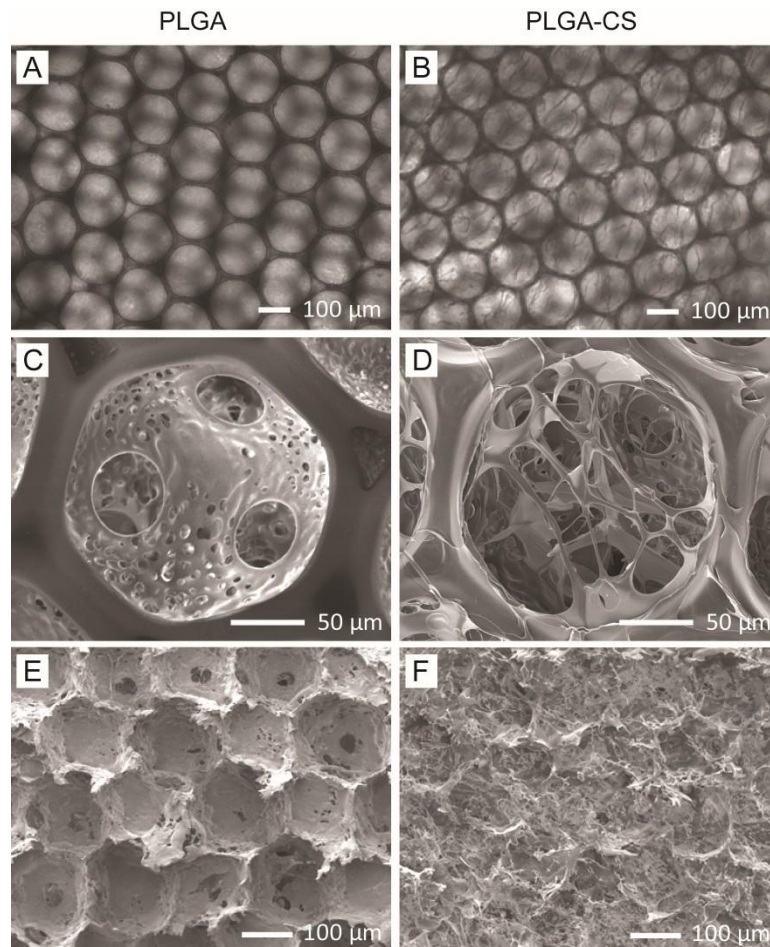


**Figure 2.15.** A, B) Transmission optical micrographs showing a plain PLGA inverse opal scaffold and a PLGA inverse opal scaffold functionalized with chitosan microstructures in the pores, respectively. C, D) SEM images showing individual pores of a plain PLGA inverse opal scaffold and a PLGA inverse opal scaffold functionalized with chitosan microstructures in the pores, respectively. E, F) SEM images showing cross-sectional views of a plain PLGA inverse opal scaffold and a PLGA inverse opal scaffold functionalized with chitosan microstructures in the pores, respectively.

I then compared the proliferation profiles of cells in these two types of scaffolds using MC3T3-E1 preosteoblasts as a model cell line. The scaffolds were seeded with the cells at a density of  $2 \times 10^5$  cells per scaffold using a spinner flask to ensure good homogeneity in cell seeding. After 3 h, the scaffolds were removed from the spinner flask and placed in the wells of a 12-well plate. Seeding efficiency was calculated by counting the remaining cells that did not attach to the scaffolds, and then normalized against the number of cells initially added for seeding. It was found that, the pristine PLGA scaffolds had a high seeding efficiency (approximately 45%), which could be attributed to the large pore size and high interconnectivity of the inverse opal scaffolds (Figure 2.16A). In comparison, the PLGA-CS scaffolds had a lower seeding efficiency of approximately 25%. This result is reasonable because during the same period of time (3 h) for cell seeding, it would be more difficult for the cells to diffuse into the inner space of the PLGA-CS scaffolds than the PLGA scaffolds as the PLGA scaffolds did not have the microstructures to hinder the movement of the cells during the seeding process. Cell proliferations were assessed at days 1, 3, 7, and 14 post-seeding using the MTT assay (Figure 2.16B). For the PLGA scaffolds, the cells proliferated faster at the early stage (1–3 days), and the proliferation slowed down afterwards. For the PLGA-CS scaffolds, the cells proliferated linearly at the first 7 days, by which the cell number reached the same level as that for the PLGA scaffolds. The proliferation of cells slowed down only slightly

afterwards, and by day 14, the cell number had exceeded that in the PLGA scaffolds by approximately 25% on average. When the cell number at each time point was normalized to that at day 1 for each type of scaffolds, a significant difference between the two types of scaffolds was observed (Figure 2.16C). The normalized number of cells in the PLGA-CS scaffolds showed an increase of approximately 6.5 folds in number over the 14-day period, whereas there was only a 3-fold increase for the PLGA scaffolds.

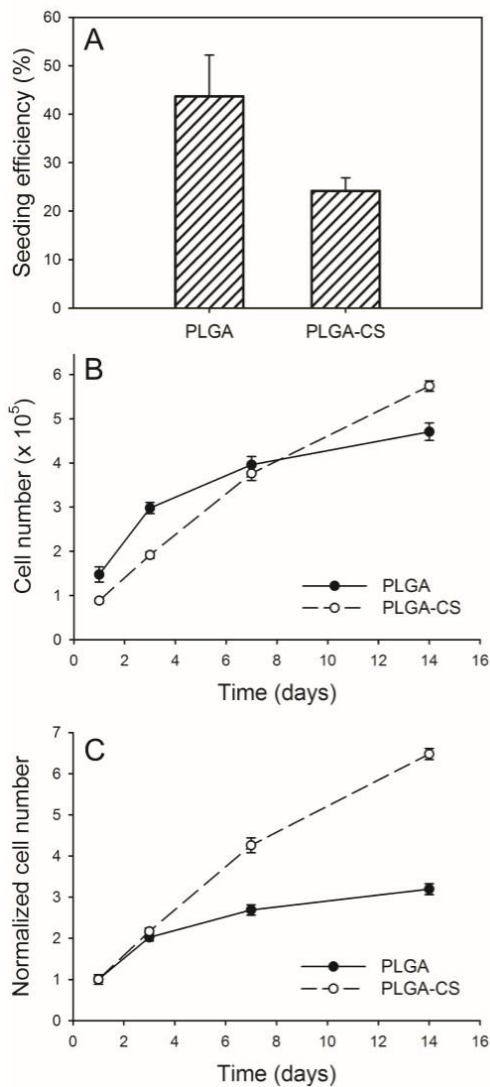


**Figure 2.16.** A) Seeding efficiency of MC3T3 preosteoblasts for a plain PLGA inverse opal scaffold and a PLGA inverse opal scaffold functionalized with chitosan microstructures in the

pores. B) Proliferation of MC3T3 preosteoblasts in a plain PLGA inverse opal scaffold and a PLGA inverse opal scaffold functionalized with chitosan microstructures in the pores. C) Normalized proliferation of MC3T3 preosteoblasts in a plain PLGA inverse opal scaffold and a PLGA inverse opal scaffold functionalized with chitosan microstructures in the pores.

To locate the positions of the cells in the pores of the two different types of scaffolds, the cells were fixed with formaldehyde post-seeding at 1 and 14 days, and then characterized with a confocal microscope. Figure 2.17 shows confocal micrographs obtained at approximately 50  $\mu\text{m}$  below the surface of the scaffolds with a layer thickness of 5  $\mu\text{m}$ . Chitosan is shown in green (pre-labeled with FITC) and cell nuclei in red (stained with propidium iodide, PI).

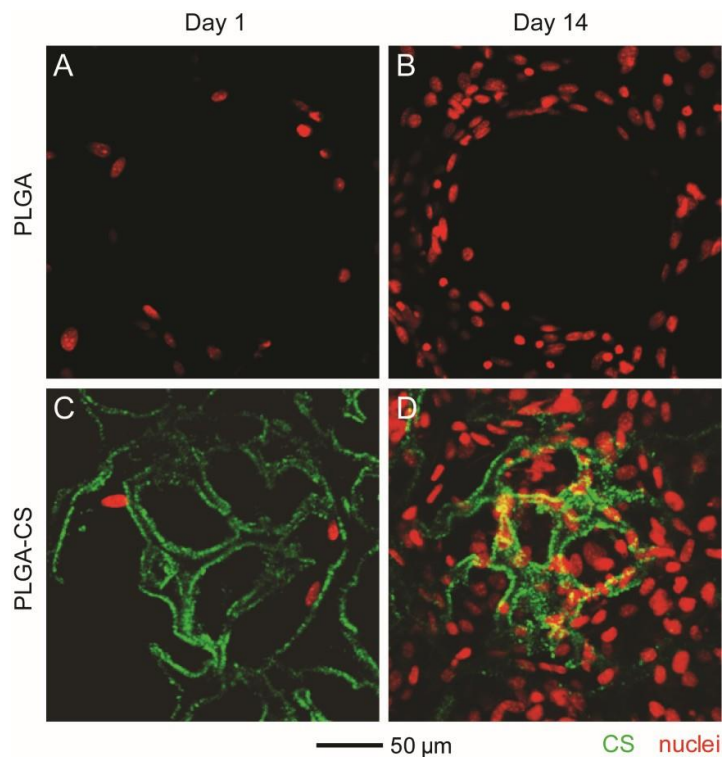


**Figure 2.17.** CLSM images showing the distribution of MC3T3 preosteoblasts in (A, B) plain PLGA inverse opal scaffolds and (C, D) PLGA inverse opal scaffolds functionalized with chitosan microstructures in the pores at (A, C) day 1 and (B, D) day 14 post seeding. The nuclei

*of the cells were stained in red and the chitosan (CS) microstructures were labeled with FITC (green).*

In the PLGA scaffold, the cells could only attach, proliferate and migrate along the wall of the pore, and they were unable to occupy the void space of the pore during given period of culture (Figure 2.17, A and B). This observation could be attributed to the contact inhibition of most normal, non-cancerous cells, which would slow down the proliferation when the cells are confluent on a surface. For the PLGA-CS scaffold, however, the cells showed a different initial distribution even at day 1 post seeding, where some of the cells had already started to attach to the chitosan microstructures in the void space (Figure 2.17C). The cells proliferated quickly, and by day 14, the cells took most of the void space in the pore (Figure 2.17D), rather than just attaching to the proximity of the wall of the pore.

This result is significant because it allows full occupation of the void space in a scaffold by cells in a relatively short period of time and can thus potentially improve the overall quality of the engineered tissue by reducing the density of defects. When such scaffolds are implanted *in vivo*, they should also be able to induce faster tissue infiltration to generate better scaffold-tissue interfaces.

## **2.6. Summary**

PLGA inverse opal scaffolds were fabricated by templating against gelatin microspheres with uniform diameters. The inverse opal scaffolds possessed a long-range well-ordered structure with uniform pores and interconnecting windows. The advantages of the inverse opal scaffolds were demonstrated, in terms of higher reproducibility among different batches of fabrication, faster diffusion of macromolecules, more homogeneous

distribution of cells *in vitro*, and more uniform neovascularization *in vivo*, all in comparison with their counterparts with spherical but non-uniform pores.

I have then demonstrated the precise control over the physical properties of PLGA inverse opal scaffolds. The pore size, window size, and surface pore size of a PLGA inverse opal scaffold could be finely tuned, respectively, by controlling the diameter of the templating gelatin microspheres, the annealing temperature of the gelatin lattice, and the concentration/viscosity of the PLGA solution for infiltration. It was further demonstrated that the PLGA inverse opal scaffolds could be functionalized both in the backbone by incorporating mineral nanoparticles, as well as in the pores by filling with chitosan microstructures, therefore expanding their potential applications in tissue engineering and regenerative medicine.

## **2.7. Experimental**

### **2.7.1. Materials and Chemicals**

Gelatin (type A, from porcine skin), sorbitan monooleate (Span<sup>®</sup> 80), and toluene were all obtained from Sigma-Aldrich (St. Louis, MO) and used for fabricating the gelatin microspheres with uniform sizes. PLGA (lactide:glycolide = 75:25,  $M_w = 66,000$ – $107,000$ ) and 1,4-dioxane were also obtained from Sigma-Aldrich and used for fabricating the scaffolds. FITC-dextran ( $M_w \approx 20,000$ , Sigma-Aldrich), a hydrophilic dye, was used to evaluate the diffusion of macromolecules through the scaffolds. All of the chemicals for the preparation of 10-times concentrated SBF (10xSBF) were purchased from Sigma-Aldrich. All chemicals were used as received. The water used in all fabrications was obtained by filtrating through a set of cartridges (Millipore, Billerica, MA). The poly(vinyl chloride) (PVC) tubes and glass microcapillary tubes were purchased from VWR International (Radnor, PA). Syringe needles were obtained from BD Biosciences (San Jose, CA).

### **2.7.2. Preparation of Gelatin Microspheres Using a Fluidic Device**

Monodispersed gelatin microspheres were prepared using a custom-made fluidic device [47]. The microfluidic device consisted of a PVC tube (1/32 in. i.d. × 3/32 in. o.d.), a glass microcapillary tube, and a syringe needle (Figure 2.1A). The device was fabricated by inserting the needle and glass microcapillary tube into the PVC tube, followed by fixing with an epoxy adhesive. The discontinuous phase was an aqueous solution of gelatin and the continuous phase was toluene containing approximately 3 vol.% Span<sup>®</sup> 80. The two phases were introduced by syringe pumps (KDS200, KD Scientific, Holliston, MA) at independently adjusted flow rates. The droplets formed at the tip of the needle flowed along the glass microcapillary tube into a 1-L tall beaker containing approximately 900 mL of the collection phase (the same as the continuous phase) incubated in an ice bath. The gelatin droplets were gently stirred for 12–36 h (dependent on the size of the droplets) to allow water to evaporate completely. The dried gelatin microspheres were collected by filtrating against a filter paper, and then washed with and stored in methanol until further use.

### **2.7.3. Preparation of PLGA Inverse Opal Scaffolds and Non-Uniform Scaffolds**

Scaffolds were fabricated using a templating process [49, 59, 85]. A suspension of gelatin microspheres in methanol was placed in a 50-mL centrifuge tube and the tube was then gently tapped to obtain a ccp lattice of the microspheres. The resultant ccp lattice was placed in an oven heated at a pre-set temperature (65–100 °C) for different periods of time (1–3 h) to induce the necking between adjacent gelatin microspheres. After cooling down to room temperature, the lattice was carefully harvested using a spatula. The lattice was placed on a filter paper to allow methanol to evaporate completely, and then infiltrated with a PLGA solution in 1,4-dioxane (10–30 wt.%). After removing the excess solution with a filter paper, the lattice pellet containing PLGA solution was frozen in a refrigerator (-20 °C) for 5 h, and lyophilized in a freeze-dryer (Labconco, Kansas City,

MO) overnight. The sample was then placed in a beaker containing 900 mL of water heated at 43 °C for 3–4 h under gentle stirring to dissolve the gelatin microspheres.

To fabricate PLGA/HAp composite inverse opal scaffolds, the PLGA solution in 1,4-dioxane containing HAp nanopowder (18 wt.% for PLGA and 9 wt.% for HAp) was sonicated for 30 min, vortexed for 1 min, and then infiltrated into the voids of the gelatin lattice. Apatite-coated PLGA/HAp scaffolds were fabricated by further depositing a layer of apatite on the surface of the PLGA/HAp scaffolds. Specifically, about 10 scaffolds were soaked in 100 mL of the 10xSBF for 2 h under gentle stirring on an orbital shaker and then rinsed with water [73, 74].

To functionalize the pores of a PLGA inverse opal scaffold with chitosan microstructures, 1 wt.% chitosan solution in 500 mM acetic acid (HAc) aqueous solution was infiltrated into the as-prepared PLGA scaffold. After removing the excess chitosan solution with a filter paper, the PLGA scaffold containing chitosan solution was subjected to freeze-drying immediately for 24 h.

Non-uniform scaffolds were fabricated by templating against “lattices” prepared from polydispersed gelatin microspheres. The non-uniform gelatin microspheres were produced by gradually changing the flow rate of the continuous phase (toluene plus Span<sup>®</sup> 80) during the production of gelatin emulsions in the fluidic device while other parameters were maintained the same as those for the fabrication of monodispersed gelatin microspheres. The non-uniform gelatin microspheres in methanol were placed in an oven heated at 70 °C for at least 2 h to make the template robust enough for handling. All other conditions and procedures remained the same as those used for the inverse opal scaffolds.

#### **2.7.4. Measurement of Diffusion Rates through the Scaffolds**

A flow device was constructed using two 50-mL centrifuge tubes, a PVC tube, and a connector (Figure 2.4A) [49]. After filling each centrifuge tube with 40 mL of

water, more water was introduced into the centrifuge tube on the right side using a syringe pump (KD200, KD Scientific) at a flow rate of  $1.0 \text{ mL min}^{-1}$  to induce a pressure difference between the two centrifuge tubes. When the flow rate in the sampling tap (centrifuge tube on the left side) was stabilized, 0.5 mL of FITC-dextran aqueous solution (0.5 wt.%) was quickly dropped into the right centrifuge tube and the eluent in the sampling tap was collected every minute and analyzed using a spectrophotometer (Infinite200, Infinite 200, TECAN, Durham, NC).

### **2.7.5. Cell Culture in the Inverse Opal Scaffolds and Characterization**

Prior to cell seeding, the scaffolds were wetted and sterilized by immersion in 70 vol.% ethanol in water for 2 h, washed with phosphate buffered saline (PBS, Invitrogen, Carlsbad, CA) three times and stored in PBS until use.

Mouse embryonic fibroblasts (NIH/3T3; American Type Culture Collection, ATCC, Manassas, VA) were used for cell distribution experiments. The cells were maintained in a Dulbecco's Modified Eagle's Medium (DMEM, ATCC), supplemented with 10 vol.% fetal bovine serum (FBS, Invitrogen) and 1 vol.% penicillin/streptomycin (P/S, Invitrogen). Approximately  $1.6 \times 10^5$  cells were used for seeding into each scaffold using a spinner flask (125 mL capacity, Proculture<sup>TM</sup>, Corning, Tewksbury, MA) at 65 rpm for 2–4 h in an incubator. The cell-seeded scaffolds were then transferred to 12-well plates (not treated for tissue culture, BD Biosciences; 1 scaffold per well). The cultures were maintained in an incubator at 37 °C in a humidified atmosphere containing 5% CO<sub>2</sub>, and the media were changed every other day. At 7 days of culture, culture media were withdrawn, scaffolds were washed with PBS, and the cells were fixed with 4 vol.% formaldehyde in PBS for 10 min. Cell nuclei were then stained with 4',6-diamidino-2-phenylindole (DAPI, Invitrogen). The cell/scaffold constructs were subsequently embedded in an optimal cutting temperature (O.C.T.) compound (Tissue-Tek<sup>®</sup>, Ted Pella, Redding, CA) and horizontally sectioned using a microtome (Cryostat, Microm HN550E,

Thermo Scientific, Waltham, MA) until middle planes (around 500  $\mu\text{m}$  in depth from the surface into the constructs) was exposed. The sectioned constructs were observed using an Olympus microscope equipped with Capture 2.90.1 (Olympus, Center Valley, PA).

Mouse calvaria-derived, preosteoblastic cells (MC3T3-E1; ATCC) were used for cell differentiation experiments with PLGA/apatite composite inverse opal scaffolds. The cells were maintained in an alpha Minimum Essential Medium ( $\alpha$ -MEM, Invitrogen), supplemented with 10 vol.% FBS and 1 vol.% P/S. Approximately  $1.5 \times 10^5$  cells were used for seeding into each scaffold using a spinner flask. The cell-seeded scaffolds were then transferred to 12-well plates (not treated for tissue culture; 1 scaffold per well), and cultured in an osteogenic differentiation medium supplemented with 300  $\mu\text{M}$  L-ascorbic acid, 10 mM  $\beta$ -glycerol phosphate, and 10 nM dexamethasone (Sigma-Aldrich). The cultures were maintained in an incubator at 37  $^{\circ}\text{C}$  in a humidified atmosphere containing 5%  $\text{CO}_2$  for up to 4 weeks and the medium was changed every other day.

MC3T3 preosteoblasts were also used for studies related with inverse opal scaffolds functionalized with chitosan microstructures. A total of approximately  $2 \times 10^5$  cells were used to seed into each scaffold using a spinner flask. The scaffolds were then transferred to 12-well plates (not treated for tissue culture; 1 scaffold per well), and maintained in a proliferation medium for up to 2 weeks. At days 1 and 14 post seeding, the samples were fixed in 4 vol.% formaldehyde in PBS and the nuclei of the cells were stained using propidium iodide (PI, Invitrogen). Fluorescence was detected using a confocal laser scanning microscope (CLSM, LSM 510, Carl Zeiss, New York, NY).

#### **2.7.6. Cell Proliferation Assay**

Cell proliferation was measured at desired intervals post cell seeding using the 3-(4,5-dimethylthiazol-2-yl)-2,5-diphenyltetrazolium bromide (MTT) assays. MTT is a water-soluble tetrazole that can be metabolized and reduced to purple, water-insoluble formazan in live cells. Typical assays were carried out in 12-well plates: 40  $\mu\text{L}$  of MTT

(Invitrogen) solution in PBS (5 mg/mL) was added to each well and incubated at 37 °C for 2–4 h and the culture media were withdrawn. Then 1 mL of isopropanol (Sigma-Aldrich) was then added to each well to completely dissolve the formazan crystals throughout the scaffold. Absorbance was measured at 560 nm using a spectrophotometer (Infinite 200, TECAN).

### **2.7.7. Mechanical Test**

To determine the mechanical properties of the scaffolds, cylindrical specimens ( $n = 3$  per group) were prepared using a mold made of poly(dimethyl siloxane) (PDMS, Dow Corning, Midland, MI). The scaffolds were sandwiched between two glass slides with unconfined compression using a custom-built testing frame [59]. Compression was applied at a crosshead speed of 0.01 mm/s (approximately 0.6% per second in strain rate) at ambient temperature and humidity. Load and displacement data were collected using a computerized data acquisition system (Labview, National Instruments, Austin, TX). Engineering stress was calculated as the load divided by the cross-sectional area of a sample. Strain was calculated as change in displacement divided by the original thickness of a sample. Modulus was calculated by linear regression using data from the linear portion of the stress-strain plot. The Bose Endura TEC ELF 3200 uniaxial testing system (DetapointLabs, Ithaca, NY) was also used to measure the mechanical properties of the scaffolds in some cases.

### **2.7.8. Scanning Electron Microscopy**

SEM (Nova NanoSEM 2300, FEI, Hillsboro, OR; Ultra 60, Carl Zeiss, Thornwood, NY) was used to characterize the scaffolds and/or the scaffold/cell constructs. In the cases where cells were involved, the specimens were fixed first in 4 vol.% formaldehyde in PBS, rinsed three times with water, dehydrated in a graded ethanol series (70–100 vol.% in water), and air dried. The samples were sputter-coated

with gold or gold/palladium for 1–3 min prior to imaging. Images were taken at an accelerating voltage of 5–10 kV.

### **2.7.9. Statistics**

Experimental results were expressed as means  $\pm$  standard deviation of the samples. Statistical comparisons were evaluated by analysis of variance (ANOVA) followed by post-hoc analysis, and statistical significance was accepted at  $p < 0.05$ .

## CHAPTER 3

### INVERSE OPAL SCAFFOLDS AS A WELL-DEFINED SYSTEM

#### 3.1. Introduction

In Chapter 2, I discussed in detail the advantages of inverse opal scaffolds as compared to their counterparts with spherical but non-uniform pores. Due to their uniform and high interconnectivity, the inverse opal scaffolds can ensure homogeneous cell seeding, facilitate free migration of cells, and enhance diffusion of biomacromolecules including nutrients and wastes. The unique inverse opal structure originated from the cubic close packing of the templating microspheres with monodispersed sizes further makes the scaffolds highly reproducible over different batches of fabrication, therefore minimizing their variations in structure during production. Another advantage of the inverse opal scaffolds is that, their pore size, surface pore size, and window size can be individually and precisely engineered over a broad range. Therefore, inverse opal scaffolds are well-suited for studying the effect of size-dependent parameters of porous scaffolds on the behavior of cells and/or tissues.

In Section 3.2, I will present a proof-of-concept experiment, in which the osteogenic differentiation of MC3T3 preosteoblasts is compared for apatite-coated PLGA/HAp composite inverse opal scaffolds with two different pore sizes of 211  $\mu\text{m}$  and 313  $\mu\text{m}$ . The precision in pore size of an inverse opal scaffold can greatly reduce the experimental errors and thus make the results more reliable. Previously, a few studies have attempted to investigate the similar pore size effect on the differentiation of stem/progenitor cells. For example, mineral-containing scaffolds with pore sizes around 200  $\mu\text{m}$  are generally known as optimal conditions for osteogenic induction [79, 80, 87, 88]. Unfortunately, the scaffolds used in those studies are typically characterized by a

broad distribution in pore sizes. As a result, the use of these non-uniform scaffolds can sometimes lead to inaccurate and unconvincing data because the results are dependent on the collective behaviors of the cells in many pores that are smaller than, equal to, or larger than the average pore size. As a matter of fact, it is more likely that the responses of the cells are affected by the properties of individual pores of a scaffold, as the dimensions of the cells are typically smaller than that of the pore in which the cells reside.

Another important paradigm in tissue engineering and regenerative medicine is the establishment of a robust vasculature in order to facilitate the transport of oxygen, nutrients and wastes to/from the cells residing in the bulk of a 3D scaffold well beyond the limit of passive diffusion [51, 89]. Despite impressive progress in recent years, it remains a grand challenge to apply the concept of tissue engineering and regenerative medicine to thick and complex tissues or organs due to the lack of rapid neovascularization (*i.e.*, formation of a vascular network) within a porous scaffold. Tissues that have been successfully engineered are largely limited to relatively thin or avascular constructs such as skins and cartilages [51].

Many strategies have been explored to promote neovascularization in a porous scaffold, including the use of natural polymers [90], encapsulation of angiogenic growth factors [81, 91-93], embedment of endothelial cells or stem cells [94, 95], and inclusion of proper genes [96]. While these angiogenic adjuncts have been shown to significantly enhance vascularization, only a few studies have directly examined how the physical properties of a scaffold affect the formation of a vascular network *in vivo*. To this end, the Hofstetter and Homann groups reported that pores of 140  $\mu\text{m}$  or larger in size supported more effective ingrowth of endothelium when ceramic and poly(ether ester) block-copolymer scaffolds were used, respectively [97, 98]. However, like the aforementioned reports on progenitor cells, the scaffolds used in these studies were also troubled by their non-uniform pores and structures, including a broad range of distribution (up to 50%

variation) in pore sizes, which tended to compromise the robustness of conclusions derived from the experimental data. Recently, several groups have fabricated scaffolds with relatively uniform pore sizes (about 10% deviation) and used them to study neovascularization. For example, Ratner and co-workers investigated PHEM-based scaffolds with a set of pore sizes up to 160  $\mu\text{m}$  in diameter and they claimed an optimal pore size of 30–40  $\mu\text{m}$  for angiogenesis with minimal fibrosis [21, 22]. Dong and co-workers used  $\beta$ -tricalcium phosphate scaffolds with pore sizes of 337, 415, 557 and 632  $\mu\text{m}$ , and they found that pores smaller than 400  $\mu\text{m}$  limited the growth of blood vessels but induced more fibrosis [99]. The results from these two studies were inconsistent and somewhat controversial to each other. In addition, pore sizes from approximately 150–350  $\mu\text{m}$  remains largely un-explored.

Based on these prior reports, I will discuss in Section 3.3 the use of PLGA inverse opal scaffolds with uniform pore sizes (<1% deviation) as a well-defined and controllable system to systematically evaluate the effect of different sizes on the pattern and degree of neovascularization *in vivo* without the involvement of angiogenic growth factors or angiogenic cells. A model for neovascularization in these scaffolds is further proposed, which may potentially offer a guideline for future design of porous scaffolds to promote neovascularization *in vivo*.

### **3.2. The Effect of Pore Size on Progenitor Cell Differentiation *in vitro***

In general, the differentiation of progenitor and stem cells is dependent on the morphology, geometry, and surface properties of a scaffold [100-102]. Here, as an initial investigation, I chose to focus on the differentiation of MC3T3 preosteoblasts as these cells are widely used for bone tissue engineering and their responses to various types of scaffolds are well-characterized [70, 103-105]. To elucidate the effect of pore size and uniformity on the differentiation of preosteoblasts, I prepared three types of apatite-

coated PLGA/HAp composite scaffolds: inverse opal scaffolds with uniform pore sizes of 211  $\mu\text{m}$  and 313  $\mu\text{m}$ , respectively, and non-uniform scaffolds with an average pore size of slightly over 200  $\mu\text{m}$  [49]. MC3T3 preosteoblasts were seeded into each type of scaffolds, cultured in an osteogenic medium, and alkaline phosphatase (ALP) activity and the amounts of secreted ECM during culture were then evaluated.

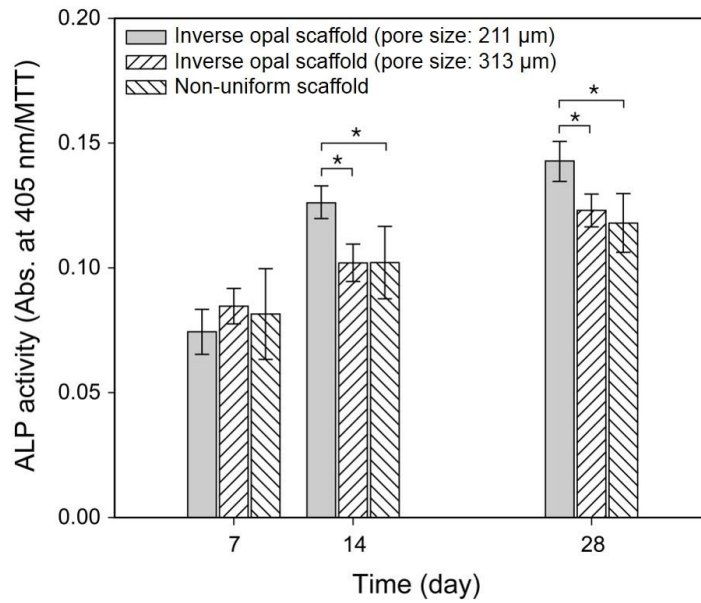


**Figure 3.1.** ALP activity of the preosteoblasts cultured in three different types of apatite-coated PLGA/HAp composite scaffolds at 7, 14, and 28 days of culture ( $n = 3$ ). \*Statistical significance between the two groups ( $p < 0.05$ ).

I first quantitatively evaluated the differentiation of preosteoblasts in the scaffolds using assays based on ALP activity. ALP is a well-known indicative marker for osteogenic differentiation. As shown in Figure 3.1, there was no significant difference in ALP activity among the samples at 7 days of culture. However, the cells in inverse opal scaffolds with a pore size of 211  $\mu\text{m}$  exhibited significantly higher ALP activity than other scaffolds at 14 and 28 days of culture, whereas there was still no significant difference in ALP activities between the non-uniform scaffolds and the inverse opal

scaffolds with a pore size of 313  $\mu\text{m}$ . The ALP test quantitatively confirmed the better performance of inverse opal scaffolds with a pore size of around 200  $\mu\text{m}$  for the differentiation of preosteoblasts. Nevertheless, such biochemical assays could only reflect the collective cell responses in an entire scaffold. In order to understand the effect of individual pores on the differentiation of MC3T3 preosteoblasts, microscopic examinations were further conducted for qualitative analyses.

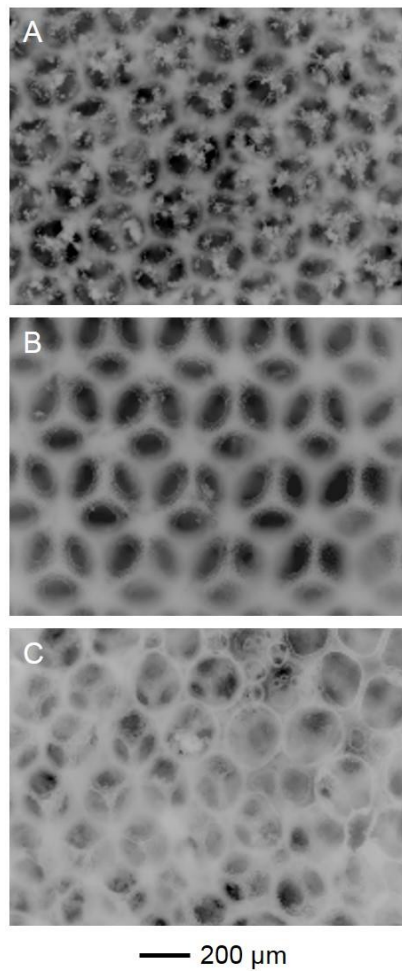


**Figure 3.2.** Transmission optical micrographs of MC3T3 preosteoblasts/scaffold constructs at 28 days of culture for inverse opal scaffolds with pores of (A) 211  $\mu\text{m}$  and (B) 313  $\mu\text{m}$ , respectively, in size, and (C) a non-uniform scaffold.

Figure 3.2 shows optical micrographs of the three types of scaffolds after 28 days of differentiation for the preosteoblasts. While a large amount of mineral was found in the inverse opal scaffold with a pore size of 211  $\mu\text{m}$  (Figure 3.2A), very little mineral was observed in the inverse opal scaffold with a pore size of 313  $\mu\text{m}$  (Figure 3.2B) or in the non-uniform scaffold (Figure 3.2C). Since mineral was observed in the entire inverted opal scaffold with a pore size of 211  $\mu\text{m}$ , it indicates that there was uniform differentiation for the preosteoblasts and subsequent secretion of mineral by the cells.

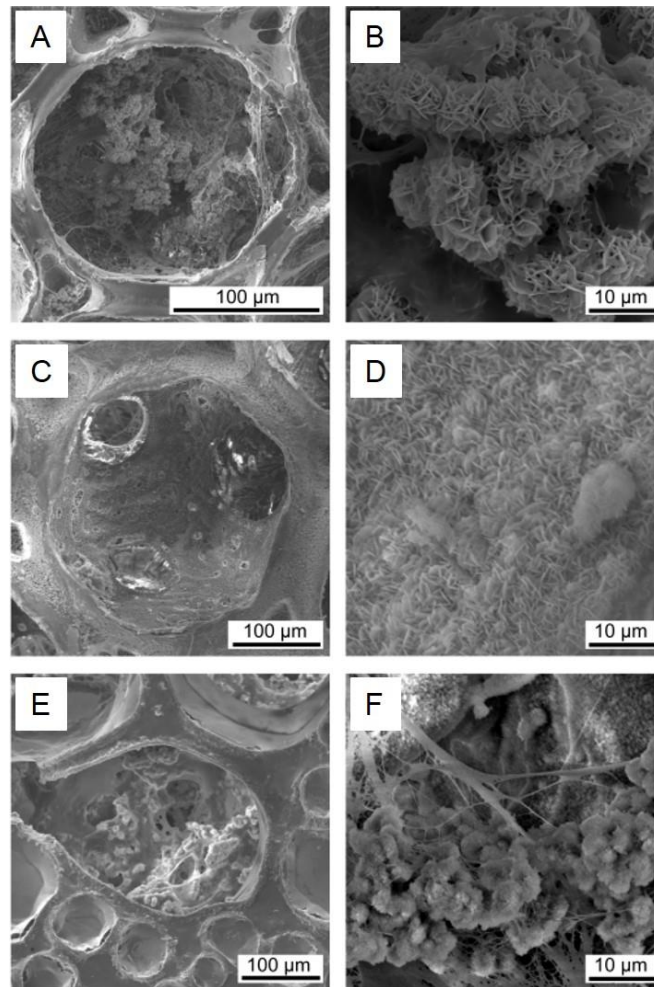


**Figure 3.3.** SEM images of the preosteoblast/scaffold constructs at 28 days of culture for inverse opal scaffolds with pores of (A, B) 211  $\mu\text{m}$  and (C, D) 313  $\mu\text{m}$ , respectively, in size, and (E, F) a non-uniform scaffold.

Figure 3.3 shows SEM images of the cell/scaffold constructs after 28 days of culture. Consistent with observations from optical microscopy (Figure 3.2), a large amount of complex structures containing both inorganic and organic ECM was found inside the pores of the inverse opal scaffold with a pore size of 211  $\mu\text{m}$  (Figure 3.3, A and B). By contrast, only a limited amount of mineral was deposited on the wall of the inverse opal scaffold with a pore size of 313  $\mu\text{m}$  (Figure 3.3, C and D). Interestingly, a moderate amount of mixture of inorganic and organic ECM was observed in the large pores (around 200  $\mu\text{m}$ ) of the non-uniform scaffold, whereas most of the smaller pores and/or larger pores in the scaffold were free of visible ECM or occluded only by the fibrous organic ECM (Figure 3.3, E and F). These observations suggested that the apatite-decorated pores with sizes around 200  $\mu\text{m}$  could indeed facilitate the secretion of both inorganic and organic ECM, which corresponded to the most effective osteogenic differentiation where both organic (*e.g.*, collagen and other bone marker proteins such as osteocalcin, bone sialoprotein, and osteopontin) and inorganic (*e.g.*, bio-apatite) components would be present [106]. On the contrary, large pores (around 300  $\mu\text{m}$ ) seemed to be more favorable for the secretion of inorganic ECM and small pores were better suited for the secretion of organic fibrous ECM.

An important notion can therefore be concluded: the secretion pattern of the preosteoblasts is largely determined by the size of an individual pore in which the cells reside, rather than the bulk properties of a scaffold (*e.g.*, the average pore size). This notion in turn, emphasizes the significance of the capability to precisely engineer the physical parameters of an inverse opal scaffold.

### **3.3. The Effect of Pore Size on Neovascularization *in vivo***

In this study, PLGA inverse opal scaffolds were fabricated with four different sets of pore sizes of 79, 147, 224, and 312  $\mu\text{m}$ , respectively [107]. A 20 wt.% PLGA solution

in 1,4-dioxane was used as the infiltration solution so that the surface pore size was 75–85% of the pore size. As a result, the four groups of inverse opal scaffolds had surface pore sizes of approximately 62, 115, 175 and 243  $\mu\text{m}$ , respectively. Additionally, for all scaffolds used in the present work, the gelatin microspheres were fused at 70  $^{\circ}\text{C}$  for 1 h, and the window size was 20–25% of the pore size, *i.e.*, the window sizes were approximately 18, 33, 50 and 70  $\mu\text{m}$ , respectively, for the scaffolds with pore sizes of 79, 147, 224, and 312  $\mu\text{m}$ .

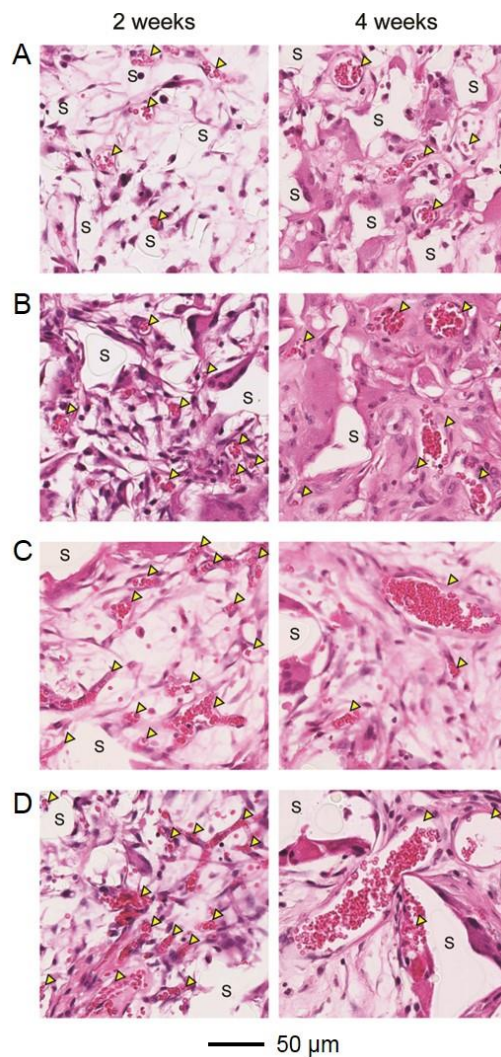


**Figure 3.4.** Representative hematoxylin and eosin stained sections of subcutaneously implanted scaffolds with pores of (A) 79  $\mu\text{m}$ , (B) 147  $\mu\text{m}$ , (C) 224  $\mu\text{m}$ , and (D) 312  $\mu\text{m}$ , respectively, in pore

size, at 2 weeks (left column) and 4 weeks (right column) post implantation. All the images were obtained from sections approximately 200  $\mu\text{m}$  in depth from the top surfaces of the scaffolds. Blood vessels are indicated by yellow arrowheads, whereas 'S' indicates the scaffolds.

The inverse opal scaffolds were then subcutaneously implanted at the dorsal sides of nude mice. Each scaffold was positioned such that the top surface was against the layer of connective tissue underlying the dermis where the majority of blood vessels resided. In this case, the vessels could only invade into the bulk of the scaffold through the pores on the top surface [107].

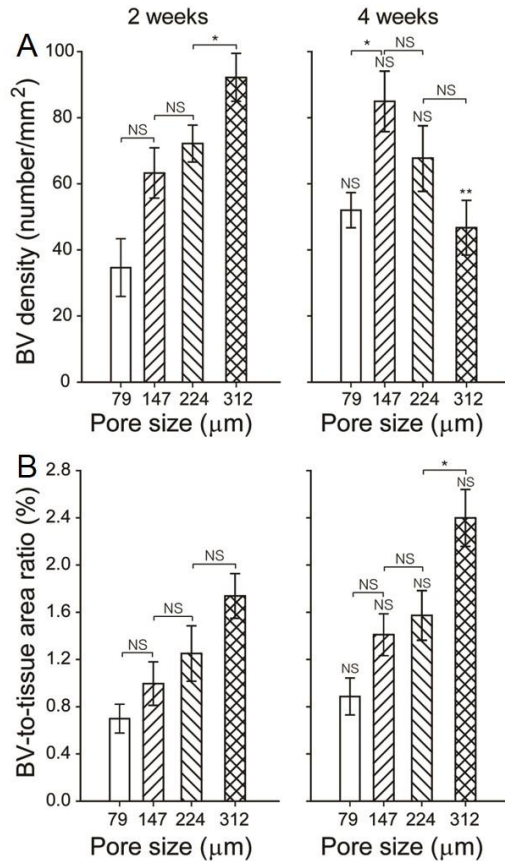


**Figure 3.5.** Plots of (A) blood vessel density and (B) blood vessel-to-tissue area ratio as a function of pore size at 2 and 4 weeks post implantation, both of which were measured from hematoxylin and eosin stained tissue sections approximately 200  $\mu\text{m}$  in depth from the top surfaces of the scaffolds. \*Statistical significance between two groups ( $p < 0.005$ ), whereas NS

*means not statistically significant ( $p > 0.005$ ). \*\*Statistical significance relative to the value of the samples at 2 weeks. For each sample, at least 200 blood vessels from 8 tissue sections were examined ( $n = 4$ ).*

Figure 3.4 shows bright-field optical micrographs of representative hematoxylin and eosin stained samples obtained from sections approximately 200  $\mu\text{m}$  away from the top surface of the scaffolds at 2 and 4 weeks post implantation. Nascent vessels extending into the implanted scaffolds were histologically confirmed by the presence of red blood cells surrounded by continuous rings of vascular cells (indicated by arrowheads). Scaffolds were identified by the areas where no stains could be observed (indicated by ‘S’). At 2 weeks post implantation, although a number of blood vessels were observed to penetrate into the pores of all implanted scaffolds (Figure 3.4, left column), scaffolds with large pore sizes (224  $\mu\text{m}$  and 312  $\mu\text{m}$ ) apparently supported higher densities of blood vessels than scaffolds with small pore sizes (79  $\mu\text{m}$  and 147  $\mu\text{m}$ ), with multiple blood vessels invading individual pores. These initially formed blood vessels had an average diameter of about 15  $\mu\text{m}$ , irrespective of the pore size of the scaffold. At 4 weeks post implantation, remarkable differences were observed in both the number and size of blood vessels in the implanted scaffolds with different pore sizes (Figure 3.4, right column). The mean diameter of blood vessels in scaffolds with small pore sizes increased to approximately 25  $\mu\text{m}$ . Interestingly, while scaffolds with large pore sizes supported the formation of blood vessels with a mean diameter of approximately 40  $\mu\text{m}$ , there was a decrease in the number of small vessels relative to the samples at 2 weeks post implantation.

Histology sections were then utilized to quantitatively assess both the blood vessel density and the blood vessel-to-tissue area ratio at the same depth (about 200  $\mu\text{m}$ ) from the top surface of the scaffolds. The blood vessel density was calculated as the number of blood vessels per unit area of the scaffold/tissue section (in the unit of

number/mm<sup>2</sup>). The blood vessel-to-tissue area ratio was defined as the percentage of total areas of all the blood vessels in a scaffold/tissue section against the area of that section (expressed as %).

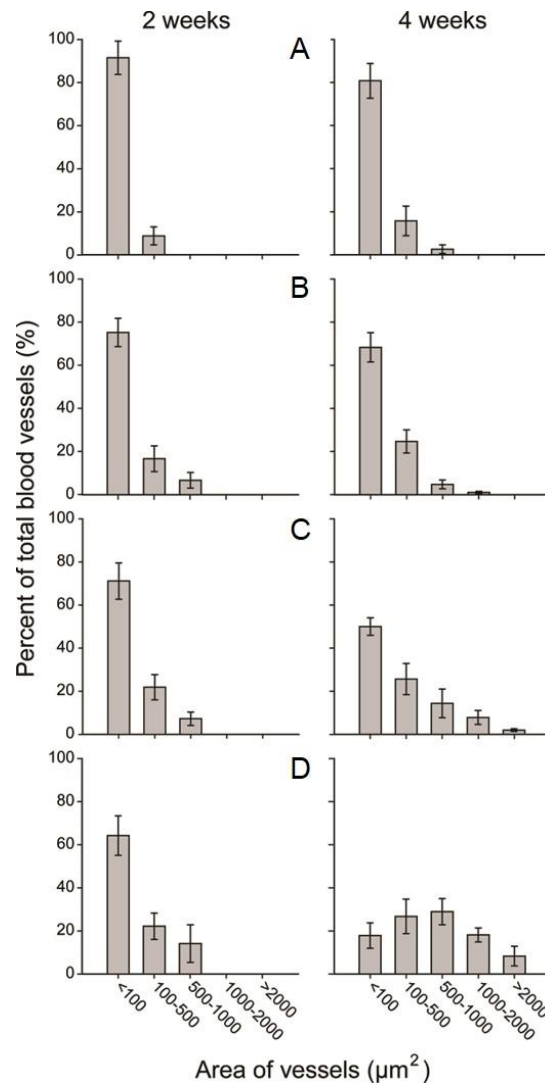


**Figure 3.6.** Plots showing distributions of blood vessel areas in the scaffolds with pores of (A) 79  $\mu\text{m}$ , (B) 147  $\mu\text{m}$ , (C) 224  $\mu\text{m}$ , and (D) 312  $\mu\text{m}$ , respectively, in size, at 2 weeks (left column) and 4 weeks (right column) post implantation. The data were measured from hematoxylin and eosin stained tissue sections approximately 200  $\mu\text{m}$  in depth from the top surfaces of the scaffolds. For each sample, at least 200 blood vessels from 8 tissue sections were examined ( $n = 4$ ).

Figure 3.5A shows plots of blood vessel density as a function of pore size at 2 and 4 weeks post implantation. At 2 weeks, scaffolds with large pore sizes were found to induce a higher density of blood vessels in the scaffolds than scaffolds with small pore sizes. Particularly, the scaffolds with a pore size of 312  $\mu\text{m}$  showed the highest density of blood vessels among the four samples. However, at 4 weeks, the densities of blood vessels in scaffolds with large pore sizes appeared to decrease whereas the densities of vessels in scaffolds with small pore sizes greatly increased. Figure 3.5B shows plots of the blood vessel-to-tissue area ratio as a function of pore size at 2 and 4 weeks post implantation. The ratio was observed to increase over time in all scaffolds. Despite the reduction in blood vessel densities for scaffolds with large pores at 4 weeks, the scaffolds with a pore size of 312  $\mu\text{m}$  showed substantially higher blood vessel-to-tissue area ratio than other scaffolds, which could be attributed to the presence of a number of large vessels.

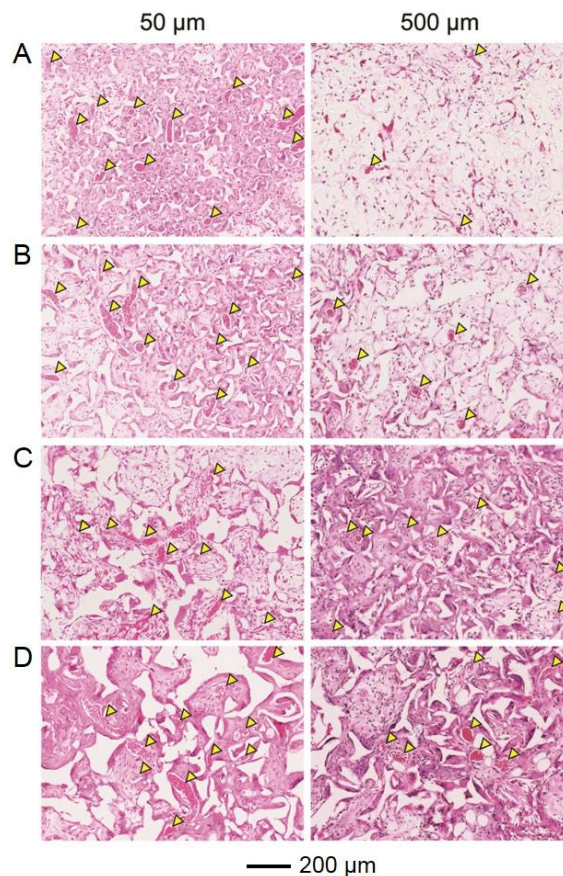


**Figure 3.7.** Representative hematoxylin and eosin stained tissue sections of subcutaneously implanted scaffolds with pores of (A) 79  $\mu\text{m}$ , (B) 147  $\mu\text{m}$ , (C) 224  $\mu\text{m}$ , and (D) 312  $\mu\text{m}$ , respectively, in size, at 4 weeks post implantation. The sections were around 50  $\mu\text{m}$  (left column) and 500  $\mu\text{m}$  (right column) in depth from the top surfaces of the scaffolds. Blood vessels are indicated by arrowheads.

Indeed, this argument was confirmed by quantifying the distribution of blood vessel areas in these scaffolds (Figure 3.6). The majority of nascent vessels in all the scaffolds at 2 weeks had small cross-sectional areas ( $<100 \mu\text{m}^2$ ). At 4 weeks, by contrast, scaffolds with large pores showed a markedly different distribution in vessel areas, moving towards blood vessels with larger areas. Particularly, in the case of scaffolds with a pore size of 312  $\mu\text{m}$ , blood vessels with areas ranging from 500–1000  $\mu\text{m}^2$  occupied the highest percentage.

To further assess the effect of pore size on the degree of neovascularization, the ingrowth of blood vessels in the scaffolds at 4 weeks post implantation was examined at other two different depths of about 50 and 500  $\mu\text{m}$ , respectively, from the top surface of the scaffolds. At a depth of 50  $\mu\text{m}$ , there were a number of large blood vessels present irrespective of the pore size of the scaffolds (Figure 3.7, left column). The densities of these vessels were lower than those at a depth of 200  $\mu\text{m}$  (Figure 3.8A), while the blood vessel-to-tissue area ratios of the vessels were remarkably larger (Figure 3.8B). At a depth of 500  $\mu\text{m}$ , noticeably fewer blood vessels were observed for scaffolds with small pore sizes (Figure 3.7, A and B, right column, and Figure 3.8, A and B) relative to the depth of 200  $\mu\text{m}$  (Figure 3.4, A and B, right column and Figure 3.5A). By contrast, the difference in the densities of blood vessels was less significant for scaffolds with large pore sizes at different depths (Figure 3.7, C and D, right column *versus* Figure 3.4, A and B, right column, and Figure 3.8A *versus* Figure 3.5A, right panel), suggesting that the large pore sizes could facilitate the invasion of blood vessels deeply into the bulk of the

scaffolds. Scaffolds with large pore sizes also had higher blood vessel-to-tissue area ratios at this depth of 500  $\mu\text{m}$  than scaffolds with small pore sizes (Figure 3.8B) although the ratios were smaller in all cases in comparison with those close to the surface region (Figure 3.7, left column, and Figure 3.5B, right panel).

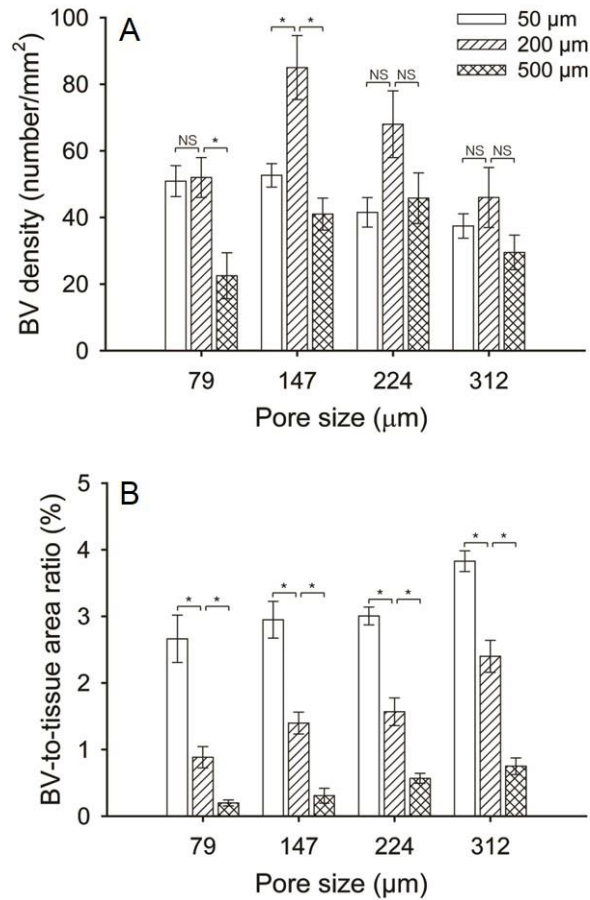


**Figure 3.8.** Plots of (A) blood vessel density and (B) blood vessel-to-tissue area ratio as quantified from histology analyses. \*Statistical significance between two groups ( $p < 0.005$ ), whereas NS means not statistically significant ( $p > 0.005$ ). For each sample, at least 200 blood vessels from 8 tissue sections were examined ( $n = 4$ ).

The histology and histomorphometric analyses suggested that the pore size of a scaffold could directly regulate the pattern and degree of neovascularization. Scaffolds

with pore sizes smaller than 200  $\mu\text{m}$  favored the formation of vascular networks with small vessels at high densities close to the surface, while vascular networks with large blood vessels and low densities could grow deeply into scaffolds with pore sizes larger than 200  $\mu\text{m}$ . Figure 3.9 shows the proposed mechanism to explain these observations on the development of neovasculature in inverse opal scaffolds with different size parameters. It was assumed that, the surface pore size, pore size, and window size should all have played their respective roles in regulating the neovascularization process in a 3D porous scaffold.

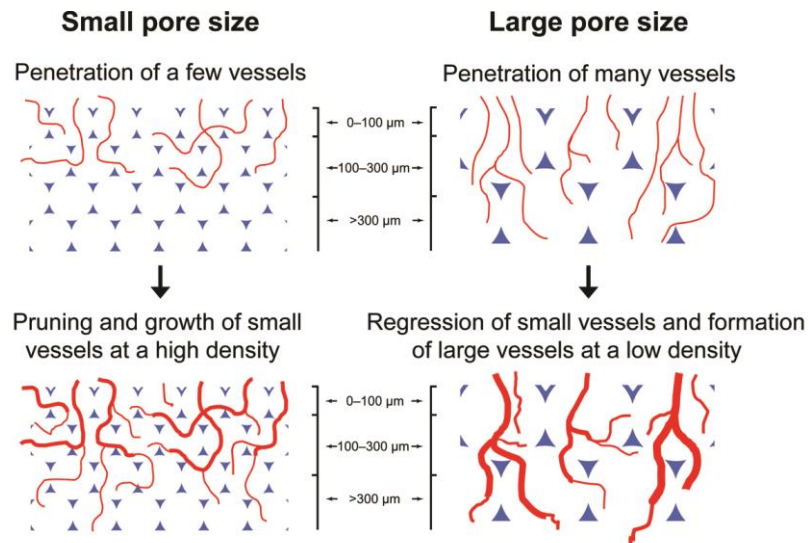


**Figure 3.9.** Schematic illustrations showing the proposed mechanism via which the size parameters of a scaffold affects neovascularization *in vivo*.

First, all four types of scaffolds could have allowed the initial penetration of similar numbers of vessels into the pores on the surface despite their difference in surface pore sizes, because in the present study the percentage of open space was about the same in each case. Some of the vessels competitively developed into large and interconnected vessels while others regressed when the nascent vasculature was consisted of too many small vessels [108-112]. This argument is supported by the observation that large vessels

in low quantities formed in the scaffolds at 4 weeks close to the very top surface (50  $\mu\text{m}$  in depth) where the vessels essentially encountered no barriers during the progression (Figure 3.7, left column and Figure 3.8, A and B). Although the total number of vessels initially penetrated into each scaffold was similar, scaffolds with small pore sizes had fewer numbers of vessels per pore. Such lower densities of vessels should have resulted in more vessels to grow and prune by themselves rather than forming large vessels by connecting with others, due to the separation by the polymer walls of the pores. Indeed, the density of blood vessels decreased (Figure 3.8A) while the blood vessel-to-tissue area ratios increased (Figure 3.8B) as the pore size increased in these scaffolds.

After the initial infiltration of blood vessels from the top surface of the scaffolds, the pore size should then play an important role when these vessels further branched and penetrated deeper. It is obvious that it would take a substantially longer time for nascent vessels to cross the spherical pores at the surface of a scaffold when the pore size was increased. As a result, during the same period of time, the blood vessels in scaffolds with large pore sizes were still growing and interconnecting with other vessels whereas the vessels in scaffolds with small pore sizes might have already encountered the bottom of the spherical pores at the surface and started to enter the pores underneath through the windows.

At this point, the window size would then become a critical parameter. For scaffolds with small pore sizes, after the invading tissues and nascent vessels had reached the bottom of the pores at the surface, they could not efficiently penetrate into the pores underneath because of the small windows, leading to three possible outcomes: *i*) a number of vessels would become trapped in a few layers of pores close to the surface as there were more vessels penetrating and branching than those that could progress even deeper; *ii*) the physical barriers imposed by the polymer backbone of the scaffolds would eventually limit the number of vessels penetrating deeply into the scaffolds, resulting in low densities of blood vessels in the bulk; and *iii*) as the vessels penetrated more deeply,

they tended to be separated from each other in individual pores, and therefore could only grow by themselves rather than interconnecting with other vessels. On the contrary, for scaffolds with large pore sizes, the sufficiently large window sizes would allow the invasion of multiple vessels into individual pores underneath, making it possible for the vessels to merge with others.

These two arguments regarding the effects of pore size and window size are supported by the following observations. Firstly, scaffolds with large pore sizes (224 and 312  $\mu\text{m}$ ) had higher blood vessel densities than those with small pore sizes at a depth of 200  $\mu\text{m}$  at 2 weeks because of the absence of physical barriers for the invading vessels in these scaffolds at such a depth. Nevertheless, for scaffolds with pore sizes of 147 and 79  $\mu\text{m}$ , the vessels had already encountered one and two layers of pores at such a depth, respectively, and a majority of them were blocked by the polymer backbone while some others could penetrate more deeply through the small windows. As more growing or branching vessels with small areas progressed from the top surface, most of them became trapped around this depth in scaffolds with small pore sizes at 4 weeks (Figures 3.4–3.6). By contrast, more vessels were able to penetrate to this depth in scaffolds with large pore sizes initially at 2 weeks, leading to decreased numbers of vessels and increased vessel-to-tissue ratios at 4 weeks due to merging and regressing (Figures 3.4–3.6). Secondly, while both the blood vessel densities and blood vessel-to-tissue area ratios were reduced in all types of scaffolds, the reduction in scaffolds with small pore sizes was more pronounced due to the obstruction by multiple layers of pores (Figure 3.7, right column and Figure 3.8). However, all of these vessels might have not been able to grow and interconnect with others during the period of time tested (4 weeks). This is why the blood vessel-to-tissue area ratios at 500  $\mu\text{m}$  below the surface for all the scaffolds (Figure 3.7, right column and Figure 3.8B) were low compared to those close to the surface (Figure 3.4, right column and Figure 3.5, right column). Lastly, in addition to endothelial cells and pericytes, the migration of non-vascular cells (*e.g.*, fibroblasts) is also one of the

factors critical to neovascularization in a scaffold. As these peripheral cells migrate to the inner space of a scaffold, they tend to become hypoxic due to an environment with a low level of oxygen and thus secrete angiogenic factors (*e.g.*, vascular endothelial growth factor, VEGF) [113]. These chemical cues can function to recruit endothelial (progenitor) cells, facilitating the development of a neovasculature. Therefore, the limited infiltration of non-vascular cells due to the small surface pore sizes, pore sizes, as well as window sizes could possibly count for another reason why poorer neovascularization developed in scaffolds with small pore sizes (note that in Figure 3.7, A and B, right column, the scaffolds with small pore sizes were poorly cellularized at the depth of 500  $\mu\text{m}$ ).

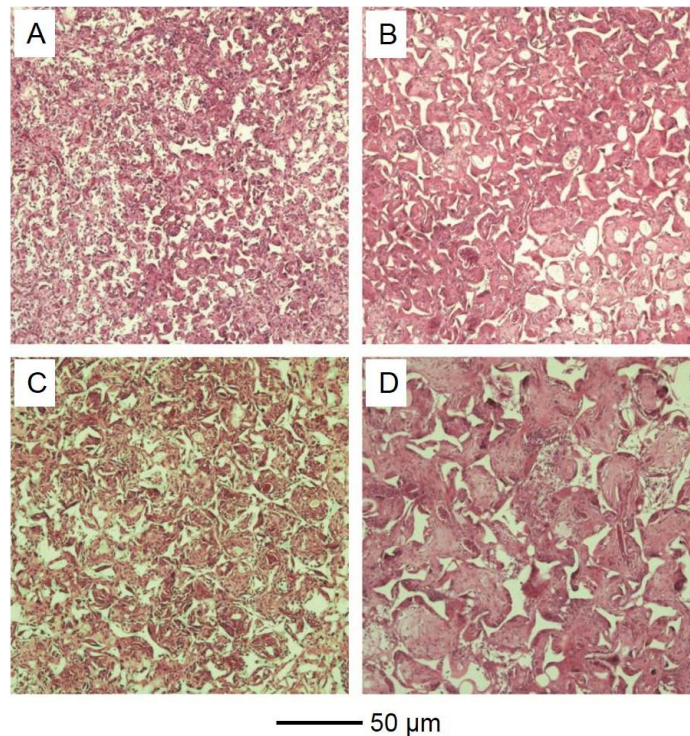


**Figure 3.10.** Transmission bright-field optical micrographs showing representative hematoxylin and eosin stained tissue sections of subcutaneously implanted scaffolds with pores of (A) 79  $\mu\text{m}$ , (B) 147  $\mu\text{m}$ , (C) 224  $\mu\text{m}$ , and (D) 312  $\mu\text{m}$ , respectively, in size, at 4 weeks post implantation.

It should be pointed out that, during the 4-week period of *in vivo* experiments, the PLGA scaffolds did not experience noticeable changes in their overall morphologies although slight deformation in some of the pore could be observed, presumably due to sample preparation for histology (*i.e.*, dehydration and heating during the paraffin section procedures). As shown by the low-magnification bright-field optical images of hematoxylin and eosin stained sections at 4 weeks post implantation (Figure 3.10), all four types of scaffolds largely retained their structural integrity including the uniform pores and windows. According to my own experience, the collapse of these scaffolds (*i.e.*, when they lost their mechanical strength) for subcutaneous implantation *in vivo* typically did not occur until roughly 7–10 weeks post implantation. Therefore, the effect of scaffold degradation could be neglected in studying the pattern and degree of neovascularization.

### 3.4. Summary

Owing to their uniform pore sizes and highly reproducible structure, PLGA inverse opal scaffolds are well-suited as model systems for studies involving the effects of size-related parameters on the behaviors of cells and/or tissues. Consistent with expectation, the osteogenic differentiation of MC3T3 preosteoblasts was regulated by the size of individual pores of a porous scaffold. Therefore, in a non-uniform scaffold, the responses of the cells might be averaged by the presence of both small and large pores when the scaffold is assessed as a single unit. By contrast, for inverse opal scaffolds with uniform pores, the cells residing in all pores should more or less follow the same pathway and lineage commitment. Similarly, the differences in pore size and window size were also found to influence the degree and pattern of neovascularization when they were implanted *in vivo*.

These two studies are simply proof-of-concept experiments to examine how the physical parameters of a porous scaffold might affect the cells/tissues residing in it. More comprehensive and sophisticated investigations still need to be conducted to fully understand these effects.

Although it was observed that the MC3T3 preosteoblasts showed different levels of ALP activity and ECM secretion, the changes in the gene expression patterns of the cells during differentiation remain unclear. Therefore, further studies should include analyses from the perspective of cell biology, such as polymerase chain reaction (PCR), and immunocytochemistry, to examine the regulation of specific genes and proteins, such as osteocalcin, osteopontin, Runx2, and bone sialoprotein. Then, other types of progenitor cells such as endothelial progenitor cells, preadipocytes, as well as less terminally differentiated stem cells including mesenchymal stem cells (MSCs) and ESCs should be studied for their differentiation into multiple lineages in inverse opal scaffolds with different size parameters. More interestingly, each of the three sizes (pore size, surface pore size, and window size) should be individually adjusted to examine their respective effects. For example, holding the pore and window sizes constant while changing the surface pore size could be used to evaluate the relationship between the surface pore size and cell/tissue penetration from the surface of a scaffold; alternatively, varying only the pore size or window size while holding the other two parameters constant could give respective information on how these two sizes modulate cell/tissue behavior. Once the influence of each of these three sizes has been determined, it would then be possible to combine multiple parameters in an effort to more precisely regulate cell/tissue responses via scaffold design.

### **3.5. Experimental**

#### **3.5.1. Materials and Chemicals**

Gelatin (type A, from porcine skin), Span<sup>®</sup> 80, and toluene were all obtained from Sigma-Aldrich and used as-received for the fabrication of gelatin microspheres with uniform sizes. PLGA (lactide:glycolide = 75:25,  $M_w = 66,000\text{--}107,000$ ) and 1,4-dioxane were also obtained from Sigma-Aldrich and used as-received for the fabrication of scaffolds. All of the chemicals for the preparation of 10xSBF were purchased from Sigma-Aldrich. The water used in all fabrications was obtained by filtrating through a set of cartridges (Millipore). The PVC tubes and glass microcapillary tubes were purchased from VWR International. Syringe needles were obtained from BD Biosciences.

### **3.5.2. Preparation of PLGA Inverse Opal Scaffolds and Non-Uniform Scaffolds**

The PLGA and apatite-coated PLGA/HAp composite inverse opal scaffolds and non-uniform scaffolds were fabricated as described in Chapter 2 [49, 53, 59, 85].

### **3.5.3. Cell Culture in Inverse Opal Scaffolds and Characterization**

MC3T3-E1 preosteoblasts (ATCC) were maintained in an  $\alpha$ -MEM (Invitrogen) supplemented with 10 vol.% FBS and 1 vol.% P/S. Prior to cell seeding, the scaffolds were wetted and sterilized by immersion in 70 vol.% ethanol for 2 h, washed with PBS (Invitrogen) three times and stored in PBS until use. Approximately  $1.6 \times 10^5$  cells were used for seeding into each scaffold using a spinner flask (Corning). The cell-seeded scaffolds were then transferred to 12-well plates (not treated for tissue culture, BD Biosciences; 1 scaffold per well), and cultured in an osteogenic differentiation medium supplemented with 300  $\mu\text{M}$  L-ascorbic acid, 10 mM  $\beta$ -glycerol phosphate, and 10 nM dexamethasone (Sigma-Aldrich). The cultures were maintained in an incubator at 37 °C in a humidified atmosphere containing 5% CO<sub>2</sub> for up to 4 weeks and the medium was changed every other day.

### **3.5.4. Alkaline Phosphatase Assay**

ALP assays were performed at 7, 14, and 28 days after cell seeding using the p-nitrophenyl phosphate (pNPP) method. Briefly, at specific time points, scaffolds ( $n = 3$  per group per time point) were washed with PBS twice and the cells were lysed in 1 mL of PBS containing 0.1 M glycine, 1 mM  $\text{MgCl}_2$  and 0.05 vol.% Triton X-100 (Sigma-Aldrich). Cell lysates were stored at  $-20\text{ }^\circ\text{C}$  until use. The pNPP solution (1 mg/mL) in 0.2 M Tris buffer (Invitrogen) was made from SIGMAFAST<sup>TM</sup> pNPP tablets (Sigma-Aldrich) according to the manufacturer's instructions. Reactions were carried out in a 96-well plate by mixing 200  $\mu\text{L}$  of pNPP solution and 50  $\mu\text{L}$  of cell lysates in each well, and the plate was kept at  $37\text{ }^\circ\text{C}$  for 2 h. Absorbance was measured at 405 nm using a spectrophotometer (Infinite 200, TECAN) immediately after reactions.

### **3.5.5. Animals and Surgical Procedures**

Sixteen adult male athymic nude mice (7–8 weeks old, Harlan Laboratories Inc., Indianapolis, IN) were randomly divided into eight groups (I–VIII) with two animals in each group. Animals in all groups were anesthetized by administration of gaseous isoflurane (2%, Butler Inc., Dublin, OH) and aseptically prepared for implantation of scaffolds. Two parasagittal incisions were made on the dorsum of each animal approximately 1 cm rostral to the hip and 0.5 cm lateral to the spine. Subcutaneous pockets were created lateral to both incisions by separating the subcutaneous fascial plane using blunt dissection. One scaffold was inserted into each subcutaneous pocket (*i.e.*, two scaffolds per animal) and positioned such that the top surface of the scaffold was against the layer of connective tissue underlying the dermis. Animals in Groups I and V, II and VI, III and VII, and IV and VIII received inverse opal scaffolds with pore sizes of 79, 147, 224, and 312  $\mu\text{m}$ , respectively. Skin incisions were then closed with 5-0 Ethilon suture (Ethicon, Somerville, NJ) and secured using VetBond dermal adhesive (3M, St. Paul, MN). At 2 weeks post implantation, all animals in Groups I-IV were euthanized using sodium pentobarbital (200 mg/kg, intraperitoneal injection) prior to explantation of

the scaffolds. At 4 weeks post implantation, all animals in Groups V-VIII were similarly euthanized prior to explantation of the scaffolds. All surgical procedures were performed in accordance with the National Institutes of Health (NIH, Bethesda, MD) Guidelines and were approved by the Washington University Animal Studies Committee.

### **3.5.6. Histological Assessment and Histomorphometric Analysis**

Following explantation, the PLGA scaffolds were fixed in 4 vol.% formaldehyde in PBS (Invitrogen) for 24 h, dehydrated, embedded in paraffin wax, and then serially sectioned (5  $\mu\text{m}$  in thickness). The collected cross sections were mounted on glass slides and stained with hematoxylin and eosin to examine infiltration of host tissues and vasculature into the scaffolds. The as-prepared slides were imaged using a Nanozoomer 2.0-HT slide scanner (Hamamatsu, Hamamatsu City, Japan). The acquired images were utilized to quantify both the blood vessel density and the blood vessel-to-tissue area ratio in the scaffolds using the ImageJ software (National Institute of Health, NIH, Bethesda, MD). Specifically, to calculate the density, blood vessels were manually counted and the number was normalized against the area of the scaffold/tissue section, and expressed in the unit of number per  $\text{mm}^2$ . The blood vessel-to-tissue area ratio was calculated by normalizing the total area of all the blood vessels against the area of the scaffold/tissue section, and expressed in the form of percentage (%). For each sample, at least 200 blood vessels from 8 tissue sections randomly chosen were examined.

### **3.5.7. Statistical Analysis**

Results were reported as mean  $\pm$  standard deviation, unless otherwise noted. Comparisons were performed using ANOVA, followed by Fisher's least significant difference (LSD) test for paired comparisons between groups. Statistical significance was set at  $p < 0.005$  to account for multiple comparisons.

### **3.5.8. Scanning Electron Microscopy**

SEM (Nova NanoSEM 2300, FEI) was used to characterize the PLGA inverse opal scaffolds and scaffold/tissue constructs. Prior to imaging, the samples were sputter-coated with gold for approximately 60 s. Images were taken at an accelerating voltage of 5–10 kV.

# **CHAPTER 4**

## **PHOTOACOUSTIC MICROSCOPY FOR TISSUE ENGINEERING AND REGENERATIVE MEDICINE**

### **4.1. Introduction**

In Chapter 1, I stated that another major challenge in tissue engineering and regenerative medicine lies in the characterization of 3D tissue constructs once they have been prepared. Conventional methods relying on microtomy where serial sections are obtained from a 3D sample are laborious and the capability to reconstruct the 3D information is limited. As a result, non-invasive volumetric imaging modalities are needed in order to overcome these issues. Although many potent imaging techniques have been developed over the past century, issues persist. For example, while pure optical imaging modules such as confocal and multi-photon microscopy can achieve high resolution [114, 115], their penetration depths are typically confined to no more than a few hundred micrometers, and thus are most suited for pure biological imaging; on the other hand, while non-optical imaging modalities such as ultrasound, micro-CT, MRI and positron emission tomography (PET) are able to penetrate deep or even indefinitely, they are limited by relatively low resolution or ionizing irradiation [116-120]. As a result, PAM has gained increasing attention in recent years for its use in biomedical engineering [38, 39]. In essence, PAM combines optical and ultrasonic imaging, and therefore it can achieve both high resolution originated from the absorption contrast, and deep penetration depth due to the low scattering of acoustic waves by biological tissues.

In recent years, PAM has been widely used in biomedical imaging of blood vessels and melanomas because of their intrinsic pigmentation (hemoglobin and melanin, respectively) [121, 122]. However, there are essentially no previous reports on the use of

PAM in tissue engineering and regenerative medicine. My work therefore represents the very first demonstration of PAM in non-invasive and volumetric imaging and quantification of engineered 3D tissue/scaffold constructs.

In Section 4.2, I will give an overview of PAM, including its basic configuration, principle of operation, and general classification.

In Section 4.3, I will describe how PAM can be used for non-invasive characterization of melanoma cells grown in PLGA inverse opal scaffolds. Melanoma cells contain natural dark pigments melanin that can serve as an absorption contrast and thus enable label-free PAM of the cells. The capability of PAM to resolve melanoma cells in an entire PLGA inverse opal scaffold was demonstrated by comparing the distribution of the cells under two different seeding and culturing methods. The chronological imaging of the proliferation of melanoma cells in PLGA inverse opal scaffolds was further studied to understand the long-term interaction between the scaffolds and the cells. Quantitative analysis was then drawn from the volumetric PAM data and compared with the conventional, invasive MTT biochemical assay to verify its accuracy. This study serves as the basis for the subsequent work that PAM is indeed beneficial when thick 3D samples are involved.

In Section 4.4, I will present several staining techniques that can generate contrasts for other types of cells that do not contain natural pigments for PAM imaging. Specifically, MTT, a metabolic dye, can be used to stain almost all the living cells due to the capability of these cells to convert MTT to MTT formazan, a purple insoluble crystal that can serve as an efficient contrast agent for PAM. I will also discuss the applications of traditional chromogenic (immuno)cytochemistry techniques in 3D volumetric PAM imaging of fixed cells in PLGA inverse opal scaffolds.

PAM has also been extensively utilized to analyze blood vessels in a label-free manner thanks to the absorption contrast from hemoglobin in red blood cells for biomedicine. In Section 4.5, I will therefore extend the application of PAM to non-

invasively monitor the neovascularization process in PLGA inverse opal scaffolds *in vivo* in individual nude mice. By combining with optical coherence tomography (OCT), the structure of the scaffolds could be observed simultaneously.

In addition to imaging cells and tissues, it is sometimes necessary to characterize the alterations to the scaffolds themselves at high resolution and/or in a quantitative fashion. Such topic will be covered in Section 4.6, where studies are presented on the use of PAM to non-invasively image and quantify the degradation of individual PLGA inverse opal scaffolds doped with a contrast agent, MTT formazan. As an additional feature, it was possible to simultaneously resolve the development and remodeling of blood vessels in and around the scaffold region by using dual-wavelength scanning mode of PAM.

## 4.2. Photoacoustic Microscopy

In PAM, both the optical excitation and the ultrasonic detection are focused. The foci are configured coaxially and confocally. For each laser shot, time-resolved ultrasonic detection produces a one-dimensional (1D), depth-resolved image (A-line) without mechanical scanning. Thus, a 1D line scanning produces a 2D frame (B-scan) and a 2D raster scanning along the transverse plane generates complete volumetric (3D) data. Volumetric images can be viewed through projection images coded by amplitude of maximum (*i.e.*, maximum amplitude projection, MAP) or depth of maximum, or direct 3D rendering. A projection image is performed by typically projecting chosen signals from each A-line onto the transverse plane, although projections along other axes are possible as well. Usually, PAM aims at imaging millimeters in depth at micrometer-scale resolution. The axial resolution and the maximum penetration depth are inversely proportional to the central frequency of the ultrasonic transducer, and the lateral resolution is predominantly determined by the tighter focus of the dual foci.

A total of 5 custom-designed PAM systems were used for the studies discussed in this Chapter: an acoustic-resolution PAM (AR-PAM) [121], an optical-resolution PAM (OR-PAM) [123, 124], a subwavelength-resolution PAM (SW-PAM) [125], a hybrid system combining OR-PAM and fluorescence confocal microscopy (OR-PAM-FCM) [126], and a hybrid system combining OR-PAM and OCT (OR-PAM-OCT) [127].

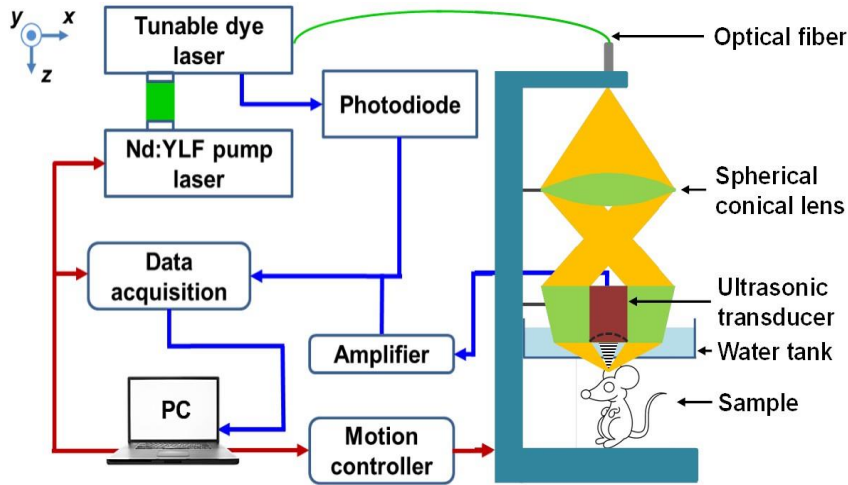


**Figure 4.1.** A schematic showing the configuration of an AR-PAM.

A schematic of the AR-PAM is shown in Figure 4.1. Optical excitation is provided by a tunable dye laser (pulse width: 7 ns; repetition rate: 5 kHz; CBR-D, Sirah, Kaarst, Germany) pumped by a Nd:YLF laser (INNOSLAB, Edgewave, Würselen, Germany). The excitation is implemented through a dark-field illumination, and the light is reshaped by a conical lens to form a ring pattern [37, 128]. The ring-shaped light is then weakly focused into the sample by an optical condenser. The generated photoacoustic signals are detected using a focused ultrasonic transducer (central frequency: 50 MHz; V214-BB-RM, Olympus NDT, Waltham, MA), which is located in the center of the optical condenser. The optical and ultrasonic foci are configured coaxially and confocally. The optical focal spot size was about 2 mm in diameter in a clear medium, much larger than the 45- $\mu\text{m}$  ultrasonic focus, so the lateral resolution is

predominantly determined by the ultrasonic focus, the so-called “acoustic resolution”. The AR-PAM can achieve a lateral resolution of approximately 45  $\mu\text{m}$ , an axial resolution of approximately 15  $\mu\text{m}$ , and a penetration depth of more than 3 mm in soft tissues [37].

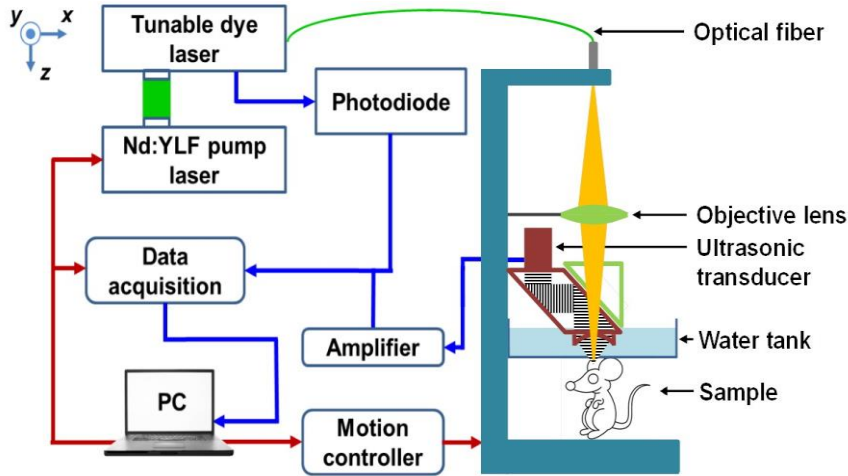


**Figure 4.2.** A schematic showing the configuration of an OR-PAM.

Figure 4.2 shows a schematic of the OR-PAM. A bright-field optical illumination, with a much tighter focus than the acoustic focus, is adopted to achieve optical resolution [124]. A tunable dye laser (CBR-D, Sirah) pumped by a Nd:YLF laser (INNOSAB, Edgewave) is used as the excitation source. The pulses from the dye laser are focused by a microscope objective (4x, NA = 0.1; Olympus America, Center Valley, PA) into the sample. The generated photoacoustic signals are detected by a focused ultrasonic transducer (central frequency: 50 MHz; V214-BC-RM, Olympus NDT), which is placed confocally with the objective. An ultrasound/light splitter, composed of a thin layer of silicone oil sandwiched between a right-angle prism and a rhomboid prism, is used for the co-axial alignment of the optical and acoustic beams. A plano-convex lens attached to the top of the splitter corrects the refraction of the prisms. The optical focal spot size was about 5  $\mu\text{m}$ , much smaller in diameter than the acoustic focus, so the lateral resolution

was predominantly determined by the optical focal spot size, the so-called optical resolution. The OR-PAM has a lateral resolution of approximately 5  $\mu\text{m}$ , an axial resolution of approximately 15  $\mu\text{m}$ , and a penetration depth of up to 1.2 mm in soft tissues [124].

The SW-PAM utilized an Nd:YVO<sub>4</sub> laser (NT242-SH, Ekspla, Vilnius, Lithuania) as the irradiation source. The laser generates 532-nm pulses with 1.5-ns duration, which are transmitted to the optical objective through a single-mode optical fiber. The objective lens has an NA of 0.60, providing a lateral resolution of approximately 0.4  $\mu\text{m}$  [125]. The samples irradiated by focused laser pulses generate photoacoustic waves, which are detected in transmission mode by a custom-made ultrasonic transducer with a central frequency of 40 MHz and an NA of 0.5. The photoacoustic signals were then amplified, digitized at a sampling rate of 1 GHz, and processed by a computer for image processing.

The OR-PAM-FCM system uses a tunable dye laser (CBR-D, Sirah) pumped by a Nd:YLF laser (INNOSAB, Edgewave) as the irradiation source. The laser beam is focused into the sample by an objective lens (13.3X, NA = 0.2; Olympus America). The generated photoacoustic waves are detected using an ultrasonic transducer (central frequency: 75 MHz; V2022 BC, Olympus NDT). The OR-PAM subsystem can achieve a lateral resolution of approximately 3.9  $\mu\text{m}$ , an axial resolution of approximately 17  $\mu\text{m}$ , and a penetration depth of up to 1.2 mm in soft tissues [126]. The FCM subsystem shares the same laser source and objective lens. A dichroic mirror (DMLP605, Thorlabs, Newton, NJ) and an emission filter (FF01-624/40-25, Semrock, Rochester, NY) allow the transmission of fluorescence (above 605 nm) emitted from the sample. The fluorescence light passing through the pinhole (pinhole diameter: 50  $\mu\text{m}$ ) is collected by a photomultiplier (H6780-20, Hamamatsu, Bridgewater, NJ). The photoacoustic signals and fluorescence signals are acquired through a data acquisition card (CS 14200, Gage Applied, Lockport, IL). The FCM subsystem has a lateral resolution of approximately 3.9

$\mu\text{m}$ , an axial resolution of approximately  $38 \mu\text{m}$ , and a penetration depth of approximately  $1 \text{ mm}$  in soft tissues [126].

For the OR-PAM-OCT dual modality system, the OR-PAM subsystem is irradiated by a diode-pumped Nd:YVO<sub>4</sub> laser (pulse width:  $1.2 \text{ ns}$ ; repetition rate:  $20 \text{ kHz}$ ; wavelength:  $532 \text{ nm}$ ; Elforlight SPOT, Northants, UK) and the photoacoustic signals are detected using a focused ultrasonic transducer (central frequency:  $75 \text{ MHz}$ ; V2022, Olympus NDT). The OR-PAM subsystem can achieve a lateral resolution of approximately  $5 \mu\text{m}$ , an axial resolution of approximately  $14 \mu\text{m}$ , and a penetration depth of approximately  $1 \text{ mm}$  in soft tissues [127]. The OCT subsystem measures the depth-resolved backscattered light from the object. It is configured as a fiber-based Michelson interferometer, and is seeded by a broadband superluminescent diode (D890, Superlum, Carrigtwohill, Ireland). The OCT subsystem has a lateral resolution of approximately  $5 \mu\text{m}$  and an axial resolution of approximately  $5.9 \mu\text{m}$  in soft tissues. The axial imaging range of OCT was approximately  $2 \text{ mm}$  in soft tissues [127].

### **4.3. Photoacoustic Microscopy of Melanoma Cells**

Melanoma cells are a type of skin cancer cells that contain melanin, a natural dark pigment [129]. Therefore, unlike most other types of cells, melanoma cells are black in color when viewed under a bright-field optical microscope (Figure 4.3A). Due to the strong optical absorption of melanin in the visible light region, melanoma cells could be conveniently imaged using PAM. In a high-resolution PAM image (Figure 4.3B), individual intracellular compartments termed melanosomes containing the melanin pigment can be clearly observed. Figure 4.3C shows a transmission bright-field optical micrograph of melanoma cells grown inside a PLGA inverse opal scaffold. Despite its capability to resolve the distribution of the cells, it was difficult to derive 3D information from the image.

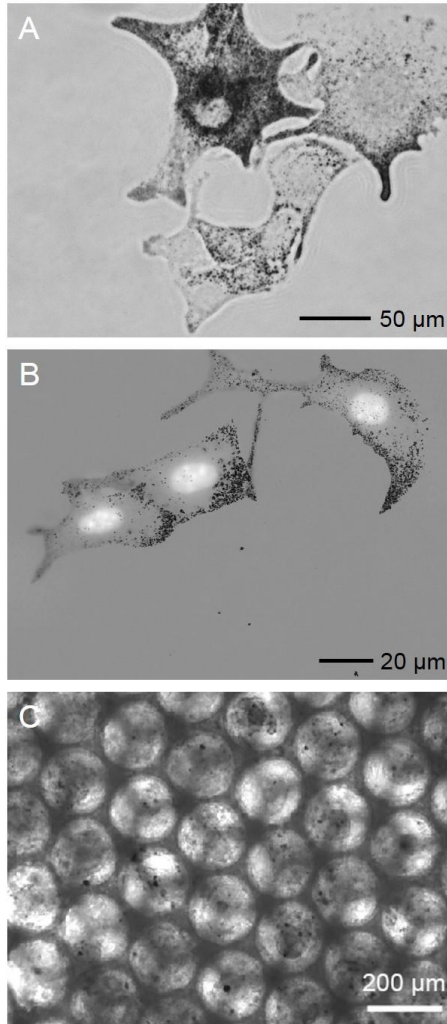


**Figure 4.3.** A) Transmission bright-field micrograph showing several melanoma cells grown on a cover glass. B) High-resolution PAM image of melanoma cells superimposed with fluorescence micrograph of cell nuclei. C) Transmission bright-field micrograph showing melanoma cells grown in a PLGA inverse opal scaffold with a uniform pore size of 200  $\mu\text{m}$ . The melanoma cells are shown as dark dots in the void space.

Figure 4.4 shows the feasibility of non-invasive 3D imaging by AR-PAM [130]. The PAM coronal and sagittal MAP images in Figure 4.4A clearly show the distribution of melanoma cells in a scaffold, with the capability to penetrate the entire cell/scaffold construct with a thickness of about 1.2 mm. Figure 4.4B shows a 3D depiction of the melanoma cells in the scaffold. Individual cells or cell clusters could be identified (black

dots or patches) in both the 2D and 3D images. This penetration depth is rather deep as compared to the conventional microscopy techniques. According to my experience, for a similar inverse opal scaffold seeded with melanoma cells, confocal microscopy and two-photon microscopy could only reach a depth of about 0.1–0.2 mm and about 0.2–0.3 mm, respectively. Importantly, the AR-PAM system could still provide acceptable lateral resolution of approximately 45  $\mu\text{m}$  at such a deep penetration depth. These results clearly demonstrated the advantage of AR-PAM in penetration for characterizing cells in 3D scaffolds. In comparison, a cell-free PLGA inverse opal scaffold was also imaged by AR-PAM. As expected, no obvious signals were observed because the optical absorption of the scaffold at the given wavelength (570 nm) was low. Hence, it was confirmed that the photoacoustic signals came from the melanoma cells rather than the scaffold.

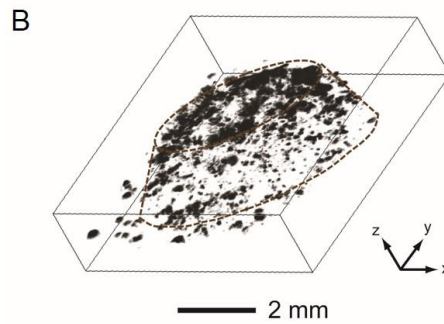
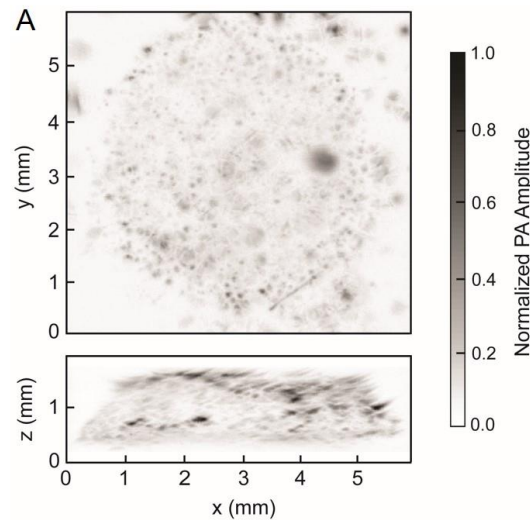


**Figure 4.4.** A) PAM coronal and sagittal MAP images showing the distribution of melanoma cells in a PLGA inverse opal scaffold. B) A 3D reconstruction view of the cells in the scaffold. The dotted lines indicate the boundary of the scaffold.

To more accurately assess the cell distribution at a certain depth in the examined volume (420–780  $\mu\text{m}$  planes), a series of sections were mapped with a layer thickness of 60  $\mu\text{m}$  at day 14 (Figure 4.5). Uniform cell distribution was observed across all layers, even in the central plane of the scaffold. The results clearly showed that, AR-PAM could resolve spatial distribution of cells inside a thick scaffold, and readily distinguish different patterns in cell distribution. In principle, as a critical feature of the imaging modality, sections at any depth of the volume can be reconstructed. Using AR-PAM, an engineered scaffold/tissue construct can be conveniently examined in a non-invasive manner to determine if defect regions are present inside the construct (as well as the exact number and locations of defect sites) before the construct is used for implantation.

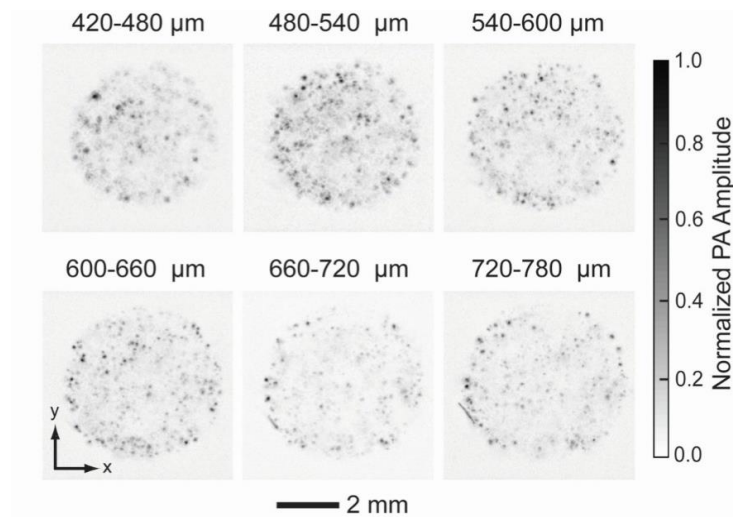


**Figure 4.5.** PAM coronal MAP images of melanoma cells in a PLGA inverse opal scaffold cultured for 14 days. The images were taken from different layers parallel to the top surface without physically slicing the scaffold. The first layer started at 420  $\mu\text{m}$  beneath the surface, and the layer spacing was 60  $\mu\text{m}$ .

In addition to qualitative imaging, it has been so far rarely reported to temporally monitor and quantify cell proliferation in a 3D scaffold with relatively high spatial resolution. AR-PAM is a well-suited tool for accomplishing this task due to its deep penetration depth and non-invasiveness. In a typical study, melanoma cells were seeded into PLGA inverse opal scaffolds with a thickness of about 1.5 mm using a spinner flask. At days 1, 3, 7, and 14 post-seeding, the scaffolds with cells were carefully taken out from the media, immobilized on a polydimethylsiloxane (PDMS) block, and immersed in warm PBS at 37 °C supplemented with 1 vol.% antibiotics for PAM imaging. Pure PDMS block was found not to generate photoacoustic signals, indicating no contribution to the photoacoustic signals from the PDMS block.

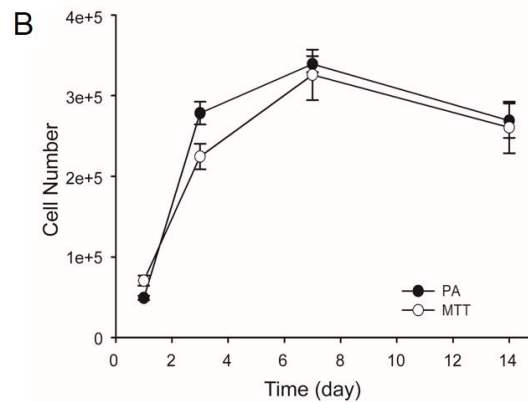
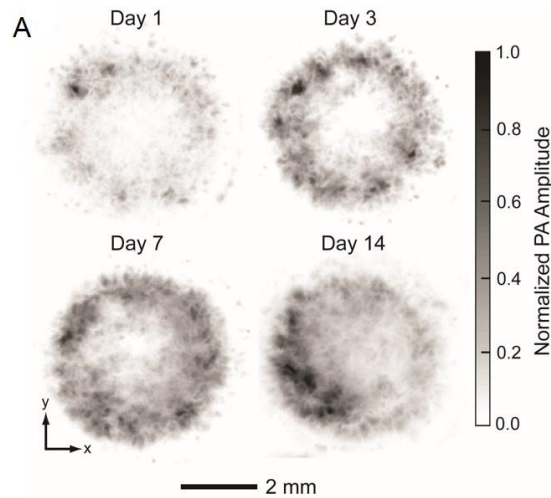


**Figure 4.6.** A) Representative time-course PAM images (coronal MAP of the entire volume) of melanoma cells in a PLGA inverse opal scaffold at 1, 3, 7 and 14 days post-seeding. B) Quantitative analysis of the proliferation of melanoma cells in the scaffolds derived from both the PAM volumetric data ( $n = 4$ ) and the MTT assay ( $n = 3$ ). The data are presented as mean  $\pm$  standard error.

Time-course PAM coronal MAP images clearly show the growth of melanoma cells inside an individual scaffold (Figure 4.6A). Quantification of the cell numbers was calculated using the collected PAM volumetric data. To elucidate the relationship between the photoacoustic signal amplitude and the number of melanoma cells in the scaffold, inverse opal scaffolds with different numbers of cells were scanned with PAM under identical conditions. The cells in the scaffolds were then completely released from the scaffolds with Accumax<sup>TM</sup> and manually counted using a hemocytometer. The signal amplitude from the photoacoustic volumetric data was found to be linearly correlated with the number of cells in the scaffold.

The cell numbers calculated from the PAM volumetric data were plotted against different time points (Figure 4.6B). It was observed that the number of cells increased with time during the first 7 days, and then started to decrease for the next 2 weeks. Based on the calibration curve, the average cell numbers at days 1, 3, 7, and 14 were calculated to be approximately  $4.9 \times 10^4$ ,  $2.8 \times 10^5$ ,  $3.4 \times 10^5$ , and  $2.7 \times 10^5$  per scaffold, respectively. A parallel MTT assay was also conducted. Interestingly, the average numbers of cells in the scaffolds for the MTT group at days 1, 3, 7, and 14 were calculated to be  $7.1 \times 10^4$ ,  $2.2 \times 10^5$ ,  $3.3 \times 10^5$ , and  $2.6 \times 10^5$ , respectively, which were very similar to those in the PAM group.

In summary, PAM clearly exhibits advantages over other currently available techniques. PAM scan rate is fast compared to many other imaging modalities. For a scaffold with the same dimensions, it takes about 20 min for a confocal microscope to

scan through in order to get a volumetric data of approximately 200  $\mu\text{m}$  in depth. Due to the complexity in the scanning mechanisms and reconstruction algorithms, micro-CT and MRI require even longer times. By contrast, PAM only takes about 6 min. This fast scanning rate for PAM gives it the unique ability to characterize live cells in thick, 3D scaffolds, and therefore, chronologic monitoring of individual scaffolds is possible.

#### **4.4. Photoacoustic Microscopy of Cells Containing No Pigments *in vitro***

##### **4.4.1. Photoacoustic Microscopy of Cells Stained by MTT Formazan**

Although melanoma cells can be used as a model cell line in the proof-of-concept demonstration, they do not represent the majority of cells that are commonly used in tissue engineering and regenerative medicine. Unlike melanoma cells, most other cell types contain no intrinsic pigments with strong optical absorption and thus cannot be readily detected by PAM. Cells engineered with fluorescent proteins may give photoacoustic signals [131, 132], but the signal intensities are usually low due to their small extinction coefficients ( $<50,000 \text{ M}^{-1}\text{cm}^{-1}$ ). Li *et al.* recently demonstrated *in vivo* PAM imaging of cells that were transfected with lacZ gene and then stained with 5-bromo-4-chloro-3-indolyl-beta-D-galactopyranoside (X-gal) [133, 134]. Krumholz *et al.* further demonstrated PAM imaging of cells that were transfected with tyrosinase, an enzyme that can produce the pigment melanin [135]. Gold-based nanoparticles have also been shown to give strong photoacoustic signals that can be used to label cells for PAM imaging [136, 137]. In addition to these methods, I have introduced a contrast agent based on MTT formazan for simple, stable and nontoxic staining of various types of cells, allowing high-resolution and volumetric PAM imaging [138].

The key component of this approach is MTT, a tetrazole that can be metabolized and reduced to MTT formazan in living cells (Figure 4.7A) [139-142]. The MTT assay

has long been used to biochemically evaluate cell viability, metabolic activity, and proliferation profile. The concentration of MTT formazan is determined by extracting it from cells with an organic solvent and then measuring the optical density using a spectrophotometer. In general, the optical density is linearly proportional to the number of metabolically active cells. The MTT formazan is insoluble in water but soluble in a number of organic solvents. The MTT formazan solution in 1-propanol has a purple color (Figure 4.7B, bottom), with a broad, strong absorption in the spectral region of 500–620 nm, and a peak around 560 nm (Figure 4.7C, purple line). There is also a linear relationship between the absorbance and the concentration of MTT formazan in 1-propanol. In contrast, the MTT solution in PBS shows a yellowish color (Figure 4.7B, top) with absorption only below 450 nm (Figure 4.7C, green line).

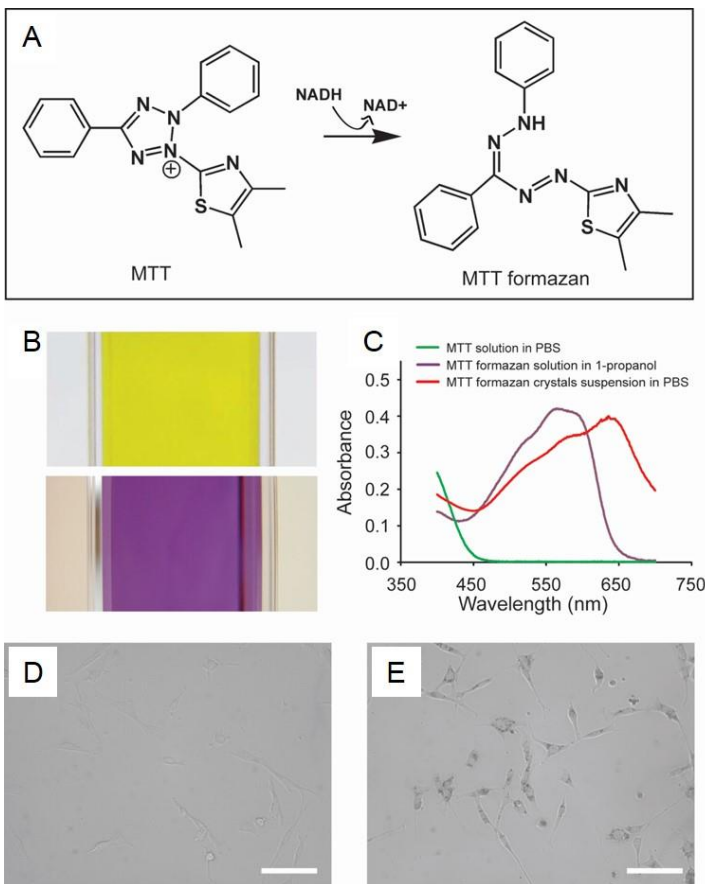


**Figure 4.7.** A) A schematic showing the conversion of MTT to MTT formazan in live cells. B) Photographs showing MTT solution in PBS (top panel) and MTT formazan solution in 1-propanol (bottom panel). C) UV-vis absorption spectra of MTT solution in PBS, MTT formazan solution in 1-propanol, and MTT formazan crystal suspension in PBS. D, E) Transmission bright-field optical micrographs showing fibroblasts grown on cover glasses (D) without and (E) with MTT formazan staining for 3 h.

Since MTT formazan crystals also show a purple color, it is not unreasonable to assume that their absorption spectra are similar to what is observed for their solution in 1-propanol. Indeed, the suspension of the crystals in PBS showed strong absorption in the spectral region of 500–700 nm, with a peak around 650 nm (Figure 4.7C, red line). This red shift in absorption band relative to the band of individual molecules in 1-propanol is probably due to the coupling of molecular transition dipoles [143]. As a result, the MTT formazan crystals generated inside living cells can be directly used to greatly enhance the contrast for conventional optical microscopy. Except for a few types of cells (*e.g.*, melanoma cells and erythrocytes), most other cells (*e.g.*, fibroblasts) show very little contrast under a bright-field optical microscope and can barely be observed (Figure 4.7D). However, after 3 h incubation with MTT in a regular culture medium, the cells could be easily resolved with sharp contrast because the metabolite MTT formazan strongly absorbs visible light and provides good contrast for bright-field imaging (Figure 4.7E). In this case, the MTT formazan is more or less equivalent to the natural pigments in melanoma cells or erythrocytes, suggesting its potential use as a contrast agent for PAM.

I first demonstrated the suitability of MTT formazan as a contrast agent for PAM of cells cultured on 2D substrates. In a typical experiment, fibroblasts were incubated with MTT in the culture medium for 3 h under normal conditions (37 °C and 5% CO<sub>2</sub>). Afterwards, the cells were briefly fixed and fluorescently stained for f-actin and imaged

using an OR-PAM-FCM that can measure both fluorescence contrasts and optical absorption [126]. The confocal and PAM images (Figure 4.8, A–C) indicate that nearly all the cells stained with MTT formazan could be detected by PAM. The undetected cells are presumably due to the fact that they were dead prior to MTT treatment, thus preventing conversion of MTT to MTT formazan. In contrast, the unstained cells were not detectable by PAM (Figure 4.8, D–F).

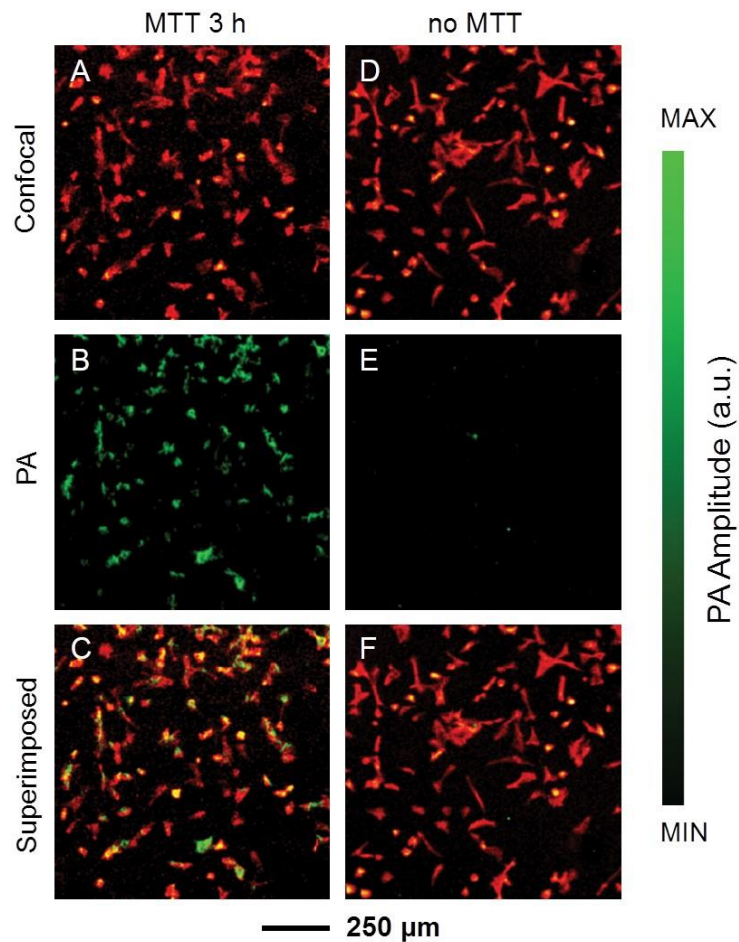


**Figure 4.8.** A–C) Confocal and PAM MAP images showing NIH/3T3 fibroblasts grown on a cover glass and stained with MTT for 3 h. D–F) Confocal and PAM MAP images showing NIH/3T3 fibroblasts grown on a cover glass without staining. In both cases the f-actin of the cells were stained in red for fluorescence observation.

The intensity of the collected photoacoustic signals is dependent on both the concentration of MTT and the incubation time because these two parameters determine the amount of MTT formazan generated inside each cell. To quantify these correlations, 40  $\mu\text{L}$  of 5 mg/mL or 10 mg/mL MTT solution was added to the culture medium in each well containing  $5 \times 10^4$  fibroblasts and incubated for 15, 60 and 120 min. The PAM images (Figure 4.9A) indicate that, at 15 min of incubation, both concentrations gave signals of similar low intensity, presumably due to the limited uptake and/or metabolic conversion of MTT by the cells within the short period of time. As the incubation time was prolonged, the signal intensity increased; similarly, the signal intensity was stronger at a higher concentration of MTT under the same incubation time.

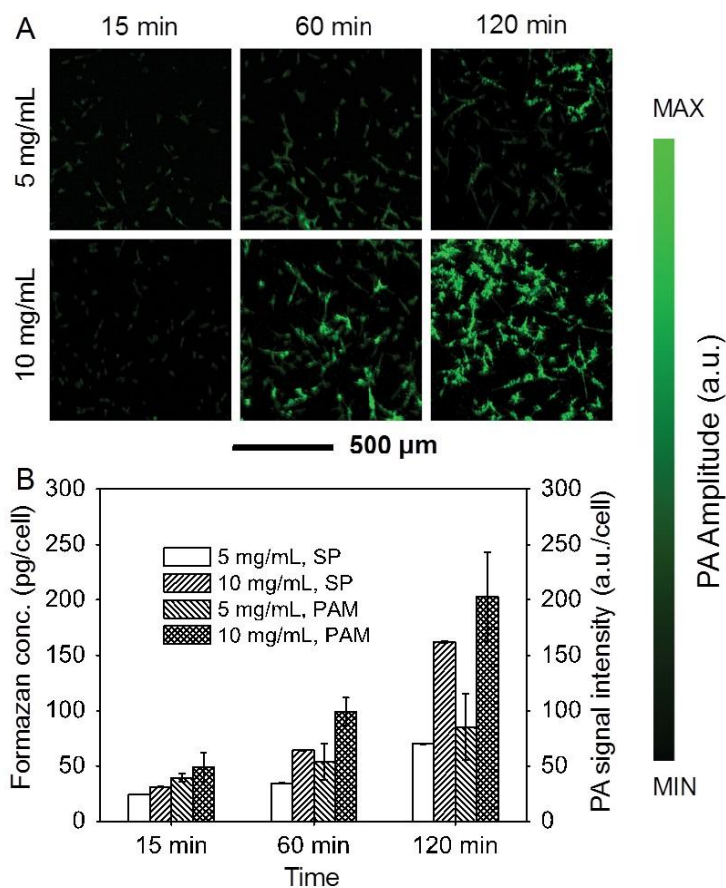


**Figure 4.9.** A) PAM MAP images showing fibroblasts cultured on cover glasses in the presence of MTT at the indicated concentration and duration of time. B) The amount of MTT formazan and

*photoacoustic signal intensity per cell as a function of MTT concentration and incubation time. Data were presented as means  $\pm$  standard deviation.*

Immediately after each PAM scan, the formazan crystals from the cells were extracted by dissolution with 1-propanol and then quantified using a spectrophotometer. The amount of MTT formazan per cell was calculated based on the calibration curve and the number of cells in each well. As shown in Figure 4.9B, the calculated amount of MTT formazan per cell correlated well with the PAM image. The amount of formazan per cell for 10 mg/mL MTT was approximately twice of that for 5 mg/mL with incubation times up to 120 min except for the initial time point (15 min), where the two samples only showed a minor difference. At a fixed concentration of 5 mg/mL or 10 mg/mL, the amount of formazan per cell increased with incubation time. We also calculated the PA signal intensity per cell from the PA image. Interestingly, the PA signal intensity per cell showed a trend similar to what was observed in the spectroscopic measurements (Figure 4.9B). Cell viability was also evaluated by using LIVE/DEAD staining post MTT addition, and it was found that >99% of the cells were alive in all cases, similar to the control group without MTT treatment, indicating the negligible toxicity of the staining method.

I further explored the use of this staining method for 3D cellular imaging, which is highly sought-after in tissue engineering. Fibroblasts were seeded into PLGA inverse opal scaffolds with a uniform pore size of 200  $\mu$ m. At day 5, the cell/scaffold constructs were incubated with MTT for 3 h, briefly rinsed with PBS, and immediately scanned with an AR-PAM. MAP images from the top and the side revealed the spatial distribution of cells in the 3D space of the scaffold with a penetration depth of over 1.2 mm (Figure 4.10A, black dots). More importantly, it was able to render 3D cell distribution from the volumetric PAM data (Figure 4.10B). To evaluate the ability of MTT to stain cells in a dense matrix rather than the highly porous scaffolds, a PLGA inverse opal scaffold was

filled with a cell suspension in 1 wt.% alginate saline solution, followed by cross-linking with a 1 wt.%  $\text{CaCl}_2$  saline solution for 5 min. The cell-hydrogel-laden inverse opal scaffold was kept in culture for 5 days and then subjected to MTT staining for 4 h. An incubation time of 4 h was chosen so that enough MTT would diffuse into the entire matrix, be uptaken and metabolized by the cells to generate MTT formazan. Again, AR-PAM images clearly show identifiable cells throughout the scaffold (Figure 4.10C). Immediately after PAM imaging, an optical micrograph was taken using a microscope in the reflection mode (Figure 4.10D). Comparing with the PAM projection image from the top, well-matched features on the surface of the scaffold were observed as indicated by arrowheads (Figure 4.10, C and D), indicating good accuracy of PAM when combined with the staining.

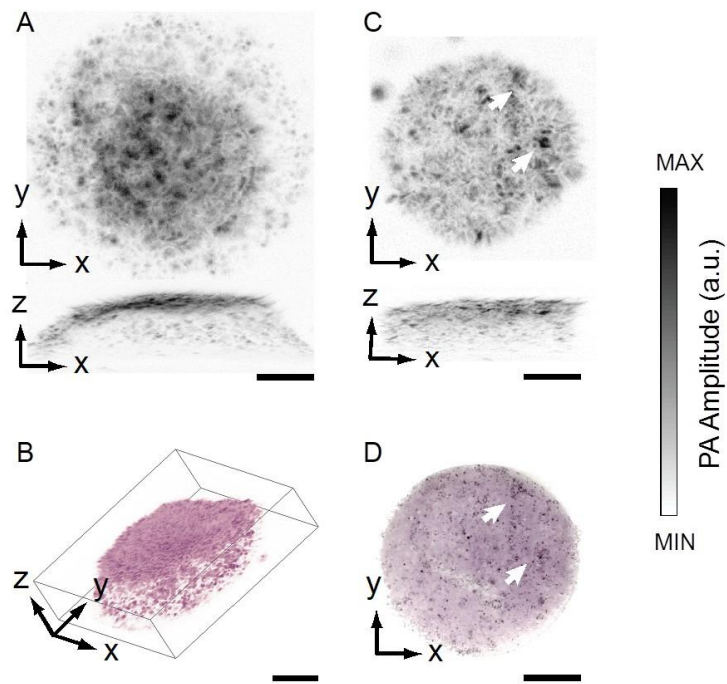


**Figure 4.10.** A) PAM coronal and sagittal MAP images showing fibroblasts cultured in a PLGA inverse opal scaffold, followed by MTT staining for 3 h. B) 3D rendering of the volumetric PAM data in (A). C) PAM coronal and sagittal MAP images of fibroblasts cultured in a PLGA inverse opal scaffold filled with cross-linked alginate hydrogel, followed by incubation with MTT for 4 h.

D) A reflective optical micrograph showing the same scaffold as in (C). The arrows indicate the matching features in PAM and optical microscopy. Scale bars: 1 mm.

I then conducted chronologic PAM of scaffolds containing the cells, in an attempt to quantify the cell proliferation profile. At 6 h, 3 days and 7 days post seeding of fibroblasts, the scaffolds were incubated with MTT for 3 h and then imaged with AR-PAM. Representative MAP images from the middle layer (600–660  $\mu\text{m}$  from the top surface) of the scaffolds at each time point showed the progressive cell proliferation as indicated by the increase in area for the dark dots (Figure 4.11A). The presence of dark dots with large areas in the center of the scaffold could be attributed to the high cell densities. Quantification could be obtained from the volumetric data of PAM scans. Summations of PA signal amplitudes, which correspond to total cell numbers, measured at day 3 and day 7 were normalized to what was obtained at 6 h (Figure 4.11B). The curve clearly shows how the cells proliferated with time.

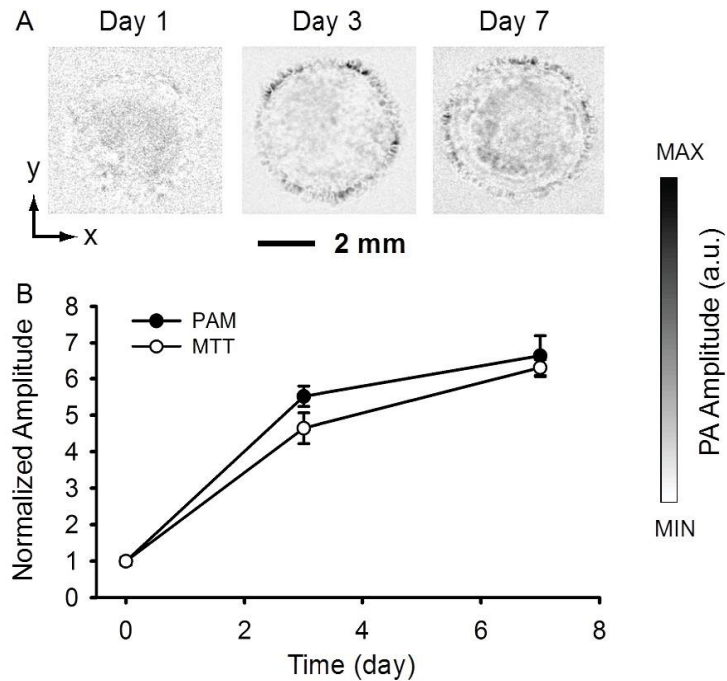


**Figure 4.11.** A) Representative PAM chronological coronal images showing fibroblasts grown in PLGA inverse opal scaffolds (MAPs in the 600–660  $\mu\text{m}$  layers from the top surface) at 6 h, 3 days and 7 days. B) Quantification of normalized cell numbers in the scaffolds as determined by volumetric PAM data ( $n = 3$ ) and parallel MTT biochemical assays ( $n = 3$ ). Data are presented as mean  $\pm$  standard deviation.

The proliferation profile obtained from PAM correlated well with what was derived from a traditional quantitative MTT cell viability assay. In this case, immediately post PAM imaging, the formazan crystals were extracted by dissolution with 1-propanol and quantified using a spectrophotometer. The normalized cell proliferation profiles obtained using these two different methods look very similar (Figure 4.11B).

In addition, a cell invasion experiment was conducted to further expand the scope of application for the staining method in PAM, which essentially functions as virtual biopsy. In this case, I fabricated PLGA inverse opal scaffolds with two different pore sizes of 200 and 300  $\mu\text{m}$ , respectively. After forming monolayers of fibroblasts in a 24-well plate, the scaffolds were carefully placed on top of the cells (one scaffold per well) and the cells were allowed to invade from the surface into the bulk of the scaffolds. The cells were cultured for 1, 3 and 7 days, stained with MTT formazan, and imaged with an OR-PAM-OCT (only the PAM subsystem was used in this case). As shown by the PAM sagittal MAP images (Figure 4.12A), the cells had invaded from the seeding side (bottom of the image) into the scaffolds to approximately half of the entire thickness in the case of scaffolds with 300- $\mu\text{m}$  pores. The cell invasion depth can be quantified using the volumetric PAM data. The maximum invasion depth was calculated from all the 800 PAM scan slices for each scaffold (Figure 4.12B). Scaffolds with small pores (200  $\mu\text{m}$ ) showed a slightly faster cell invasion rate than scaffolds with large pores (300  $\mu\text{m}$ ) at day one.

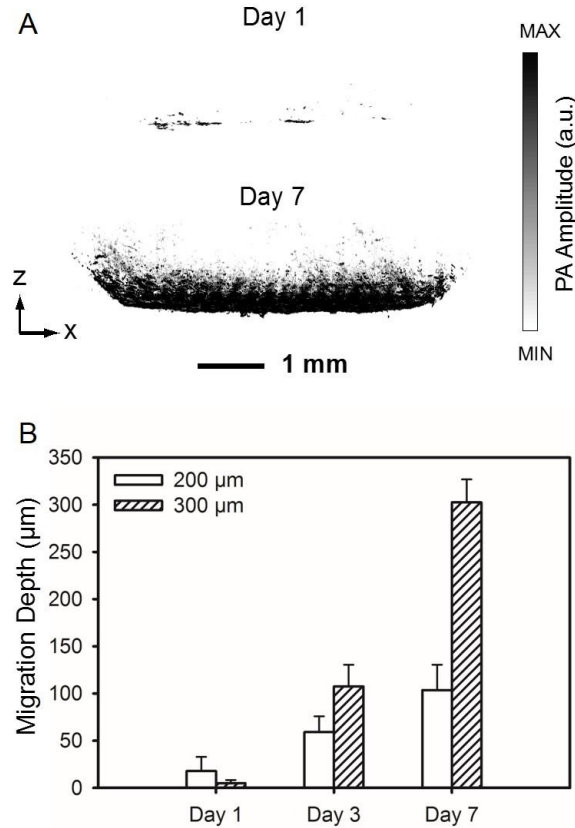


**Figure 4.12.** A) PAM sagittal MAP images showing cell invasion profiles at days 1 and 7 into PLGA inverse opal scaffolds with a pore size of 300  $\mu\text{m}$ . B) Average cell penetration depths in scaffolds with pore sizes of 200 and 300  $\mu\text{m}$ , respectively, as determined by PAM virtual biopsy. Data are presented as means  $\pm$  standard deviations ( $n = 3$ ).

Such observation could be explained by the fact that, for scaffolds with smaller pores, the surface areas and thus the contact regions between the scaffolds and the cell monolayers were larger, facilitating the cell migration in the initial stage. However, as more cells migrated into the scaffolds and started to proliferate, if the windows connecting the pores were not big enough (as in the case of scaffolds with 200- $\mu\text{m}$  pores, where the windows size was 40–50  $\mu\text{m}$ ), they might be blocked by the cells, so that further cell invasion was impeded. As expected, scaffolds with 300- $\mu\text{m}$  pores showed deeper invasion at later time points, as they provided bigger windows (70–80  $\mu\text{m}$ ) to interconnect adjacent pores for cell migration. Such result is similar to that obtained by

using the conventional technique based on invasive sectioning and fluorescence microscopy [53].

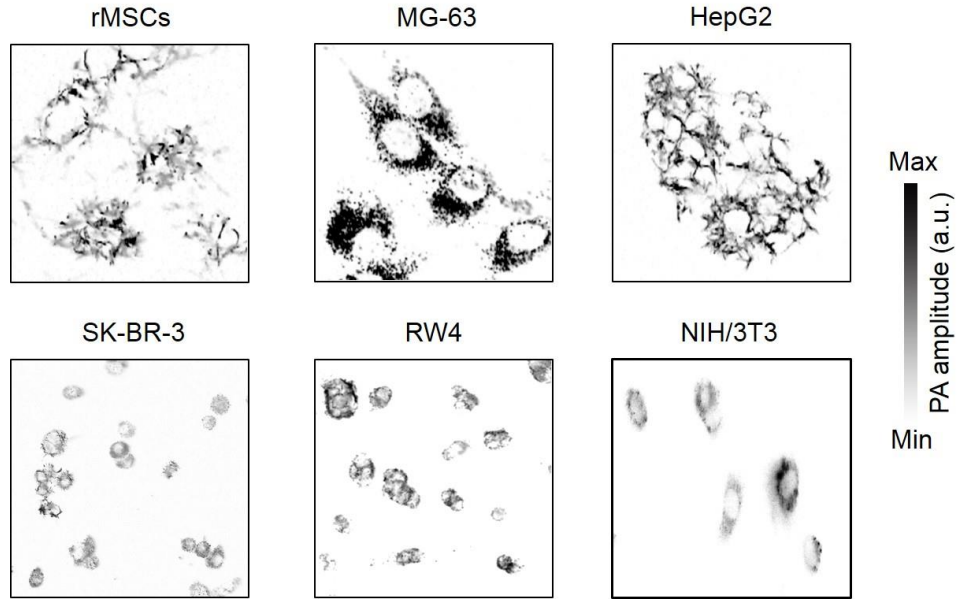


**Figure 4.13.** High-resolution PAM coronal MAP images showing rat bone marrow stromal cells (rMSCs), MG-63 human osteoblasts, HepG2 human hepatoma cells, SK-BR-3 human breast cancer cells, RW4 mouse ESCs, and NIH/3T3 mouse embryonic fibroblasts, after the cells had been stained with MTT.

The staining could also enable high-resolution (0.4  $\mu\text{m}$ ) PAM imaging. Rat bone marrow stromal cells, MG63 human osteoblasts, HepG2 human hepatoma cells, SK-BR-3 breast cancer cells, RW4 mouse ESCs and NIH/3T3 mouse embryonic fibroblasts were cultured on cover glasses, fixed and then stained with MTT formazan. All these cells with whole-cell morphology could be efficiently imaged by PAM (Figure 4.13).

It should be noted that, for the present system, MTT formazan crystals have a strong absorption in the region of 500–700 nm. By using other tetrazolium-formazan systems [139, 141], however, the absorption peak position can be finely tuned to enable

PAM imaging at other wavelengths for various biological and biomedical applications as well as possible multi-wavelength scanning.

#### 4.4.2. Photoacoustic Microscopy of Cells Stained via Cytochemistry

There is another category of convenient staining methods, the chromogenic (immuno)cytochemistry. It is typically conducted by sectioning thick samples into thin slices, staining these slices with dyes and followed by examination under a microscope. Although cytochemistry has been used as a pivotal tool for biology and medicine for over a century, its capability is limited by the nature of 2D imaging of the conventional microscopy. Realizing that the rich absorption contrasts are present in a biological sample after histological staining, I have therefore extended its application to volumetric PAM imaging of the cells in thick scaffolds without the need of physical sectioning [144].

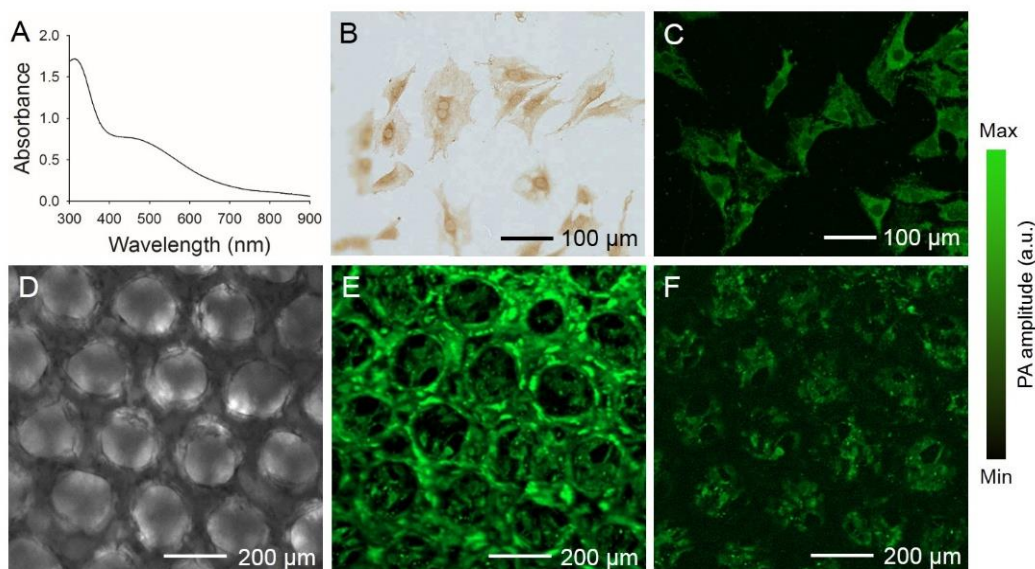


**Figure 4.14.** A) UV-vis absorption spectrum of the reaction product of ImmPACT DAB and HRP. B) Transmission bright field optical micrograph of MC3T3 cells stained for f-actin with biotin-phalloidin, streptavidin-HRP and DAB. C) High-resolution OR-PAM coronal MAP image of MC3T3 cells stained for f-actin with the same procedure as in (B). D) Transmission bright-field optical micrograph showing the cells cultured in a PLGA inverse opal scaffold for 3 days and

*stained with biotin-phalloidin/HRP-streptavidin/DAB. E) OR-PAM coronal MAP image (0–200  $\mu\text{m}$  beneath the top surface) of the same cell/scaffold construct in (D). F) OR-PAM coronal MAP image showing the bottom section (100–200  $\mu\text{m}$  beneath the top surface) of the pores on the surface of the scaffold.*

Figure 4.14A shows the UV-vis absorption spectrum of the reaction product of horseradish peroxidase (HRP) and ImmPACT diaminobenzidine (DAB) peroxidase substrate, which had a strong absorption peak at 320 nm, followed by a broad peak from 400 nm to 700 nm. Figure 4.14B shows a representative transmission bright field optical micrograph of MC3T3 preosteoblasts whose f-actin was stained with biotin-phalloidin/streptavidin-HRP, followed by color development with DAB. Figure 4.14C shows a high-resolution (0.4  $\mu\text{m}$ ) SW-PAM coronal MAP image of a different area of the same sample obtained at the wavelength of 570 nm, clearly revealing the stained cytoskeleton and the unstained nuclei. This result demonstrates the capability of PAM to resolve a specific cell component after immunostaining.

I then seeded MC3T3 preosteoblasts into a 3D PLGA inverse opal scaffold with a uniform pore size of 200  $\mu\text{m}$ . Figure 4.14D shows a representative transmission bright-field optical micrograph of cells cultured in the scaffold for 3 days and then stained for f-actin with biotin-phalloidin/streptavidin-HRP/DAB. The cells typically stretched along the walls of the pores. As shown in the OR-PAM coronal MAP image (Figure 4.14E), the same pattern of cell attachment was observed. It is noticed that those cells close to the bottom of the pores on the surface (*i.e.*, 100–200  $\mu\text{m}$  beneath the top surface) also showed up in the MAP image (Figure 4.14E), and the signals from these cells could be easily separated from the rest of the sample (Figure 4.14F) based on the depth information. In comparison, it was very difficult to image the cells at depth using a transmission bright field optical microscope (Figure 4.14D), unless the scaffold is physically sectioned prior to imaging. OR-PAM can reach a penetration depth of 200–

300  $\mu\text{m}$  with these scaffold-based samples, which is more than twice that of confocal microscopy at similar lateral resolutions. The penetration depth can be doubled by illuminating a sample from both the top and bottom [145]. By using AR-PAM, the penetration depth can be further extended [37, 130, 138]. Moreover, OR-PAM relies on optical absorption, and non-absorbing biomaterials do not generate photoacoustic signals; therefore, photoacoustic imaging is essentially background-free. On the contrary, the use of fluorescence microscopy can sometimes be influenced by the autofluorescence from certain biomaterials, especially the biologically derived polymers such as collagen [146].

#### **4.5. Photoacoustic Microscopy of Neovascularization *in vivo***

Despite many years of research, it remains a grand challenge to non-invasively monitor and assess the development of neovasculature *in vivo* with high spatial resolution, deep penetration, and high contrast [147]. In assessing neovascularization in implanted scaffolds, the most widely used imaging modalities include micro-CT and laser scanning microscopy (LSM, *e.g.*, confocal and multi-photon microscopy) [148, 149]. While micro-CT can penetrate a tissue/scaffold construct up to several centimeters thick, it suffers from poor contrast for soft tissues and fluid-perfused scaffolds unless exogenous contrast agents are administered, as well as ionizing irradiation. LSM has limited tissue penetration (up to several hundred micrometers deep only) especially in the presence of strong light scattering by blood, and they usually require the use of a fluorescent chromophore as the probe as well. PAM on the other hand, is well-suited for this job. Hemoglobin, the primary carrier of oxygen in blood, exhibits a strong intrinsic optical absorption contrast for label-free PAM with high sensitivity [38, 39]. This unique feature allows one to map the vascular network and avoid possible alternations to the hemodynamics caused by exogenous angiographic agents. In this section, I will demonstrate the capability of PAM in non-invasive imaging and monitoring of the

neovascularization process in PLGA inverse opal scaffolds *in vivo* for individual mice up to 6 weeks post implantation [150]. When combined with OCT, which is based on optical scattering contrast from the scaffold, the neovasculature developed inside the pores of the scaffolds as a function of time could be easily resolved and compared. In addition, I also evaluated the effect of pore size on neovascularization by quantifying the PAM volumetric data.

#### 4.5.1. OR-PAM-OCT of Neovascularization and Scaffolds

PLGA inverse opal scaffolds (with a uniform pore size of 200  $\mu\text{m}$ ) of about  $3 \times 3 \times 1.5 \text{ mm}^3$  in dimensions were implanted subcutaneously in the ears of nude mice (one scaffold per ear per mouse, Figure 4.15), and monitored using the dual-modality OR-PAM-OCT system up to 6 weeks post implantation.

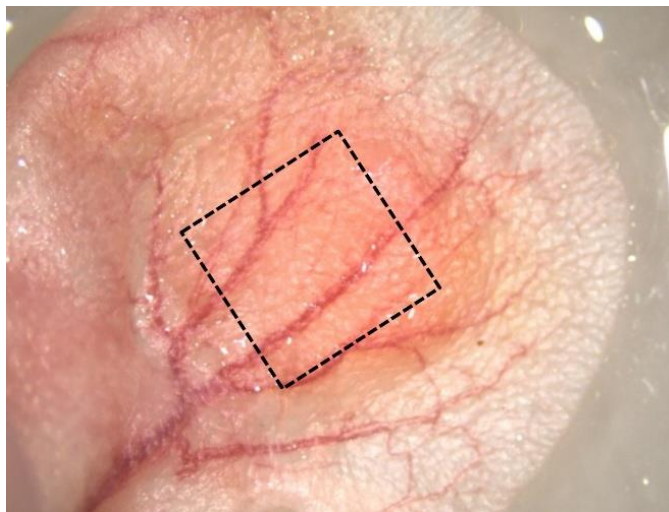


**Figure 4.15.** A photograph showing the mouse ear model used for *in vivo* neovascularization studies using PLGA inverse opal scaffolds. The dotted square indicates the approximate region where the scaffold resided.

In this study, the PLGA polymer itself could not generate sufficiently strong photoacoustic signals to provide adequate contrast, and thus only vasculature was imaged

by PAM due to the strong optical absorption of hemoglobin. As shown by the coronal MAP images in Figure 4.16, A–C, the density of blood vessels increased with time over the 6-week period. Microvasculature down to the capillary level was well-resolved due to the high lateral resolution of OR-PAM. OCT signals were also collected simultaneously with PAM scanning, which were used to resolve the structure of the scaffold/tissue construct. The OCT signals from the top layer of the ear skin (around 150  $\mu\text{m}$  in thickness) were removed from the 3D data [151]. As shown by the coronal MAP images in Figure 4.16, D–F, while the overall structure of the scaffold was largely retained by week 6, some regions had started to degrade over the period, leading to a slight local increase in the size of a few pores (examples are indicated by arrowheads).

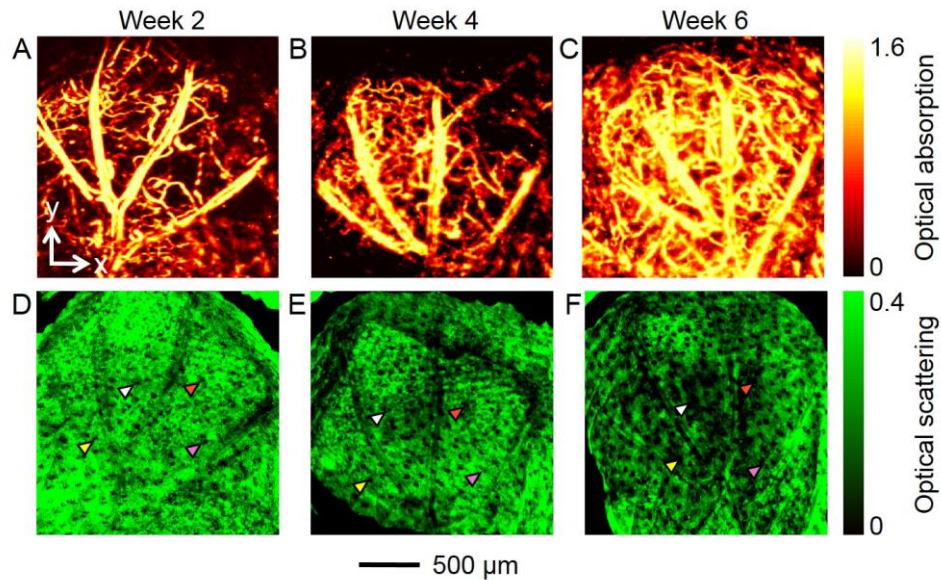


**Figure 4.16.** A–C) PAM coronal MAP images showing the development of blood vessels at 2, 4, and 6 weeks post-implantation, respectively. D–F) The corresponding OCT coronal MAP images showing the scaffold/tissue construct. The signals from the skin layer were removed from all the OCT images to show the surface of the scaffold more clearly. Arrowheads indicate examples of local increase in pore size over time due to degradation of the scaffold.

Figure 4.17, A–C, shows co-registered 3D depictions of the vasculature (in red) and the scaffold/tissue construct (in green). The growth of a neovasculature into the scaffold started prior to week 4, as revealed by co-localization of the blood vessels and the pores on the surface of the scaffold (Figure 4.17, B and C, marked by arrowheads). Figure 4.17, D–F, shows the corresponding co-registered B-scan images (transverse plane) at the positions indicated by the dotted lines in Figure 4.17, A–C, respectively. Several layers of the pores close to the surface of the scaffold could be clearly resolved in the OCT images. Blood vessels were seen to gradually develop over time from the surrounding tissue into the interior of the scaffold. Some vessels could reach a depth of more than 1 mm at week 6 (Figure 4.17F). In these images, OCT signals from the skin were removed to clearly show the surface of the scaffold [151].

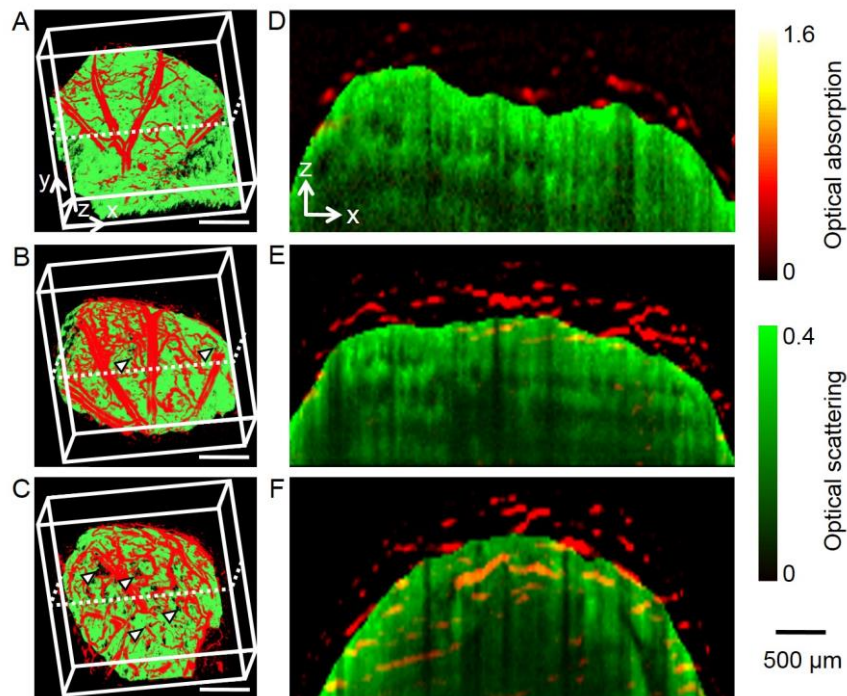


**Figure 4.17.** A–C) Co-registered 3D depictions of the vasculature (red) and scaffold/tissue construct (green) at 2, 4, and 6 weeks post-implantation, respectively. Arrowheads indicate the growth of neovasculature into the pores of the scaffold (scale bars: 500 μm). D–F) Co-registered B-scan images at the planes indicated by dotted lines in (A–C), respectively, showing the gradual

*inward growth of blood vessels into the inner pores of the scaffold. The signals from the skin layer were removed from all the OCT images to clearly show the boundaries between the blood vessels outside and inside the scaffold.*

#### 4.5.2. AR-PAM of Neovascularization

For the OR-PAM subsystem, it was difficult to image deeply into the scaffold due to strong optical scattering. Therefore, the same group of mice was also monitored by AR-PAM at an excitation wavelength of 570 nm at 1, 2, 4 and 6 weeks post-implantation (Figure 4.18).

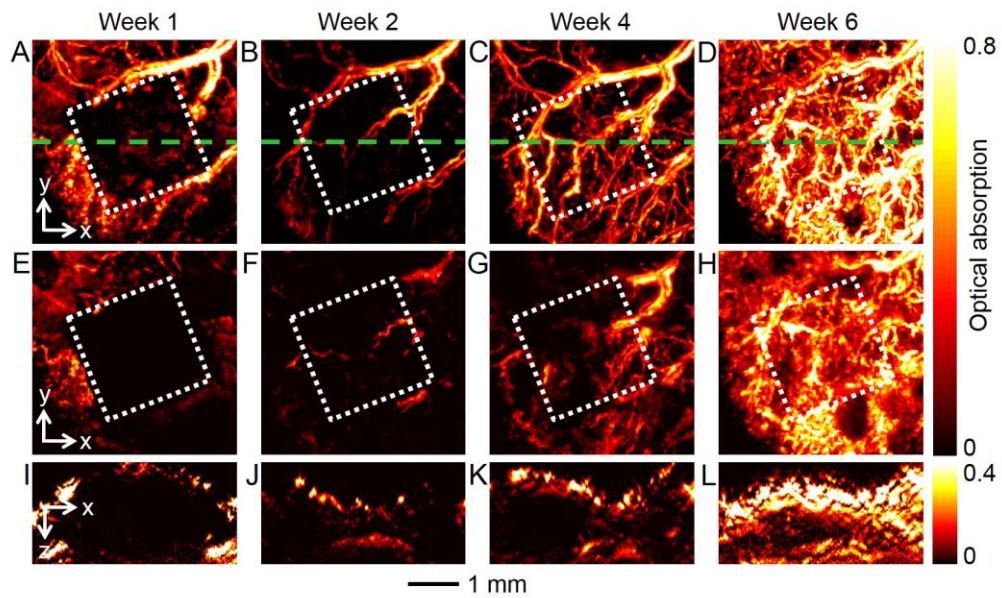


**Figure 4.18.** Chronological AR-PAM images revealing the development of neovasculture in an inverse opal scaffold with a pore size of 200  $\mu\text{m}$ . A–D) PAM coronal MAP images without removing the signals from the skin layer on top of the scaffold at 1, 2, 4, and 6 weeks post-implantation, respectively. E–H) Corresponding MAP images after removal of the signals from the skin layer on top of the scaffold. I–L) Corresponding B-scan images at planes marked by the green dashed lines in (A–D), respectively. The dotted square in each image indicates the area where the scaffold resided.

At 1 week post-implantation, the area of the scaffold (indicated by the white dotted square) could be clearly resolved due to the absence of blood vessels (Figure 4.18A). The scaffold could be better resolved in Figure 4.18E after removal of the signals from the skin (around 150  $\mu\text{m}$  in thickness) using an algorithm similar to what was used for the OCT images [151]. As shown by Figure 4.18, B–D, the neovasculature developed gradually over time, consistent with the observations by OR-PAM depicted in Figure 4.17, A–C. These blood vessels not only grew on top of the implanted scaffold but also penetrated into the scaffold, as shown by the images in Figure 4.18, F–H, where the signals from the skin layer have been removed from the 3D PAM data. In addition, B-scan images (Figure 4.18, I–L) at the indicated positions (green dotted lines in Figure 4.18, A–D) show increase both in signal intensity and number of blood vessels in the central regions, confirming the inward growth of a neovasculature into the inner pores of the scaffold.

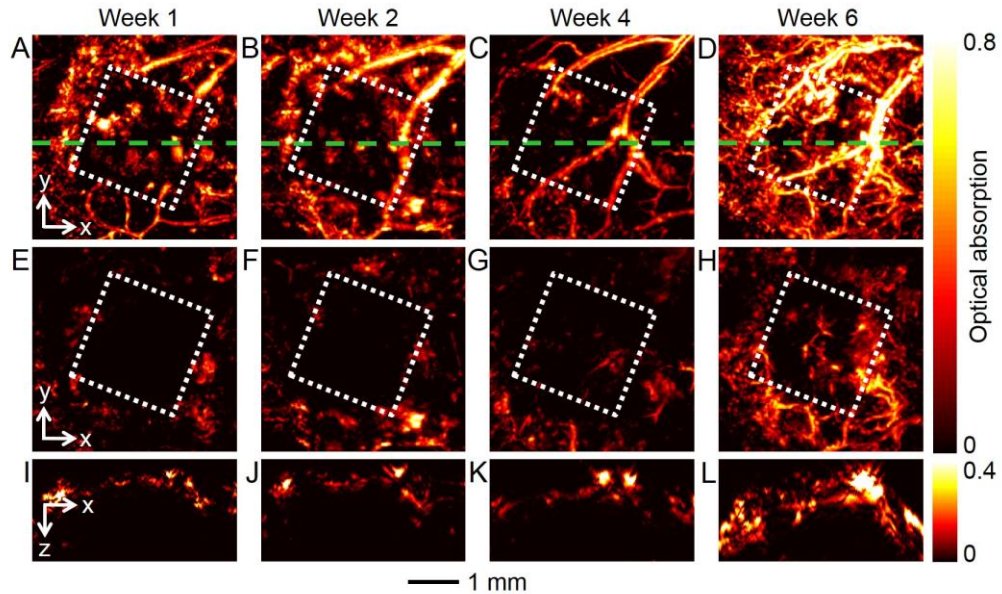


**Figure 4.19.** Chronological AR-PAM images revealing the development of neovasculature in an inverse opal scaffold with a pore size of 80  $\mu\text{m}$ . A–D) PAM coronal MAP images without removing the signals from the skin layer on top of the scaffold at 1, 2, 4, and 6 weeks post-

*implantation, respectively. E–H) Corresponding MAP images after removal of the signals from the skin layer on top of the scaffold. I–L) Corresponding B-scan images at planes marked by the green dashed lines in (A–D), respectively. The dotted square in each image indicates the area where the scaffold resided.*

To further demonstrate the capability of our imaging modality PLGA inverse opal scaffolds with a uniform pore size of 80  $\mu\text{m}$  were implanted into the ears of a new group of mice. The mice were then non-invasively monitored by AR-PAM at 1, 2, 4 and 6 weeks post implantation (Figure 4.19). As shown in the images where the signals from the skin layer had been removed from the 3D PAM data, the neovasculature essentially did not efficiently regenerate into the scaffold region until week 4 (Figure 4.19, E–G). Even by week 6 (Figure 4.19H), there were significantly fewer blood vessels inside the scaffold and they took up much smaller areas than those inside the scaffold with a pore size of 200  $\mu\text{m}$  (Figure 4.18H). The corresponding B-scan images also show much fewer blood vessels inside the scaffold (Figure 4.19, I–L).

In a parallel group, the mice with implanted PLGA inverse opal scaffolds (200  $\mu\text{m}$  and 80  $\mu\text{m}$  in pore size) were sacrificed and subjected to histology analyses at the same time points as the PAM imaging. Figure 4.20, A–C, shows typical hematoxylin and eosin stained sections from the center (200–800  $\mu\text{m}$  below the surface) of the scaffolds with a pore size of 200  $\mu\text{m}$  at 2, 4 and 6 weeks post-implantation, respectively. A few blood vessels (indicated by arrowheads) with small diameters could be observed starting at week 2 (Figure 4.20A), and they grew both in number and area over time (Figure 4.20, B–C). By contrast, for scaffolds with a pore size of 80  $\mu\text{m}$ , only a limited number of blood vessels with small total areas could be observed even at week 6 (Figure 4.20, E–G). These observations were qualitatively consistent with the PAM images (Figures 4.18 and 4.19).

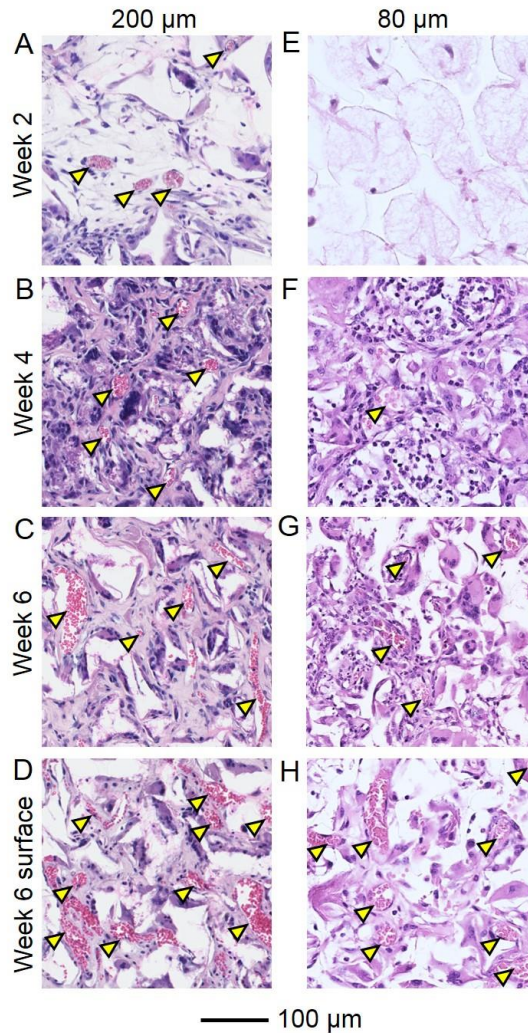


**Figure 4.20.** A–H) Hematoxylin and eosin stained sections of the explanted scaffolds with a pore size of (A–D) 200  $\mu\text{m}$  and (E–H) 80  $\mu\text{m}$  post-implantation at (A, E) 2 weeks, (B, F) 4 weeks and (C, D, G, H) 6 weeks. Sections in (A–C, E–G) were obtained from the central region (200–800  $\mu\text{m}$  below surface) of the scaffolds, while sections in (D, H) were obtained from a plane close to the surface (0–100  $\mu\text{m}$ ). Arrowheads denote blood vessels.

Figure 4.21, A and B, shows quantifications of normalized vessel area as a function of time calculated from both histology and PAM data for the scaffolds with pore sizes of 200  $\mu\text{m}$  (Figure 4.21A) and 80  $\mu\text{m}$  (Figure 4.21B), respectively. The area of blood vessels at each time point was normalized against that of the scaffolds with a pore

size of 80  $\mu\text{m}$  at week 2. The PAM results show that the normalized vessel areas for the scaffolds with a pore size of 200  $\mu\text{m}$  was 2.0–3.5 times larger than those of the scaffolds with a pore size of 80  $\mu\text{m}$  over a period of 6 weeks, which correlated well with the histology analyses.

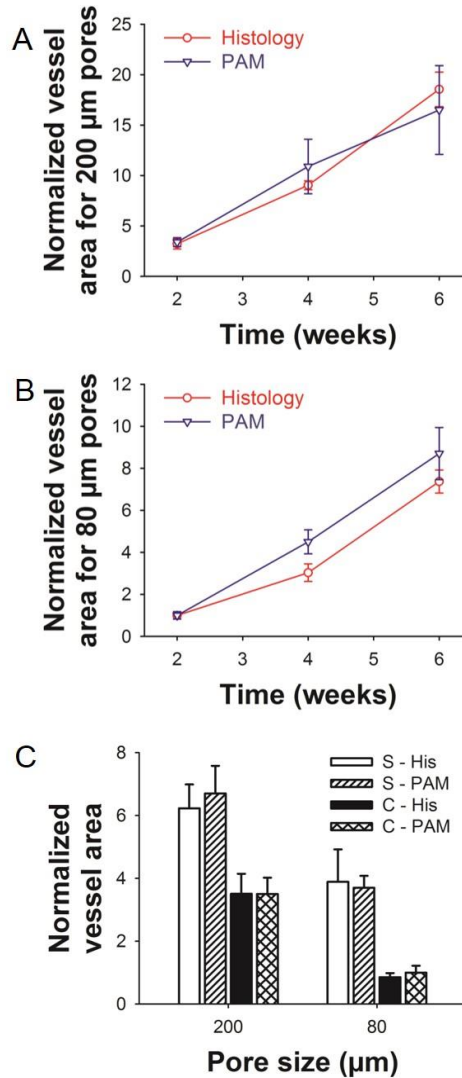


**Figure 4.21.** A, B) Normalized vessel area calculated from both PAM data and histology for scaffolds with a pore size of (A) 200  $\mu\text{m}$  and (B) 80  $\mu\text{m}$ . C) A comparison of the blood vessel area in the scaffolds at planes close to the surface and in the central region of the scaffolds 6 weeks post implantation. S: surface; C: center; His: histology. All the results were presented as mean  $\pm$  standard error ( $n = 3$ ).

I further examined the development of neovasculature close to the surface (0–100  $\mu\text{m}$ ) of the scaffold from the PAM data (Figure 4.20, D and H). In both type of scaffolds, there were vessels with large areas, and the vessel areas were estimated to be about 1.9 times and 3.7 times larger than those in the central region of the scaffolds with pore sizes of 200  $\mu\text{m}$  and 80  $\mu\text{m}$ , respectively (Figure 4.21C). Similar results were obtained by analyzing the histology data (Figure 4.21, A–C). These observations also correlated well with the previous study where only the invasive histology techniques were adopted to investigate the effect of pore size of the PLGA inverse opal scaffolds on neovascularization *in vivo* (see Chapter 3, Section 3.3) [107].

It should be pointed out that, for histology analyses used here, the blood vessel areas were calculated using the data from hematoxylin and eosin stained tissue/scaffold sections. Blood vessels were identified from the presence of RBCs surrounded with a continuous layer of (vascular) cells [96]. Although such a method cannot distinguish different types of vessels by specific markers as with immunostaining (*e.g.*, CD31 and Von Willebrand factor for endothelial cells in capillaries [152, 153], and  $\alpha$ -smooth muscle actin for smooth muscle cells in arterioles [154]), the results could be directly compared with those obtained by PAM. The reason is that PAM detects hemoglobin in RBCs in all types of blood vessels including those newly formed (with RBCs but without blood flow), and therefore the blood vessel areas calculated from PAM volumetric data were essentially the areas of RBCs, which should match better with those derived from histology images with simply hematoxylin and eosin staining.

#### **4.6. Photoacoustic Microscopy of Scaffold Degradation *in vitro* and *in vivo***

Besides characterization of cells/tissues in 3D scaffolds, often it is equally desirable to study the scaffolds themselves. For example, when a biodegradable scaffold is used, it is necessary to quantitatively know the degradation profile of such a scaffold.

In spite of its importance and many years of research, it is still a challenge to measure the degradation profile of a scaffold as the current method has to rely on the measurement of mass loss across multiple samples. In addition to its invasive nature, the assay is also labor-intensive and requires one to sacrifice large numbers of samples or animals. To address this issue, several imaging techniques have been explored for non-invasive assessment of the degradation profiles of a scaffold. For example, Hollister and co-workers have shown the capability to track the degradation of a poly(1,8-octanediol-*co*-citrate) scaffold using ultrasound elasticity imaging [155]. Edelman and co-workers have utilized fluorescence imaging to track the erosion of a poly(ethylene glycol)/dextran or collagen scaffold [156]. Although these authors were able to quantify overall changes to the scaffold from the collected images, it was impossible to observe alterations to the fine structures of the scaffold due to limited resolution of the imaging modalities (typically, a few hundred micrometers in lateral dimensions). As a result, new imaging techniques with high spatial resolution and deep penetration depth still need to be developed for non-invasively assessing the degradation of 3D scaffolds both *in vitro* and *in vivo*.

As described above, PAM can achieve scalable spatial resolution with desired penetration of up to centimeter-scale for biological structures, while maintaining consistent optical absorption contrasts [38, 39]. Inspired by these convenient features of PAM, here I have further extended its capability to non-invasively tracking, both *in vitro* and *in vivo*, of the degradation of PLGA inverse opal scaffolds doped with a contrast agent, such as MTT formazan [157].

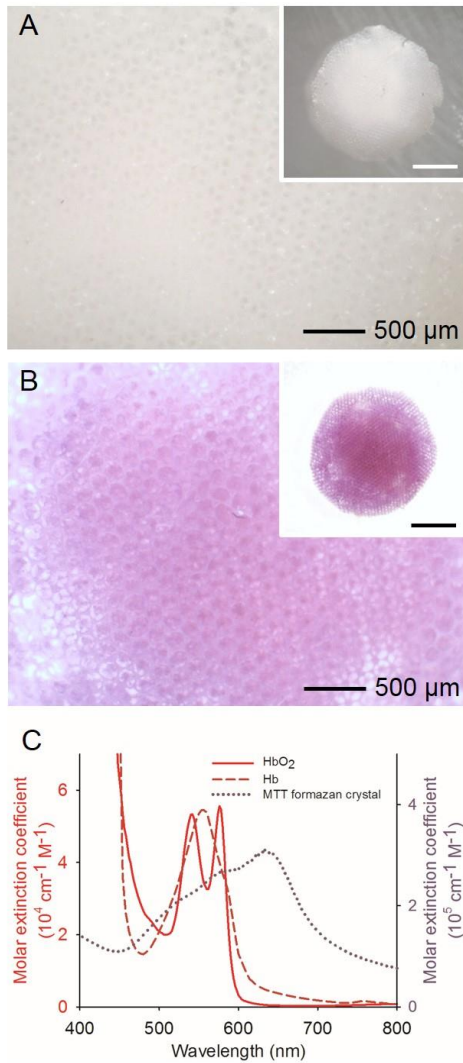


**Figure 4.22.** A, B) Reflective optical micrographs showing (A) a pristine PLGA inverse opal scaffold and (B) a PLGA inverse opal scaffold after doping with MTT formazan to render it purple in color. C) UV-vis spectra of hemoglobin, deoxy-hemoglobin, and MTT formazan crystals.

I used a mixture (in equal mass) of two types of PLGAs with lactide-to-glycolide ratios of 50:50 and 75:25, respectively, in order to achieve an intermediate degradation kinetics (approximately 10–20 weeks *in vitro*) [35, 36]. PLGA inverse opal scaffolds with a uniform pore size of 180 μm were used. Typically, a pristine PLGA inverse opal scaffold wetted and filled with water is translucent white and barely absorbs visible light

(Figure 4.22A). To generate contrast for PAM, the scaffold was doped with MTT formazan (a mass ratio of 1:60 to PLGA) during the fabrication process, which rendered the scaffold purple in color (Figure 4.22B). MTT formazan was chosen as a contrast agent for the following reasons: *i*) formazan is relatively nontoxic [158]; *ii*) MTT formazan crystals have strong absorbance covering the spectral range of approximately 490–700 nm at half maximum, distinct from the absorption of hemoglobin or deoxy-hemoglobin (Figure 4.22C); *iii*) the addition of MTT formazan caused no alteration to the degradation behavior of a PLGA scaffold (Figure 4.23); *iv*) due to its strong hydrophobicity, MTT formazan could hardly leak out from the scaffolds over the 6-week period tested, or the actual amount released was negligible compared to the amount encapsulated (Figure 4.24), and thus enabling accurate quantification.

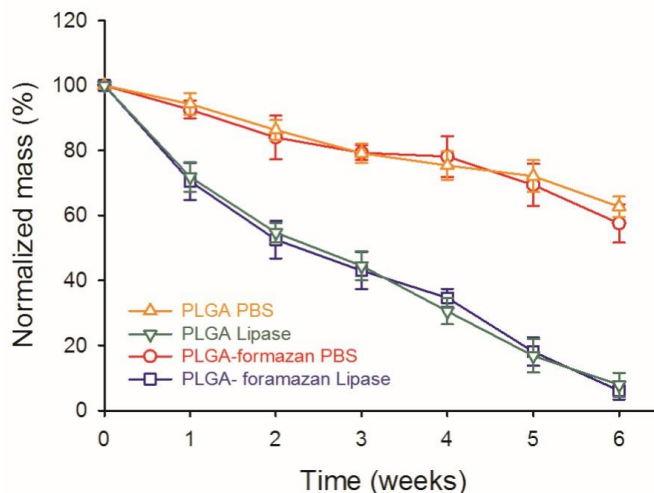


**Figure 4.23.** Degradation of pristine and MTT formazan-doped PLGA inverse opal scaffolds in PBS solutions in the presence and absence of lipase, respectively, as measured by the mass loss assay. The addition of MTT formazan did not alter the degradation behaviors of the scaffolds.

The scaffolds doped with MTT formazan were then subjected to PAM imaging. In order to demonstrate the capability of PAM to track the morphological changes of the

scaffolds, the degradation of the PLGA inverse opal scaffolds was examined under two different conditions: a normal condition in plain PBS, and an *in vivo* mimicry condition in PBS supplemented with 0.025 wt.% lipase. Lipase was chosen because it is secreted in the body naturally upon certain stimulations, such as the implantation of biomaterials [159, 160]. Lipase could specifically cleave the ester groups in PLGA, therefore expediting the degradation of the polymer so that a prominent contrast between the two groups can be easily observed.

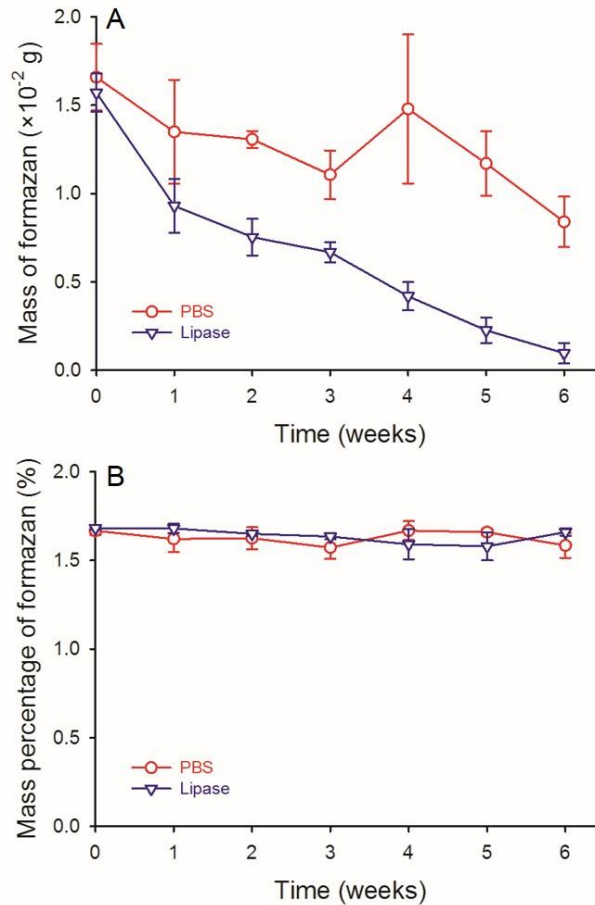


**Figure 4.24.** A) The change in the mass of MTT formazan as a function of degradation time for the scaffolds in PBS, in the absence and presence of lipase, respectively. B) The change in the mass percentage of MTT formazan relative to the scaffolds as a function of degradation time of the scaffolds in PBS solutions, in the absence and presence of lipase, respectively.

Using an OR-PAM which had a lateral resolution of approximately 5  $\mu\text{m}$  and a penetration depth of approximately 1 mm in highly scattering soft tissues [126], I was able to efficiently follow changes to the fine structure of a scaffold during its degradation. Figure 4.25 shows PAM coronal MAP images of the scaffolds, which are color-coded by depth of maximum from blue (surface) to red (bottom). From these images, one could not only clearly observe the uniform pores on the surface of a scaffold, but also the uniform windows connecting them to the pores underneath. The scaffold in plain PBS only showed minor changes to the structures during the 6-week period, mainly caused by shrinkage (Figure 4.25, A–D). By contrast, the addition of lipase induced remarkably accelerated degradation of the scaffold (Figure 4.25, E–H; and I–L, magnified views). The reduction in the overall size of the scaffold became apparent at week 2. The scaffold was largely disrupted at week 4, with large holes appearing in the bulk of the scaffold, and the scaffold had almost completely degraded by week 6.

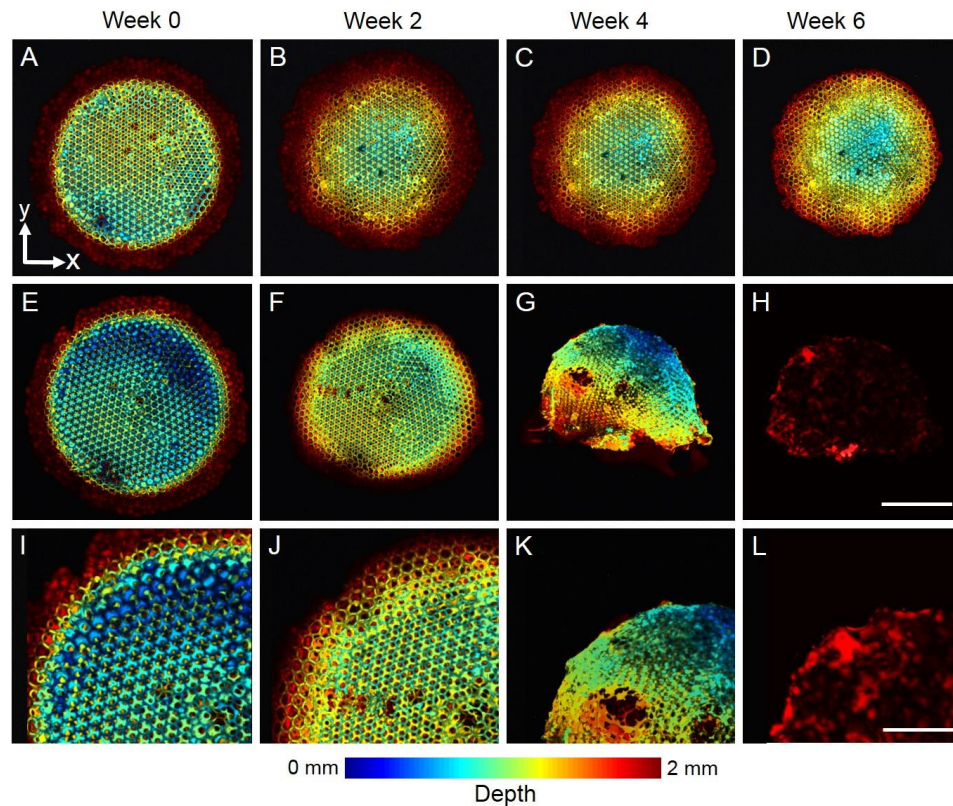


**Figure 4.25.** A–H) OR-PAM coronal MAP images showing the inward degradation of a PLGA inverse opal scaffold immersed in (A–D) plain PBS and (E–H) PBS containing 0.025 wt.% lipase at 37 °C for a period up to 6 weeks. The medium was changed every day. Scale bar: 2 mm. I–L) Magnified views showing the top-left corner of the images in (E–H), respectively. Scale bar: 1 mm. The images are color-coded by depth of maximum.

PAM could be further used to quantitatively analyze the degradation of the scaffolds in addition to resolving their structural changes. To demonstrate this capability, I used an AR-PAM with a deeper penetration depth of approximately 3 mm in soft tissues, at the expense of reducing the lateral resolution to approximately 45  $\mu\text{m}$  [37]. The same groups of inverse opal scaffolds were monitored by AR-PAM for 6 weeks at an excitation wavelength of 638 nm (Figure 4.26, A and B).

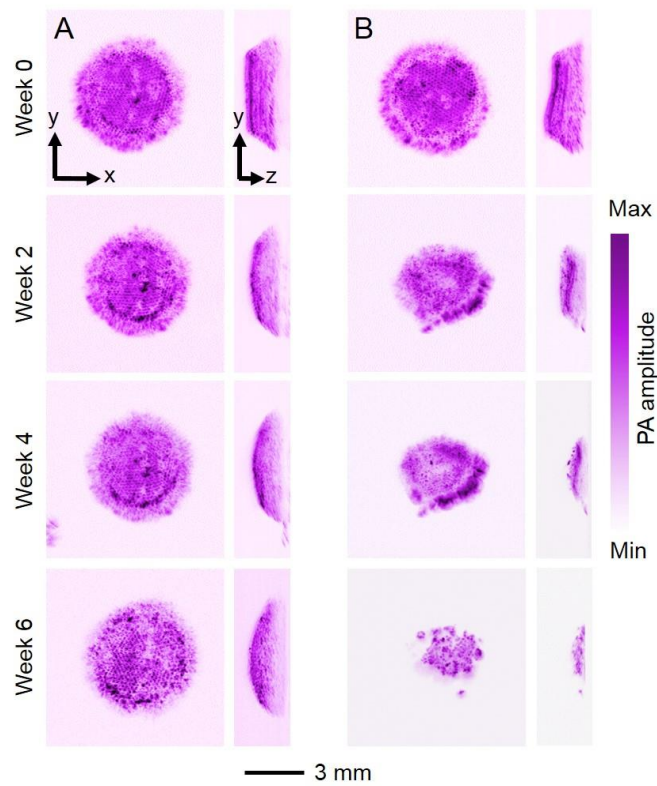


**Figure 4.26.** AR-PAM coronal (left row) and sagittal (right row) MAP images showing the degradation of a PLGA inverse opal scaffold immersed in (A) plain PBS and (B) PBS containing 0.025 wt.% lipase at 37 °C for a period of up to 6 weeks. The medium was changed every day.

Similar to the OR-PAM results, the scaffolds in plain PBS did not show remarkable structural changes other than slightly reduced diameter and thickness. By contrast, those in lipase-containing PBS had almost completely degraded by week 6.

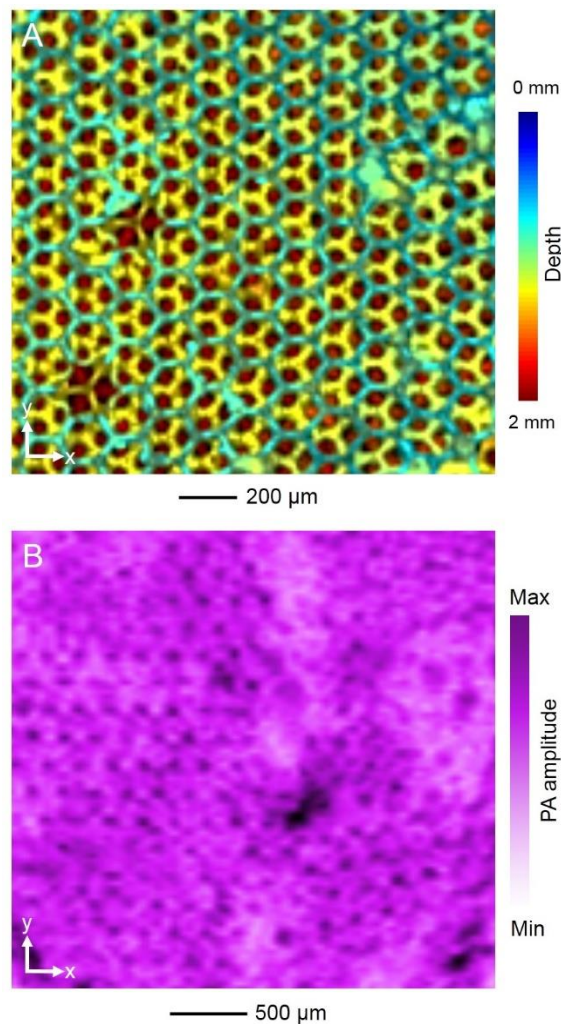


**Figure 4.27.** A) OR-PAM and B) AR-PAM coronal MAP images at higher magnification of a PLGA inverse opal scaffold doped with MTT formazan. The images are color-coded by depth of maximum and amplitude of maximum, respectively.

Comparing the images obtained by OR-PAM and AR-PAM, it could be observed that while OR-PAM could reveal the fine details of the structure of a scaffold (Figure 4.27A), at a lateral resolution of approximately 45  $\mu\text{m}$  for AR-PAM, the porous structure of an inverse opal scaffold was still discernible (Figure 4.27B). Despite its lower resolution, by using the AR-PAM volumetric data, it was able to more accurately quantify the degradation of the scaffolds (by mass) over time: the scaffolds in plain PBS had degraded about 40% by week 6, and lipase had induced about 90% degradation for the scaffolds during the same period of time (Figure 4.28A). The quantification results obtained using PAM data correlated well with those measured from similar scaffolds using the conventional invasive mass loss assay (Figure 4.28B).

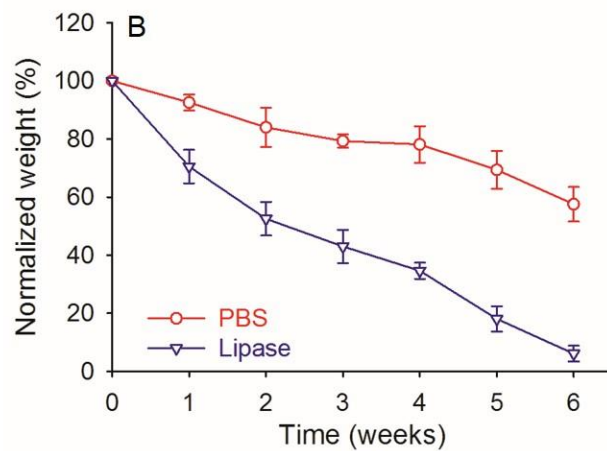
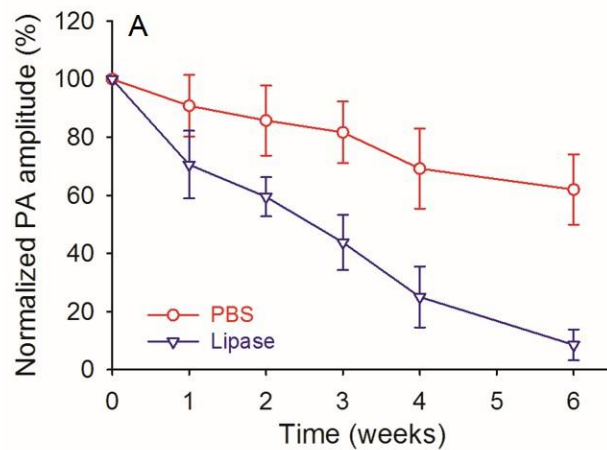


**Figure 4.28.** A) Quantification of the degradation using PAM volumetric data. B) Quantification of the degradation in PBS in the absence and presence of lipase, respectively, using the conventional mass loss assay, which showed profiles similar to what were obtained from PAM.

More significantly, besides *in vitro* analyses, PAM could be used to track the degradation of the scaffolds *in vivo*. In a typical study, the PLGA inverse opal scaffolds doped with MTT formazan were implanted in mouse ears (one scaffold per ear per mouse) [150], and monitored using dual wavelength AR-PAM. Figure 4.29, A–D, shows coronal PAM MAP images of an individual scaffold in the same mouse ear at weeks 0, 1, 3, and 6 post implantation, respectively, at a wavelength of 638 nm. Similar to *in vitro* analysis, the structural changes to the scaffold could be detected without interference from blood vessels thanks to the limited optical absorption of hemoglobin at the chosen wavelength. The diameter of the scaffold decreased from about 5 mm to about 2.5 mm over a period of 6 weeks, together with a decrease in photoacoustic amplitude. Using the PAM volumetric data, it was estimated that the scaffolds had degraded about 90% by week 6 (Figure 4.29E), very similar to the results obtained from the invasive mass loss assay (about 94%, Figure 4.29E). By switching to a wavelength of 578 nm, it was able to then acquire images of both the scaffold and the vasculature because hemoglobin also had strong absorption at this wavelength. After subtracting the signals from the scaffold, the single component of blood vessels with minimum interference from the scaffold was obtained (Figure 4.30).

Figure 4.31, A–D, shows co-registered 3D depictions of blood vessels (in red) and the scaffold (in green) at weeks 0, 1, 3, and 6 post implantation. The degradation of the scaffold and the remodeling of blood vessels within the mouse ear could be identified at the same time. Figure 4.31, E–H, shows the corresponding B-scan images at the positions indicated by the dotted lines in Figure 4.31, A–D, respectively. The thickness of the scaffold decreased from about 1.5 mm at week 0 to about 0.8 mm at week 6, and some

blood vessels were observed to develop into the void space of the scaffold. Moreover, the area of the blood vessels was quantifiable using the PAM volumetric data [150].

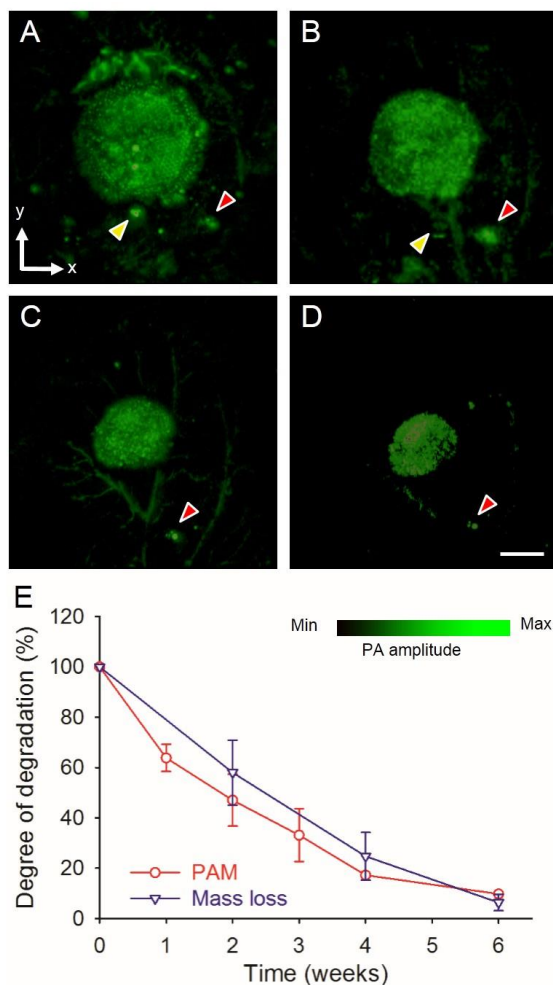


**Figure 4.29.** A–D) AR-PAM coronal MAP images taken from the same PLGA inverse opal scaffold implanted in the ear of a nude mouse at weeks 0, 1, 3, and 6 post implantation, respectively. The arrowheads indicate small pieces of the scaffold that likely came off during the surgery, and their slight changes in position and orientation relative to the main scaffold at different time points could be attributed to the activity of the mouse. Scale bar: 2 mm. E) Comparison of the degradation of scaffolds as a function of time obtained from the same scaffold using PAM and from different scaffolds using the conventional mass loss assay.

It should be noted that, some signals from outside the scaffold area were observed from regions outside the scaffold within the first week of implantation (Figure 4.29A),

which could be attributed small pieces of the scaffold that came off during the surgery process (the scaffold was held by a pair of tweezers and then inserted into the subcutaneous pocket on the ear). These pieces gradually disappeared or were reduced in size in the course of degradation (Figure 4.31, E–H, arrowheads). Across different time points, some of these small pieces could experience changes in position and orientation relative to the main scaffold due to the activity of the mouse. Interestingly, while the native vessels should not generate any intense photoacoustic signals at a wavelength of 638 nm, a few vessels were detected at weeks 0 through 6 (Figure 4.29, B and C). This phenomenon was likely related to the clearance, via the lymphatic system, of MTT formazan released from the scaffold itself or the broken pieces as they were undergoing degradation. As a result, only a few vessels close to the scaffold were visible. However, further studies are needed to clarify this issue.

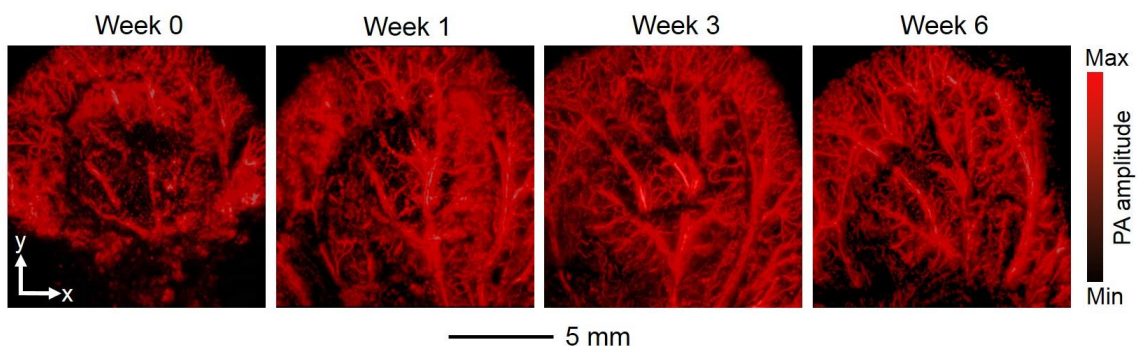


**Figure 4.30.** AR-PAM coronal MAP images showing the remodeling of blood vessels around the PLGA inverse opal scaffold (the same piece) in the ear of a nude mouse at weeks 0, 1, 3, and 6 post implantation.

Such technique using multiscale PAM to non-invasively track the degradation of individual biomaterial scaffolds may find widespread applications in assisting the analyses of biomaterial-tissue interactions in conjunction with the assessment of other *in vivo* vascular parameters. Besides the mass loss measurement as described in this report,

information on molecular degradation of a scaffold can also be potentially obtained by directly conjugating dye molecules within the repeating units of the polymer material.

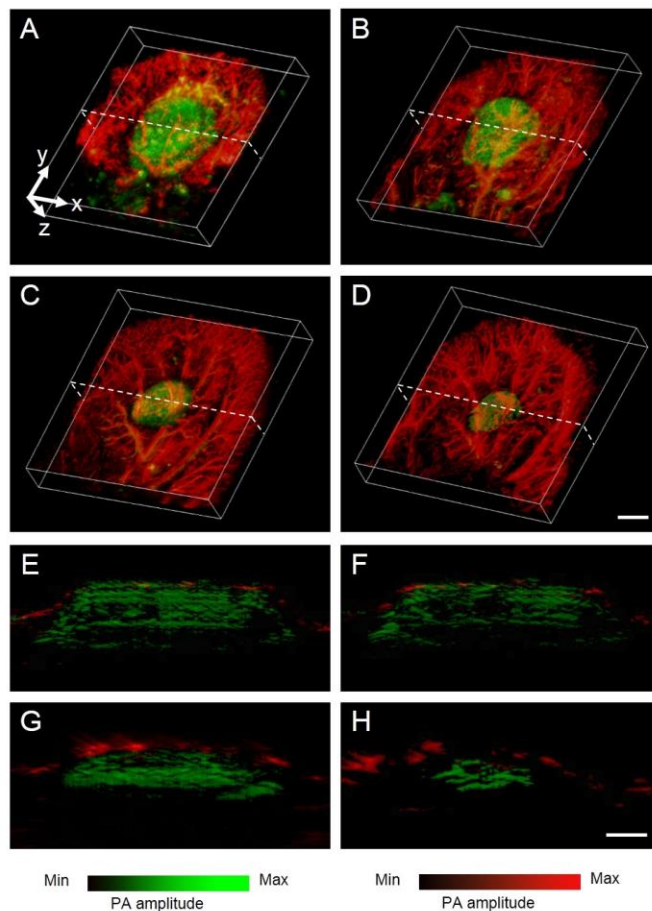


**Figure 4.31.** A–D) Co-registered 3D reconstruction images showing the degradation of a PLGA inverse opal scaffold (the same piece) and the remodeling of the vasculature simultaneously. Scale bar: 2 mm. E–H) Co-registered B-scan images at the dotted planes indicated in (A–D), respectively, showing the inward growth of blood vessels into the bulk of the scaffold. Scale bar: 1 mm.

It should be mentioned that PAM (or photoacoustic tomography, PAT) can achieve much greater penetration depth than pure optical imaging modalities, typically on the scale of a few centimeters [161-163]. While such a penetration depth may suffice the

needs for small laboratory animals or near surface regions, assessment of implants at deep depths in large animals or human objects using PAM might still be difficult. In addition, due to its principle of operation that PAM is based on optical/ultrasonic imaging, bony or air-filled tissues cannot be effectively imaged using such a modality. Despite these two major limitations, I still consider the technique to be a great tool that may eventually become an enabling procedure in analyzing biomaterial-tissue interactions in small animals or surface regions in conjunction with the assessment of other *in vivo* vascular parameters in a completely non-invasive manner.

#### 4.7. Summary

PAT/PAM is expected to find broad applications in imaging 3D scaffold-based samples for regenerative medicine. PAT can even resolve structures in biological tissues as deep as about 7 cm at the expense of decreasing lateral resolution [161-163], which may be sufficient to fit the ultimate goal of engineering tissues with large volumes, at least for *in vitro* evaluations or *in vivo* investigations of implants close to the surface regions. Functional PAM can also be performed to derive other important parameters (*e.g.*, flow velocity [164, 165], oxygen saturation [121, 166], oxygen partial pressure [166], and metabolic rate of oxygen [167]) of the neovasculature.

PAT/PAM still has multiple technical challenges. For high-speed multi-contrast PAM based on spectroscopy, high-sensitivity acoustic arrays and high-repetition lasers with fast wavelength-tuning at each scan position must be developed. Multiscale PAT bridges the gap of a complex biological system between the microscopic and macroscopic domains through consistent optical absorption contrasts. Thus, an integrated single PAT system with a broad range of switchable resolutions and penetration depths is of great interest [168]. It is expected that further advancement of this fast-growing

imaging modality will find wide applications in tissue engineering and regenerative medicine, especially when thick scaffold/tissue constructs are involved.

## **4.8. Experimental**

### **4.8.1. Materials and Chemicals**

Gelatin (type A, from porcine skin), Span® 80, and toluene were all obtained from Sigma-Aldrich and used as-received for the fabrication of the gelatin microspheres with uniform sizes. PLGA (lactide:glycolide = 75:25,  $M_w = 66,000\text{--}107,000$ ) and 1,4-dioxane were also obtained from Sigma-Aldrich and used as received for the fabrication of the scaffolds. All of the chemicals for the preparation of 10xSBF were purchased from Sigma-Aldrich and used as received. The water used in all fabrications was obtained by filtrating through a set of cartridges (Millipore). The PVC tubes and glass microcapillary tubes were purchased from VWR International. Syringe needles were obtained from BD Biosciences.

### **4.8.2. Preparation of PLGA Inverse Opal Scaffolds**

The PLGA inverse opal scaffolds with a uniform pore size of 200  $\mu\text{m}$  were fabricated as described in Chapters 2 and 3 [49, 53, 59, 85, 107, 130, 138, 144, 150, 157]. For the degradation project, a mixture (in equal mass) of two types of PLGAs with lactide-to-glycolide ratios of 50:50 and 75:25, respectively, were dissolved in 1,4-dioxane (30 wt.%), together with MTT formazan (0.5 wt.%) and used as the infiltration agent, while all the other procedures were maintained the same [157].

### **4.8.3. Melanoma Cell Culture in the Inverse Opal Scaffolds**

Prior to cell seeding, the scaffolds were wetted and sterilized by immersion in a mixture of ethanol (70 vol.%) and water for 2 h, washed with PBS (Invitrogen) three

times and stored in PBS until use.

B16.F10 melanoma cells were obtained from the Tissue Culture and Support Center at the Washington University School of Medicine. The cells were maintained in a DMEM (Invitrogen) supplemented with 10 vol.% heat-inactivated FBS (ATCC) and 1 vol.% P/S (Invitrogen). The cells were seeded into each scaffold using a spinner flask (Corning) at 65 rpm for 2 h in an incubator. The cell-seeded scaffolds were then washed and cultured in a spinner flask with the same culture medium, except that DMEM free of phenol red was used to reduce possible signal interference during PAM imaging. The cultures were kept in an incubator at 37 °C under a humidified atmosphere containing 5% CO<sub>2</sub>, and the medium was changed every other day.

NIH/3T3 mouse fibroblasts (CRL-1658), MG63 human osteoblasts (CRL-1427), HepG2 human hepatoma cells (HB-8065), SK-BR-3 human breast cancer cells (HTB-30), and U87-MG human brain glioblastoma cells (HTB-14) were all obtained from ATCC. The cells were maintained in the corresponding culture medium according to the vendor's instructions at 37 °C and 5% CO<sub>2</sub>. Rat bone marrow stromal cells were obtained from Prof. Thomopoulos' laboratory at Washington University School of Medicine. The cells were maintained in  $\alpha$ -MEM (Invitrogen) supplemented with 20 vol.% heat-inactivated FBS (ATCC) and 1 vol.% P/S (Invitrogen) at 37 °C and 5% CO<sub>2</sub>.

Prior to cell seeding, cover glasses (Fisher Scientific, Pittsburgh, PA) and scaffolds were sterilized with a mixture of ethanol (70 vol.%) and water for 2 h, washed with PBS (Invitrogen) three times and stored in culture medium until use. In the case of cover glasses, 24-well plates were used, and cells were seeded at a density of  $5 \times 10^4$  per well. The cells were incubated for 12 h before MTT staining. In the case of scaffolds, about  $2 \times 10^5$  cells were used to seed into each scaffold using a spinner flask (Corning) at 65 rpm for 2 h. The cell-seeded scaffolds were then transferred into a 12-well plate (not treated for tissue culture, BD Biosciences; 1 scaffold per well) and cultured in the culture medium. DMEM (Invitrogen) free of phenol red was used to reduce possible signal

interference during PAM imaging. All cultures were kept in an incubator at 37 °C in a humidified atmosphere containing 5% CO<sub>2</sub> and the media were changed every other day.

For cell invasion experiment, monolayers of fibroblasts were formed in each well of a 24-well plate. The scaffolds were carefully placed in the wells (one per well) on top of the cell monolayers. The culture was kept in still, and culture media were not changed during the entire 7-day culture period.

The protocol for the culture of mouse ESCs was identical to what was described previously [169]. RW4 mouse ESCs were obtained from Prof. Gottlieb's lab at Washington University School of Medicine and cultured in culture flasks coated with gelatin (Sigma-Aldrich). To maintain their undifferentiated state, 1000 U/mL LIF (Chemicon) and 10<sup>-4</sup> M BME (Invitrogen) were added into the medium. Cells were cultured in a complete medium consisting of DMEM supplemented with 10 vol.% newborn calf serum (Sigma-Aldrich), 10 vol.% FBS (Invitrogen), and 0.3 mM of each of the following nucleosides: adenosine, guanosine, cytosine, thymidine, and uridine (Sigma-Aldrich), and passaged every 2–3 days.

MC3T3-E1 mouse preosteoblasts (ATCC) were maintained in  $\alpha$ -MEM (Invitrogen) supplemented with 10 vol.% FBS (ATCC) and 1 vol.% P/S (Invitrogen) in an incubator. The culture medium was replaced every other day. Approximately 5 × 10<sup>5</sup> cells were used to seed into each scaffold, using a spinner flask (Corning) at 70 rpm for 2–3 h. The scaffolds were transferred to the wells (one scaffold per well) of a 12-well plate (non-tissue culture treated, BD Biosciences), rinsed once with PBS (Invitrogen), and 1 mL of culture medium was then added into each well.

#### **4.8.4. Staining**

Cells were incubated with 5 mg/mL MTT solution in PBS (40  $\mu$ L/well in culture medium to a final concentration of 0.05 wt./vol.%) for 3 h at 37 °C. This concentration and the incubation parameters were used in all experiments unless otherwise specified.

When f-actin staining was needed, the cells were briefly fixed with a 4 vol.% formaldehyde (Sigma-Aldrich) solution in PBS for 5 min, washed with PBS and further incubated with Alexa 568-phalloidin (Invitrogen) for 20 min at RT, followed by another PBS washing.

For colorimetric immunostaining for f-actin, the cell/scaffold constructs were first incubated in a streptavidin-biotin blocking solution (Vector Laboratories, Burlingame, CA) for 15 min, and then permeabilized in PBS containing 1.5 wt.% bovine serum albumin (BSA) and 0.1 vol.% Triton X-100. The cells were incubated in sequence with biotin-phalloidin (1:20 dilution, Biotium, Hayward, CA) for 30 min, streptavidin-HRP (1:100 dilution, Invitrogen) for 1 h, and ImmPACT DAB peroxidase substrate (Vector Laboratories) for 2–5 min. The cells were rinsed with water three times between any adjacent incubation sessions.

#### **4.8.5. Cell Proliferation Assay**

Cell proliferation was measured at desired time points post cell seeding using the MTT assays. Typical assays were carried out in 12-well plates: 40  $\mu$ L of MTT (Invitrogen) solution in PBS (5 mg/mL) was added to each well and incubated at 37 °C for 3 h and the culture media were withdrawn. Then 1 mL of 1-propanol (Sigma-Aldrich) was then added to each well to completely dissolve the formazan crystals throughout the scaffold. Absorbance was measured at 560 nm using a spectrophotometer (Infinite 200, TECAN).

#### **4.8.6. Cell Viability Test**

Cell viability was investigated using LIVE/DEAD<sup>®</sup> staining kit (Invitrogen) according to the manufacturer's instruction. Briefly, cells were incubated in PBS containing 2  $\mu$ M calcein AM and 4  $\mu$ M ethidium homodimer at 37 °C for 30 min, rinsed with PBS once, and then observed with a fluorescence microscope (Olympus).

#### **4.8.7. Animals and Histology**

All animal experiments were performed in accordance with protocols approved by the Washington University Department of Comparative Medicine and the Animal Studies Committee. Athymic nude mice 4–5 weeks old were obtained from Harlan and housed under specific pathogen-free conditions in the animal facility at Washington University. All the scaffolds were sterilized in a mixture of ethanol (70 vol.%) and water for at least 2 h prior to implantation. The scaffolds were then implanted subcutaneously in the ears of the mice [150]. Briefly, animals in all groups were anesthetized by administration of gaseous isoflurane (2 vol.%, Butler Inc.) and aseptically prepared. One parasagittal incision was made on the top side of the ear of each animal approximately 0.5 cm to the head. Subcutaneous pockets were created lateral to the incision by using blunt dissection. One scaffold was inserted into the subcutaneous pocket (one scaffold per mouse). The skin incision was then closed with 9-0 Ethilon suture (Ethicon) and secured using GLUture topical tissue adhesive (Abott Laboratories). At pre-determined time points post-implantation, the scaffolds were explanted, fixed in a 3.7 vol.% formaldehyde (Sigma-Aldrich) solution in PBS, dehydrated in a graded ethanol series (70–100 vol.% in water), embedded in paraffin and sectioned (5  $\mu\text{m}$  in thickness). The samples were stained with hematoxylin and eosin and observed under Nanozoomer (Hamamatsu).

#### **4.8.8. Degradation of Inverse Opal Scaffolds**

For *in vitro* experiments, inverse opal scaffolds immersed in 5 mL of either PBS or PBS containing 0.025 wt.% lipase (Sigma-Aldrich) at 37  $^{\circ}\text{C}$ . The medium was changed every day. One group of scaffolds was fixed onto glass slides using a small amount of epoxy (one scaffold per slide), and was subjected to non-invasive PAM imaging, while the scaffolds in the other group were used for mass loss measurement. Briefly, three scaffolds were removed from the medium each week, washed thoroughly

with water, and allowed to dry. The mass of each dry scaffold was measured using a microbalance (Cahn C-30), then, each scaffold was dissolved in 0.2 mL 1,4-dioxane, and absorbance at 562 nm was obtained by a spectrophotometer (Infinite 200, TECAN). The amount of MTT formazan was calculated according to a calibration curve. For *in vivo* experiments, one group of implanted scaffolds was monitored non-invasively using PAM, and the scaffolds in the other group were used for mass loss measurement. Three scaffolds were explanted each week and freeze-dried. Each scaffold/tissue construct was dissolved in dichloromethane, and the insoluble parts were removed by centrifugation. The dichloromethane solution containing dissolved PLGA was freeze-dried and the mass was measured using a microbalance. To determine the background mass caused by soluble tissue components, ear tissue samples with approximately the same volume were subjected to the same analysis.

#### **4.8.9. Scanning Electron Microscopy**

SEM (Nova NanoSEM 2300, FEI) was used to characterize both the PLGA inverse opal scaffolds and the morphologies of melanoma cells grown in the scaffolds. Prior to imaging, cells were fixed and samples were dehydrated through a graded ethanol series and sputter-coated with gold for 60 s. Images were taken at an accelerating voltage of 5 kV.

#### **4.8.10. Photoacoustic Microscopy and Signal Processing**

The details of the PAM systems are described in Section 4.2 [37, 123-128]. In a typical process of *in vitro* imaging, scaffolds were removed from the culture medium, placed in a PDMS mold or directly fixed on the bottom of a Petri dish filled with warm PBS (37 °C) containing 1 vol.% P/S, and imaged using PAM whose transducer surface was immersed in PBS for ultrasound coupling. *In vivo* imaging was typically conducted by immobilizing the mouse on a custom-made stage and keeping the mouse anesthetized

by inhalation of gaseous isoflurane (1 vol.%, Butler Inc.). Ultrasonic coupling gel was administered on top of the ear which was then coupled via a plastic wrap membrane to a tank of water, where the transducer surface was immersed. All photoacoustic data were collected and processed by user-defined LabView (National Instruments, Austin, TX), MATLAB (MathWorks, Inc., Natick, MA), or C++ programs.

#### **4.8.11. Statistics**

All the results were presented as mean  $\pm$  standard deviation or mean  $\pm$  standard error for each experimental group. In all cases, 3–4 scaffolds were monitored for *in vitro* PAM imaging, and 3 mice were used for *in vivo* PAM imaging.

## CHAPTER 5

### SUMMARY AND FUTURE DIRECTIONS

#### 5.1. Inverse Opal Scaffolds for Regenerative Medicine

Although inverse opal scaffolds have been around for many years, a considerable amount of their properties and applications still remain uninvestigated. For example, the interactions between the cells and scaffolds stay unclear. According to my own experience, the PLGA inverse opal scaffolds behave differently when cultured with different types of cells. When cells that have smaller sizes and/or do not secrete significant amounts of organic extracellular molecules (*e.g.*, fibroblasts, differentiating preosteoblasts) are cultured in PLGA inverse opal scaffolds with a pore size of around 200  $\mu\text{m}$ , the scaffolds typically maintain their overall size and shape during prolonged culture up to 8 weeks (Figure 5.1A). On the contrary, if the scaffolds are populated by cells that are large in size and/or express strong secretion of extracellular molecules (*e.g.*, undifferentiated MSCs, differentiating myoblasts), the scaffolds will then undergo gradual size shrinkage and shape alteration during culture (Figure 5.1B). Such difference in the morphological evolution of the scaffolds can be attributed to the differential stresses exerted by various types of cells as well as the ECMs they secrete when the cells proliferate and/or differentiate in the pores of the scaffolds.

As stresses caused by cells and the extracellular molecules that they secrete can alter the morphology of the scaffolds, the stiffness of a scaffold itself can, in turn, affect the behavior of the cells. Many previous studies have shown that, stem cells that were either grown on 2D substrates or embedded in 3D gels could be induced to differentiate along different lineages depending on the stiffness of the substrate [170-172]. Stiffer microenvironment induced the stem cells to differentiate into osteocyte-like cells,

whereas the stem cells on substrates with low modulus tended to undergo adipogenesis. However, there lack studies that how the cells would sense and behave when they reside in 3D porous scaffolds, which are as widely used as hydrogels in tissue engineering and regenerative medicine for stem cell culture. To this end, the inverse opal scaffolds with uniform pore sizes would be good model systems for these studies since other potential interferences such as the variations in pore size, window size and interconnectivity, can all be eliminated.

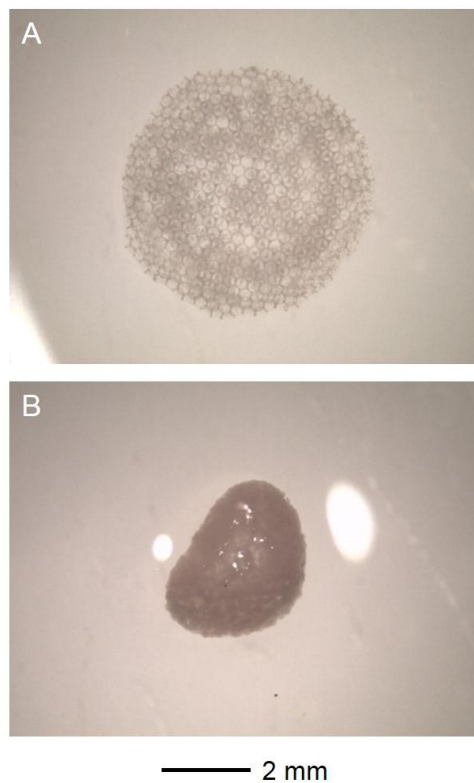


**Figure 5.1.** Reflection optical micrographs showing PLGA inverse opal scaffolds with a pore size of 200  $\mu\text{m}$  after culturing with (A) NIH/3T3 fibroblasts and (B) hMSCs for 4 weeks.

Another interesting investigation would be a complete investigation regarding the effect of size parameters on cell and tissue responses. In Chapter 3, I have shown that the differentiation of preosteoblasts *in vitro* and neovascularization *in vivo* are both affected by the size parameters of PLGA-based inverse opal scaffolds [49, 107]. The potential

behaviors of less terminally differentiated stem cells, however, remain unclear. Although several prior studies have attempted to investigate this issue [173-175], the scaffolds used did not have uniform pore size or structure, thus making their experimental results less conclusive. Inverse opal scaffolds with well-defined structure and uniform pores/windows, by contrast, perfectly solve this “non-uniform” issue.

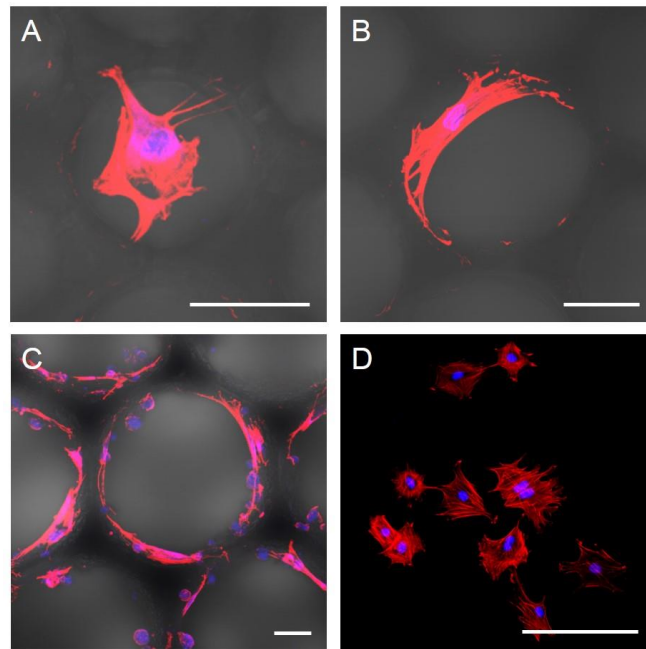


**Figure 5.2.** A–C) Superimposed confocal fluorescence and transmission bright-field optical micrographs showing MSCs grown in PS inverse opal scaffolds with pore sizes of 60, 90, and 250  $\mu\text{m}$ , respectively; scale bars: 50  $\mu\text{m}$ . D) Confocal fluorescence micrograph showing MSCs grown on PS TCPs; scale bar: 100  $\mu\text{m}$ . The f-actin and nuclei of the cells were stained in red and blue, respectively.

As shown in Figure 5.2, MSCs exhibited different morphologies when they were cultured in PS-based inverse opal scaffolds with different pore sizes. While completely 3D stretching was observed for the cells in scaffolds with a pore size similar to that of the cells (60  $\mu\text{m}$ , Figure 5.2A), a partially 3D conformation was adopted by the cells in scaffold with a pore size of 90  $\mu\text{m}$  (Figure 5.2B). The cells essentially experienced a more or less local 2D microenvironment when the pore size of the scaffold became too

large (230  $\mu\text{m}$ , Figure 5.2C), similar to the observation when they were directly cultured on the conventional 2D PS tissue culture plates (TCPs, Figure 5.2D). These variations in the spatial conformation of cells may possibly lead to their distinctive differentiation patterns. Besides 3D conformation of the cells, the difference in the local availability of oxygen, nutrients, bioactive molecules, cell-cell communications, and cell-ECM interactions as determined by the size parameters may also indirectly contribute to the different responses of the progenitor/stem cells [176-180].

In addition to the behavior of stem cells, it is not unreasonable to assume that many terminally differentiated cells are also likely to respond differently when they are cultured in inverse opal scaffolds with different pore sizes. These results, if obtained, are useful in determining the optimal pore size of a scaffold for its application involving a particular cell type. Alternatively, an inverse opal scaffold with a gradient in pore size along one or multiple directions can be applied for interface tissue engineering. One recent demonstration was conducted by Ratner and colleagues, who fabricated bi-layered inverse opal scaffolds made of PHEM for osteochondral tissue engineering [181]. The pores were 38  $\mu\text{m}$  at one side and they were further coated with HAp on the surface to facilitate bone growth, whereas cartilage was induced to develop at the other side with a pore size of 200  $\mu\text{m}$ , with both cell types induced to differentiate from MSCs.

Then, the three sizes of an inverse opal scaffold should be individually adjusted in order to achieve a comprehensive understanding on the potential effect of each of these sizes. Take neovascularization for example, the study I presented in Chapter 3 used PLGA inverse opal scaffolds with four sets of different pore sizes. However, they all had different but proportional surface pore sizes and window sizes to their respective pore sizes. As a result, the three size parameters were multiplexed and it had made the explanation of the results more complicated and to certain degree assumptive. In future studies, only one of the three sizes should be varied while holding the other two constant so that the exact effect of the chosen size could be observed: changing only the surface

pore size would allow one to study the penetration of cells/tissues from the top surface of a scaffold into the bulk; altering only the window size would give information on the migration of cells and the infiltration of tissues through the windows; and changing only the pore size makes it possible to probe parameters such as cell proliferation, migration, and cell-cell communications. After each of these effects has been clearly understood, one would be able to include multiple size parameters of a 3D porous scaffold in an effort to precisely regulate cell/tissue behavior.

While the inverse opal scaffolds can be used for most tissue types where other porous scaffolds have been applied, there are several tissues that are especially suited for the inverse opal scaffolds, and lung is one of them. The alveoli in the lung are interconnected, hollow spheroids with an average diameter of 240  $\mu\text{m}$  (range: 220–250  $\mu\text{m}$ ) [182], which structurally resemble the inverse opal scaffolds. Therefore, inverse opal scaffolds made from materials that are present in the ECM of pulmonary cells (*e.g.*, hyaluronan [183, 184]) can be a good candidate for lung tissue engineering. Similarly, the trabecular bones with a porous structure can also benefit from the use of inverse opal scaffolds made from mineral or mineral/polymer hybrid materials. Despite that in the target tissues to be engineered may not necessarily be homogeneous, again, as emphasized in Chapter 2, the use of inverse opal scaffolds with uniform pore sizes and structure would contribute to the production of engineered tissue constructs with a consistent quality, which is particularly important for clinical applications.

## **5.2. Photoacoustic Microscopy for Regenerative Medicine**

The application of PAM to tissue engineering and regenerative medicine is still at an early stage of development. Since I have already demonstrated the capability of PAM in non-invasively imaging either cells (*in vitro*) or tissues (*in vivo*) in 3D inverse opal scaffolds, future studies should be shifted to functional PAM imaging that can evaluate

the performance of the cell/tissue/scaffold constructs in terms of mechanistic design or clinical relevance.

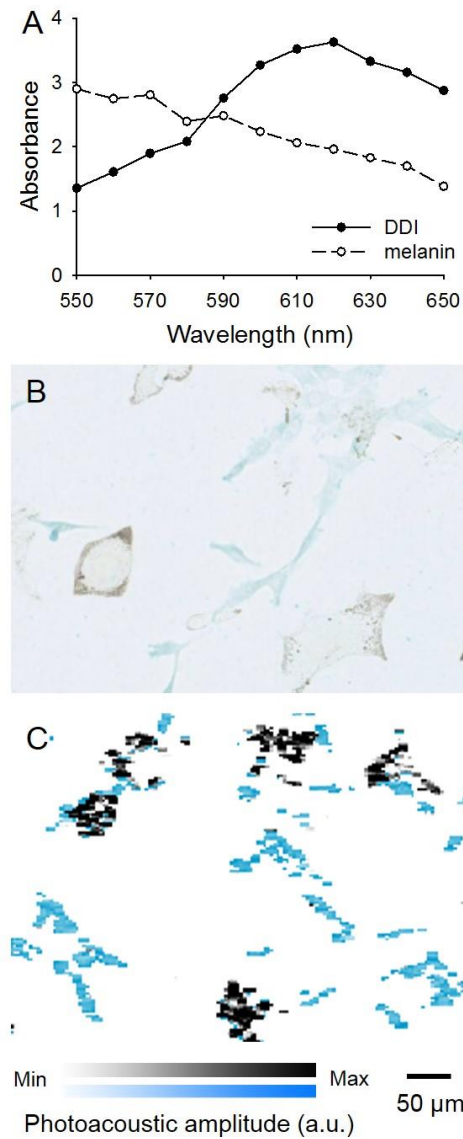


**Figure 5.3.** A) Photoacoustic spectra of DDI and melanin. B) Transmission bright-field optical micrograph showing a co-culture of melanoma cells (black) and 9L/LacZ glioblastoma cells stained by incubating with X-gal (blue). C) OR-PAM MAP image showing separation of the two cell populations in the co-culture. The melanoma cells and 9L/LacZ cells are shown in black in blue colors, respectively.

Until now, only single spectral imaging of individual cell types has been demonstrated [130, 138]. Since PAM is capable of resolving molecules with distinctive absorption spectra, it is also feasible to simultaneously image multiple cells types that contain spectrally different dyes/pigments. In a preliminary study, I demonstrated this capability by taking advantage of the different absorption spectra of melanin and the reaction product of  $\beta$ -galactosidase and 5-bromo-4-chloro-indolyl- $\beta$ -D-galactopyranoside (X-gal), 5,5'-dibromo-4,4'-dichloro-indigo (DDI). The photoacoustic spectra of these two chemical species are shown in Figure 5.3A. While the absorption of melanin monotonically decreased with increasing wavelength, DDI had an absorption peak centered at around 620 nm. Figure 5.3B shows a transmission, bright field optical micrograph of a co-culture of two types of cells, melanoma cells (in black), which naturally expressed dark melanin, and 9L/LacZ glioblastoma cells (in blue), which were transfected with LacZ promoter to express  $\beta$ -galactosidase that stained blue by X-gal. Using dual wavelength PAM at 570 nm and 638 nm, these two types of the cells in a co-culture system could be effectively separated (Figure 5.3C). Such an approach should be generic, and can be applied to essentially all types of cells that are transfected to express biomolecules with distinctive absorption spectra [131, 133-135]. The capability to resolve multiple cell types is essential in functional imaging since the interactions among the cells/tissue can thus be probed without invasive analyses.

Various transfection techniques can also be effectively used for non-invasive, functional PAM analyses of cells and tissues rather than simple imaging purposes. Similar to fluorescent proteins, genes encoding molecules possessing absorption contrasts (*e.g.*,  $\beta$ -galactosidase) could be constructed under certain promoters of stem cells [185, 186]. As a result, once the transfected stem cells are differentiated towards a particular lineage upon stimulation, they would become visible under PAM. Beyond cells, animal strains can also be bred that certain organs/cells (*e.g.*, the vascular system: endothelial cells and pericytes) naturally express contrasts with distinctive absorption spectra. By

doing these, it would reduce or even eliminate the needs for invasive histology and/or immunochemistry, so that the experimental results obtained would be of more physiological relevance.

Another potential application of PAM in tissue engineering and regenerative medicine would take advantage of its capability to obtain parameters related to blood vessels in a label-free manner. Rather than simply imaging the development of blood vessels over time, PAM can further be used to derive other important vascular parameters. For example, while pure PAM observation can detect not only all the mature vessels but also the neovessels that may regress overtime, Doppler-based PAM is able to differentiate vessels with blood flow (perfused, mature) from those without perfusion but are only filled with stationary red blood cells [164, 165]. By doing so, chronological evolution on the maturity of neovessels within a 3D scaffold can be obtained and evaluated. In addition, other parameters such as the flow velocity [164, 165], oxygen saturation [121], oxygen partial pressure [166], and blood oxygen metabolism [167] can all be obtained and collectively used to more accurately evaluate the angiogenic capability of 3D scaffolds upon implantation.

All the above-mentioned PAM imaging of cells/tissues can be combined with simultaneous visualization of scaffolds. Upon further development of PAM, such an approach could potentially become one of standard techniques to analyze cell and tissue functions for thick samples based on 3D scaffold in a completely non-invasive and longitudinal manner.

**APPENDIX A**

**FABRICATION AND SIZE PARAMETERS OF INVERSE OPAL**

**SCAFFOLDS**

<b>Scaffold Material</b>	<b>Templating Microspheres</b>	<b>Annealing Conditions</b>	<b>Window /Pore Size</b>	<b>Infiltration Solution (wt.%)</b>	<b>Surface Pore/Pore Size</b>
<b>PLGA</b>	gelatin	65 °C, 0.5 h	11%		
		65 °C, 3 h	13%		
		65 °C, 5 h	14%		
		80 °C, 3 h	23%		
		100 °C, 3 h	35%		
				10%, 1,4-dioxane	100%
				18%, 1,4-dioxane	85%
				25%, 1,4-dioxane	38%
				30%, 1,4-dioxane	0%
<b>PS</b>	gelatin	65 °C, 3 h	13%		
				20%, 1,4-dioxane	78%
<b>Alginate</b>	PS	110 °C, 4 h	21%		
		120 °C, 4 h	42%		
				2%, 500 mM HAc	90%
<b>Chitosan</b>	PCL	45 °C, 1 h	29%		
				1%, 200 mM HAc	62%

## APPENDIX B

### CATALOG INFORMATION FOR MATERIALS AND CHEMICALS

<b>Polymer</b>	<b>Description</b>	<b>Catalog #</b>
PLGA	lactide:glycolide (75:25), $M_w = 66,000\text{--}107,000$	Sigma P1941
PLGA	lactide:glycolide (50:50), $M_w = 30,000\text{--}60,000$	Sigma P2191
PCL	$M_w = 65,000$	Sigma 181609
PS	$M_w = 350,000$	Sigma 441147
Chitosan	Medium $M_w$ , 75–85% deacetylated	Sigma 448877
Alginate	Medium viscosity	Sigma A2033

## APPENDIX C

### RELATED PAPERS AND MANUSCRIPTS

#### Inverse Opal Scaffolds for Regenerative Medicine

- [1] **Zhang YS**, Choi S-W, Xia Y. Three-Dimensional Scaffolds that Promote Neovascularization: The Importance of Uniformity besides Controlled Release. In preparation, 2013.
- [2] **Zhang YS**, Xia Y. Inverse Opal Scaffolds for Applications in Regenerative Medicine. *Soft Matter*. Submitted, 2013. (Invited opinion article)
- [3] **Zhang YS**, Regan KP, Xia Y. Controlling the Pore Sizes and Related Properties of Inverse Opal Scaffolds for Tissue Engineering Applications. *Macromolecular Rapid Communications*. 2013;34:485-91.
- [4] [Choi S-W, **Zhang YS**], MacEwan MR, Xia Y. Neovascularization in Biodegradable Inverse Opal Scaffolds with Uniform and Precisely Controlled Pore Sizes. *Advanced Healthcare Materials*. 2013;2:145-54. (Equal contribution with the primary author)
- [5] **Zhang YS**, Choi S-W, Xia Y. Modifying the Pores of an Inverse Opal Scaffold with Chitosan Microstructures for Truly Three-dimensional Cell Culture. *Macromolecular Rapid Communications*. 2011;33:296-301. (It was featured on the cover of the journal)
- [6] Choi S-W, **Zhang YS**, Xia Y. Three-Dimensional Scaffolds for Tissue Engineering: The Importance of Uniformity in Pore Size and Structure. *Langmuir*. 2010;26:19001-6.
- [7] [Choi S-W, **Zhang YS**], Thomopoulos S, Xia Y. *In vitro* Mineralization by Preosteoblasts in Poly(DL-lactide-co-glycolide) Inverse Opal Scaffolds Reinforced with Hydroxyapatite Nanoparticles. *Langmuir*. 2010;26:12126-31. (Equal contribution with the primary author)

#### Photoacoustic Microscopy for Regenerative Medicine

- [1] [Cai X, **Zhang YS**], Hu S, Xia Y, Wang LV. Photoacoustic Microscopy of Multiple Cell Types with Differential Gene Expression of Optically Absorbing Chemical Species. In preparation, 2013. (Equal contribution with the primary author)

- [2] **Zhang YS**, Yao J, Zhang C, Wang LV, Xia Y. Optical-Resolution Photoacoustic Microscopy: From Histology Analysis to Three-Dimensional Cell Imaging in Tissue Engineering. In preparation, 2013.
- [3] **Zhang YS**, Cai X, Yao J, Xing W, Wang LV, Xia Y. Non-invasive and *in situ* Characterization of the Degradation of Biomaterial Scaffolds by Photoacoustic Microscopy. *Angewandte Chemie International Edition*. Submitted, 2013.
- [4] Cai X, **Zhang YS**, Xia Y, Wang LV. Photoacoustic Microscopy in Tissue Engineering. *Materials Today*. 2013;16:67-77. (Invited review article)
- [5] [Cai X, **Zhang YS**], Li L, Choi S-W, MacEwan MR, Yao J, Kim C, Xia Y, Wang LV. Investigation of Neovascularization in Three-dimensional Porous Scaffolds *in vivo* by a Combination of Multiscale Photoacoustic Microscopy and Optical Coherence Tomography. *Tissue Engineering Part C: Methods*. 2013;19:196-204. (Equal contribution with the primary author)
- [6] Cai X, Li L, Krumholz A, Guo Z, Erpelding TN, Zhang C, **Zhang YS**, Xia Y, Wang LV. Multi-Scale Molecular Photoacoustic Tomography of Gene Expression. *PLoS ONE*. 2012;7:e43999.
- [7] **Zhang YS**, Xin C, Wang Y, Zhang C, Li L, Choi S-W, Wang LV, Xia Y. Non-invasive Photoacoustic Microscopy of Living Cells Enhanced by Metabolite Dyes in Two and Three Dimensions. *Angewandte Chemie International Edition*. 2011;50:7359-63. (It was selected as a ‘hot’ paper by the editor)
- [8] Yao J, Maslov K, **Zhang YS**, Xia Y, Wang LV. Label-free Oxygen-metabolic Photoacoustic Microscopy *in vivo*. *Journal of Biomedical Optics*. 2011;16:076003.
- [9] Wang Y, Hu S, Maslov K, **Zhang YS**, Xia Y, Wang LV. *In vivo* Integrated Photoacoustic and Confocal Microscopy of Hemoglobin Oxygen Saturation and Oxygen Partial Pressure. *Optical Letters*. 2011;36:1029-31.
- [10] **Zhang YS**, Cai X, Choi S-W, Kim C, Wang LV, Xia Y. Chronic Label-free Volumetric Photoacoustic Microscopy of Melanoma Cells in Three-dimensional Porous Scaffolds. *Biomaterials*. 2010;31:8651-8.

**APPENDIX D**  
**COPYRIGHT INFORMATION**

**Section 2.5.1; Figures 2.2, 2.10–2.13:**

Reprinted (adapted) with permission from Ref. 59. Copyright 2010 American Chemical Society.

**Sections 2.3, 3.2; Figures 2.3 C and D, 2.4–2.5, 3.1–3.3:**

Reprinted (adapted) with permission from Ref. 49. Copyright 2010 American Chemical Society.

**Section 4.3; Figures 4.3C, 4.4–4.6:**

Reprinted (adapted) with permission from Ref. 130. Copyright 2010 Elsevier.

**Section 4.4.1; Figures 4.7–4.13:**

Reprinted (adapted) with permission from Ref. 138. Copyright 2011 Wiley-VCH.

**Section 2.5.2; Figures 2.15–2.17:**

Reprinted (adapted) with permission from Ref. 85. Copyright 2012 Wiley-VCH.

**Sections 2.4, 3.3; Figures 2.7, 3.4–3.10:**

Reprinted (adapted) with permission from Ref. 107. Copyright 2013 Wiley-VCH.

**Sections 4.2, 4.5; Figures 4.1, 4.2, 4.15–4.21:**

Reprinted (adapted) with permission from Ref. 150. Copyright 2013 Mary Ann Liebert.

**Section 2.4; Figures 1.2, 2.8, 2.9:**

Reprinted (adapted) with permission from Ref. 53. Copyright 2013 Wiley-VCH.

**Section 4.6; Figures 4.22–4.31:**

Reprinted (adapted) with permission from Ref. 157. Copyright 2013 Wiley-VCH.

## REFERENCES

- [1] Laurencin CT, Khan YM. Regenerative Engineering. Boca Radon: CRC Press; 2013.
- [2] Langer R, Vacanti JP. Tissue engineering. *Science*. 1993;260:920-6.
- [3] Langer R, Vacanti JP, Vacanti CA, Atala A, Freed LE, Vunjak-Novakovic G. Tissue engineering: biomedical applications. *Tissue Eng*. 1995;1:151-61.
- [4] Khademhosseini A, Vacanti JP, Langer R. Progress in tissue engineering. *Sci Am*. 2009;300:64-71.
- [5] Ma PX. Scaffolds for tissue fabrication. *Mater Today*. 2004;7:30-40.
- [6] Hollister SJ. Porous scaffold design for tissue engineering. *Nat Mater*. 2005;4:518-24.
- [7] Gallego D, Ferrell N, Sun Y, Hansford DJ. Multilayer micromolding of degradable polymer tissue engineering scaffolds. *Mater Sci Eng: C*. 2008;28:353-8.
- [8] Elli K, Dogu Baran A, Sanni V, Sari V, Susanna M, Jari H, *et al*. Direct laser writing and geometrical analysis of scaffolds with designed pore architecture for three-dimensional cell culturing. *J Micromech Microeng*. 2012;22:115016.
- [9] Velev OD, Lenhoff AM. Colloidal crystals as templates for porous materials. *Curr Opin Colloid Interface Sci*. 2000;5:56-63.
- [10] Xia Y, Gates B, Yin Y, Lu Y. Monodispersed colloidal spheres: old materials with new applications. *Adv Mater*. 2000;12:693-713.
- [11] Stein A, Schrodin RC. Colloidal crystal templating of three-dimensionally ordered macroporous solids: materials for photonics and beyond. *Curr Opin Solid State Mater Sci*. 2001;5:553-64.

- [12] Hatton B, Mishchenko L, Davis S, Sandhage KH, Aizenberg J. Assembly of large-area, highly ordered, crack-free inverse opal films. *Proc Natl Acad Sci.* 2010;107:10354-9.
- [13] Ma PX, Choi J-W. Biodegradable polymer scaffolds with well-defined interconnected spherical pore network. *Tissue Eng.* 2001;7:23-33.
- [14] Lee J, Shanbhag S, Kotov NA. Inverted colloidal crystals as three-dimensional microenvironments for cellular co-cultures. *J Mater Chem.* 2006;16:3558-64.
- [15] Stachowiak AN, Irvine DJ. Inverse opal hydrogel-collagen composite scaffolds as a supportive microenvironment for immune cell migration. *J Biomed Mater Res A.* 2008;85A:815-28.
- [16] da Silva J, Lautenschlager F, Kuo C-HR, Guck J, Sivaniah E. 3D inverted colloidal crystals in realistic cell migration assays for drug screening applications. *Integr Biol.* 2011;3:1202-6.
- [17] Peyton SR, Kalcioğlu ZI, Cohen JC, Runkle AP, van Vliet KJ, Lauffenburger DA, *et al.* Marrow-Derived stem cell motility in 3D synthetic scaffold is governed by geometry along with adhesivity and stiffness. *Biotechnol Bioeng.* 2011;108:1181-93.
- [18] Lee J, Cuddihy MJ, Cater GM, Kotov NA. Engineering liver tissue spheroids with inverted colloidal crystal scaffolds. *Biomaterials.* 2009;30:4687-94.
- [19] Lee J, Lilly GD, Doty RC, Podsiadlo P, Kotov NA. *In vitro* toxicity testing of nanoparticles in 3D cell culture. *Small.* 2009;5:1213-21.
- [20] Zhang YS, Xia Y. Formation of embryoid bodies with controlled sizes and maintained pluripotency in three-dimensional inverse opal scaffolds. *Adv Funct Mater.* 2012;22:121-9.
- [21] Marshall AJ, Irvin CA, Barker T, Sage EH, Hauch KD, Ratner BD. Biomaterials with tightly controlled pore size that promote vascular in-growth. *ACS Polym Preprints.* 2004;45:100-1.

- [22] Madden LR, Mortisen DJ, Sussman EM, Dupras SK, Fugate JA, Cuy JL, *et al.* Proangiogenic scaffolds as functional templates for cardiac tissue engineering. *Proc Natl Acad Sci.* 2010. Doi: 10.1073/pnas.1006442107.
- [23] Cuddihy MJ, Kotov NA. Poly(lactic-*co*-glycolic acid) bone scaffolds with inverted colloidal crystal geometry. *Tissue Eng A.* 2008;14:1639-49.
- [24] Osathanon T, Linnes ML, Rajachar RM, Ratner BD, Somerman MJ, Giachelli CM. Microporous nanofibrous fibrin-based scaffolds for bone tissue engineering. *Biomaterials.* 2008;29:4091-9.
- [25] Osathanon T, Giachelli CM, Somerman MJ. Immobilization of alkaline phosphatase on microporous nanofibrous fibrin scaffolds for bone tissue engineering. *Biomaterials.* 2009;30:4513-21.
- [26] Kuo Y-C, Tsai Y-T. Inverted colloidal crystal scaffolds for uniform cartilage regeneration. *Biomacromol.* 2010;11:731-9.
- [27] Kuo Y-C, Tsai Y-T. Heparin-conjugated scaffolds with pore structure of inverted colloidal crystals for cartilage regeneration. *Colloids Surf B.* 2011;82:616-23.
- [28] Kuo Y-C, Chiu K-H. Inverted colloidal crystal scaffolds with laminin-derived peptides for neuronal differentiation of bone marrow stromal cells. *Biomaterials.* 2011;32:819-31.
- [29] Isenhath SN, Fukano Y, Usui ML, Underwood RA, Irvin CA, Marshall AJ, *et al.* A mouse model to evaluate the interface between skin and a percutaneous device. *J Biomed Mater Res A.* 2007;83A:915-22.
- [30] Saul JM, Linnes MP, Ratner BD, Giachelli CM, Pun SH. Delivery of non-viral gene carriers from sphere-templated fibrin scaffolds for sustained transgene expression. *Biomaterials.* 2007;28:4705-16.
- [31] Lee J, Kotov NA. Notch ligand presenting acellular 3D microenvironments for *ex vivo* human hematopoietic stem-cell culture made by layer-by-layer assembly. *Small.* 2009;5:1008-13.
- [32] Fukano Y, Usui ML, Underwood RA, Isenhath S, Marshall AJ, Hauch KD, *et al.* Epidermal and dermal integration into sphere-templated porous poly(2-

- hydroxyethyl methacrylate) implants in mice. *J Biomed Mater Res A*. 2010;94A:1172-86.
- [33] Bryers JD, Giachelli CM, Ratner BD. Engineering biomaterials to integrate and heal: The biocompatibility paradigm shifts. *Biotechnol Bioeng*. 2012;109:1898-911.
- [34] Linnes MP, Ratner BD, Giachelli CM. A fibrinogen-based precision microporous scaffold for tissue engineering. *Biomaterials*. 2007;28:5298-306.
- [35] Lu L, Garcia CA, Mikos AG. *In vitro* degradation of thin poly(DL-lactic-co-glycolic acid) films. *J Biomed Mater Res*. 1999;46:236-44.
- [36] Lu L, Peter SJ, D. Lyman M, Lai H-L, Leite SM, Tamada JA, *et al*. *In vitro* and *in vivo* degradation of porous poly(dl-lactic-co-glycolic acid) foams. *Biomaterials*. 2000;21:1837-45.
- [37] Zhang HF, Maslov K, Stoica G, Wang LV. Functional photoacoustic microscopy for high-resolution and noninvasive *in vivo* imaging. *Nat Biotech*. 2006;24:848-51.
- [38] Wang LV. Multiscale photoacoustic microscopy and computed tomography. *Nat Photon*. 2009;3:503-9.
- [39] Wang LV, Hu S. Photoacoustic Tomography: *In vivo* imaging from organelles to organs. *Science*. 2012;335:1458-62.
- [40] Wang X, Ku G, Wegiel MA, Bornhop DJ, Stoica G, Wang LV. Noninvasive photoacoustic angiography of animal brains *in vivo* with near-infrared light and an optical contrast agent. *Opt Lett*. 2004;29:730-2.
- [41] Song KH, Kim C, Cobley CM, Xia Y, Wang LV. Near-infrared gold nanocages as a new class of tracers for photoacoustic sentinel lymph node mapping on a rat model. *Nano Lett*. 2009;9:183-8.
- [42] Boundy RH. Styrene: its polymers, copolymers, and derivatives. New York: Reinhold Publishing Corporation; 1952.

- [43] Lok KP, Ober CK. Particle size control in dispersion polymerization of polystyrene. *Can J Chem.* 1985;63:209-16.
- [44] Stöber W, Fink A, Bohn E. Controlled growth of monodisperse silica spheres in the micron size range. *J Colloid Interface Sci.* 1968;26:62-9.
- [45] Chen S-L, Dong P, Yang G-H. The size dependence of growth rate of monodisperse silica particles from tetraalkoxysilane. *J Colloid Interface Sci.* 1997;189:268-72.
- [46] Wang X-D, Shen Z-X, Sang T, Cheng X-B, Li M-F, Chen L-Y, *et al.* Preparation of spherical silica particles by Stöber process with high concentration of tetraethyl-orthosilicate. *J Colloid Interface Sci.* 2010;341:23-9.
- [47] Choi S-W, Cheong IW, Kim J-H, Xia Y. Preparation of uniform microspheres using a simple fluidic device and their crystallization into close-packed lattices. *Small.* 2009;5:454-9.
- [48] Fukano Y, Knowles NG, Usui ML, Underwood RA, Hauch KD, Marshall AJ, *et al.* Characterization of an *in vitro* model for evaluating the interface between skin and percutaneous biomaterials. *Wound Repair Regen.* 2006;14:484-91.
- [49] Choi S-W, Zhang YS, Xia Y. Three-dimensional Scaffolds for Tissue Engineering: The Importance of Uniformity in Pore Size and Structure. *Langmuir.* 2010;26:19001-6.
- [50] Zhang YS, Choi S-W, Xia Y. Three-Dimensional Scaffolds that Promote Neovascularization: The Importance of Uniformity besides Controlled Release. 2013.
- [51] Jain RK, Au P, Tam J, Duda DG, Fukumura D. Engineering vascularized tissue. *Nat Biotechnol.* 2005;23:821-3.
- [52] Koike N, Fukumura D, Gralla O, Au P, Schechner JS, Jain RK. Tissue engineering: creation of long-lasting blood vessels. *Nature.* 2004;428:138-9.
- [53] Zhang YS, Regan KP, Xia Y. Controlling the pore sizes and related properties of inverse opal scaffolds for tissue engineering applications. *Macromol Rapid Commun.* 2013;34:485-91.

- [54] Mazur S, Beckerbauer R, Buckholz J. Particle size limits for sintering polymer colloids without viscous flow. *Langmuir*. 1997;13:4287-94.
- [55] Nawaz Q, Rharbi Y. Various modes of void closure during dry sintering of close-packed nanoparticles. *Langmuir*. 2009;26:1226-31.
- [56] Park SH, Gates B, Xia Y. A three-dimensional photonic crystal operating in the visible region. *Adv Mater*. 1999;11:462-6.
- [57] Gates B, Park SH, Xia Y. Tuning the photonic bandgap properties of crystalline arrays of polystyrene beads by annealing at elevated temperatures. *Adv Mater*. 2000;12:653-6.
- [58] Abrusci C, Martín-González A, Amo AD, Catalina F, Bosch P, Corrales T. Chemiluminescence study of commercial type-B gelatines. *J Photochem Photobiol A*. 2004;163:537-46.
- [59] Choi S-W, Zhang YS, Thomopoulos S, Xia Y. *In vitro* mineralization by preosteoblasts in poly(DL-lactide-co-glycolide) inverse opal scaffolds reinforced with hydroxyapatite nanoparticles. *Langmuir*. 2010;26:12126-31.
- [60] Rezwani K, Chen Q, Blaker J, Boccaccini AR. Biodegradable and bioactive porous polymer/inorganic composite scaffolds for bone tissue engineering. *Biomaterials*. 2006;27:3413-31.
- [61] Banaszkiwicz PA, Kader DF. Postgraduate orthopaedics: the candidate's guide to the FRCS (Tr and Orth) examination. Cambridge: Cambridge University Press; 2012.
- [62] Bertazzo S, Bertran C. Morphological and dimensional characteristics of bone mineral crystals. *Key Eng Mater*. 2006;309:3-6.
- [63] El-Ghannam A, Ducheyne P, Shapiro IM. Porous bioactive glass and hydroxyapatite ceramic affect bone cell function *in vitro* along different time lines. *J Biomed Mater Res*. 1997;36:167-80.
- [64] Kokubo T, Kim H-M, Kawashita M, Nakamura T. Bioactive metals: preparation and properties. *J Mater Sci Mater Med*. 2004;15:99-107.

- [65] Chesnutt BM, Viano AM, Yuan Y, Yang Y, Guda T, Appleford MR, *et al.* Design and characterization of a novel chitosan/nanocrystalline calcium phosphate composite scaffold for bone regeneration. *J Biomed Mater Res A*. 2009;88A:491-502.
- [66] Bigi A, Boanini E, Panzavolta S, Roveri N, Rubini K. Bonelike apatite growth on hydroxyapatite–gelatin sponges from simulated body fluid. *J Biomed Mater Res*. 2002;59:709-15.
- [67] LeGeros RZ. Properties of osteoconductive biomaterials: calcium phosphates. *Clin Orthop Relat Res*. 2002;395:81-98.
- [68] Wei G, Ma PX. Structure and properties of nano-hydroxyapatite/polymer composite scaffolds for bone tissue engineering. *Biomaterials*. 2004;25:4749-57.
- [69] Chou Y-F, Huang W, Dunn JCY, Miller TA, Wu BM. The effect of biomimetic apatite structure on osteoblast viability, proliferation, and gene expression. *Biomaterials*. 2005;26:285-95.
- [70] Jiang T, Abdel-Fattah WI, Laurencin CT. *In vitro* evaluation of chitosan/poly(lactic acid-glycolic acid) sintered microsphere scaffolds for bone tissue engineering. *Biomaterials*. 2006;27:4894-903.
- [71] Tas CA. Synthesis of biomimetic Ca-hydroxyapatite powders at 37 °C in synthetic body fluids. *Biomaterials*. 2000;21:1429-38.
- [72] Tas CA, Bhaduri SB. Rapid coating of Ti6Al4V at room temperature with a calcium phosphate solution similar to 10× simulated body fluid. *J Mater Res*. 2004;19:2742-9.
- [73] Li X, Xie J, Yuan X, Xia Y. Coating electrospun poly( $\epsilon$ -caprolactone) fibers with gelatin and calcium phosphate and their use as biomimetic scaffolds for bone tissue engineering. *Langmuir*. 2008;24:14145-50.
- [74] Li X, Xie J, Lipner J, Yuan X, Thomopoulos S, Xia Y. Nanofiber scaffolds with gradations in mineral content for mimicking the tendon-to-bone insertion site. *Nano Lett*. 2009;9:2763-8.

- [75] Shu R, McMullen R, Baumann MJ, McCabe LR. Hydroxyapatite accelerates differentiation and suppresses growth of MC3T3-E1 osteoblasts. *J Biomed Mater Res A*. 2003;67A:1196-204.
- [76] Goldstein AS, Juarez TM, Helmke CD, Gustin MC, Mikos AG. Effect of convection on osteoblastic cell growth and function in biodegradable polymer foam scaffolds. *Biomaterials*. 2001;22:1279-88.
- [77] Boyan BD, Hummert TW, Dean DD, Schwartz Z. Role of material surfaces in regulating bone and cartilage cell response. *Biomaterials*. 1996;17:137-46.
- [78] Kieswetter K, Schwartz Z, Hummert TW, Cochran DL, Simpson J, Dean DD, et al. Surface roughness modulates the local production of growth factors and cytokines by osteoblast-like MG-63 cells. *J Biomed Mater Res*. 1996;32:55-63.
- [79] Yuan H, Kurashina K, de Bruijn JD, Li Y, de Groot K, Zhang X. A preliminary study on osteoinduction of two kinds of calcium phosphate ceramics. *Biomaterials*. 1999;20:1799-806.
- [80] Wang Y-W, Wu Q, Chen J, Chen G-Q. Evaluation of three-dimensional scaffolds made of blends of hydroxyapatite and poly(3-hydroxybutyrate-co-3-hydroxyhexanoate) for bone reconstruction. *Biomaterials*. 2005;26:899-904.
- [81] Richardson TP, Peters MC, Ennett AB, Mooney DJ. Polymeric system for dual growth factor delivery. *Nat Biotechnol*. 2001;19:1029-34.
- [82] Lee KY, Peters MC, Anderson KW, Mooney DJ. Controlled growth factor release from synthetic extracellular matrices. *Nature*. 2000;408:998-1000.
- [83] Kim MS, Bhang S-H, Yang HS, Rim NG, Jun I, Kim SI, et al. Development of functional fibrous matrices for the controlled release of basic fibroblast growth factor to improve therapeutic angiogenesis. *Tissue Eng A*. 2010;16:2999-3010.
- [84] Burgess WH, Maciag T. The heparin-binding (fibroblast) growth factor family of proteins. *Annu Rev Biochem*. 1989;58:575-602.
- [85] Zhang YS, Choi S-W, Xia Y. Modifying the pores of an inverse opal scaffold with chitosan microstructures for truly three-dimensional cell culture. *Macromol Rapid Commun*. 2012;33:296-301.

- [86] Di Martino A, Sittinger M, Risbud MV. Chitosan: a versatile biopolymer for orthopaedic tissue-engineering. *Biomaterials*. 2005;26:5983-90.
- [87] Tsuruga E, Takita H, Itoh H, Wakisaka Y, Kuboki Y. Pore size of porous hydroxyapatite as the cell-substratum controls BMP-induced osteogenesis. *J Biochem*. 1997;121:317-24.
- [88] Byrne E, Farrell E, McMahon L, Haugh M, O'Brien F, Campbell V, et al. Gene expression by marrow stromal cells in a porous collagen-glycosaminoglycan scaffold is affected by pore size and mechanical stimulation. *J Mater Sci Mater Med*. 2008;19:3455-63.
- [89] Moon JJ, West JL. Vascularization of engineered tissues: approaches to promote angiogenesis in biomaterials. *Curr Top Med Chem*. 2008;8:300-10.
- [90] Quint C, Kondo Y, Manson RJ, Lawson JH, Dardik A, Niklason LE. Decellularized tissue-engineered blood vessel as an arterial conduit. *Proc Natl Acad Sci*. 2011;108:9214-9.
- [91] Tabata Y, Miyao M, Yamamoto M, Ikada Y. Vascularization into a porous sponge by sustained release of basic fibroblast growth factor. *J Biomater Sci Polym Ed*. 1999;10:957-68.
- [92] Sheridan MH, Shea LD, Peters MC, Mooney DJ. Bioabsorbable polymer scaffolds for tissue engineering capable of sustained growth factor delivery. *J Controlled Release*. 2000;64:91-102.
- [93] Perets A, Baruch Y, Weisbuch F, Shoshany G, Neufeld G, Cohen S. Enhancing the vascularization of three-dimensional porous alginate scaffolds by incorporating controlled release basic fibroblast growth factor microspheres. *J Biomed Mater Res A*. 2003;65A:489-97.
- [94] Holder WD, Gruber HE, Roland WD, Moore AL, Culberson CR, Loeb sack AB, *et al*. Increased vascularization and heterogeneity of vascular structures occurring in polyglycolide matrices containing aortic endothelial cells implanted in the Rat. *Tissue Eng*. 1997;3:149-60.
- [95] Rafii S, Lyden D. Therapeutic stem and progenitor cell transplantation for organ vascularization and regeneration. *Nat Med*. 2003;9:702-12.

- [96] Jabbarzadeh E, Starnes T, Khan YM, Jiang T, Wirtel AJ, Deng M, et al. Induction of angiogenesis in tissue-engineered scaffolds designed for bone repair: A combined gene therapy–cell transplantation approach. *Proc Natl Acad Sci.* 2008;105:11099-104.
- [97] Klenke FM, Liu Y, Yuan H, Hunziker EB, Siebenrock KA, Hofstetter W. Impact of pore size on the vascularization and osseointegration of ceramic bone substitutes *in vivo*. *J Biomed Mater Res A.* 2008;85A:777-86.
- [98] Druecke D, Langer S, Lamme E, Pieper J, Ugarkovic M, Steinau HU, et al. Neovascularization of poly(ether ester) block-copolymer scaffolds *in vivo*: long-term investigations using intravital fluorescent microscopy. *J Biomed Mater Res A.* 2004;68A:10-8.
- [99] Bai F, Zhang J, Wang Z, Lu J, Chang J, Liu J, et al. The effect of pore size on tissue ingrowth and neovascularization in porous bioceramics of controlled architecture *in vivo*. *Biomed Mater.* 2011;6:015007.
- [100] Kuboki Y, Jin Q, Takita H. Geometry of carriers controlling phenotypic expression in BMP-induced osteogenesis and chondrogenesis. *J Bone Joint Surg.* 2001;83:S105-S15.
- [101] Dalby MJ, Gadegaard N, Tare R, Andar A, Riehle MO, Herzyk P, et al. The control of human mesenchymal cell differentiation using nanoscale symmetry and disorder. *Nat Mater.* 2007;6:997-1003.
- [102] Hwang NS, Varghese S, Elisseeff J. Controlled differentiation of stem cells. *Adv Drug Delivery Rev.* 2008;60:199-214.
- [103] Ma PX, Zhang R, Xiao G, Franceschi R. Engineering new bone tissue *in vitro* on highly porous poly( $\alpha$ -hydroxyl acids)/hydroxyapatite composite scaffolds. *J Biomed Mater Res.* 2001;54:284-93.
- [104] Bancroft GN, Sikavitsas VI, Mikos AG. Technical note: design of a flow perfusion bioreactor system for bone tissue-engineering applications. *Tissue Eng.* 2003;9:549-54.
- [105] Liu X, Smith LA, Hu J, Ma PX. Biomimetic nanofibrous gelatin/apatite composite scaffolds for bone tissue engineering. *Biomaterials.* 2009;30:2252-8.

- [106] Hing KA. Bone repair in the twenty-first century: biology, chemistry or engineering? *Phil Trans R Soc A*. 2004;362:2821-50.
- [107] Choi S-W, Zhang YS, MacEwan MR, Xia Y. Neovascularization in biodegradable inverse opal scaffolds with uniform and precisely controlled pore sizes. *Adv Healthcare Mater*. 2013;2:145-54.
- [108] Carmeliet P, Jain RK. Angiogenesis in cancer and other diseases. *Nature*. 2000;407:249-57.
- [109] Carmeliet P, Conway EM. Growing better blood vessels. *Nat Biotechnol*. 2001;19:1019-20.
- [110] Carmeliet P. Angiogenesis in health and disease. *Nature Med*. 2003;9:653-60.
- [111] Djonov V, Schmid M, Tschanz SA, Burri PH. Intussusceptive angiogenesis: its role in embryonic vascular network formation. *Circ Res*. 2000;86:286-92.
- [112] Burri PH, Djonov V. Intussusceptive angiogenesis—the alternative to capillary sprouting. *Mol Aspects Med*. 2002;23:1-27.
- [113] Steinbrech DS, Longaker MT, Mehrara BJ, Saadeh PB, Chin GS, Gerrets RP, *et al*. Fibroblast response to hypoxia: the relationship between angiogenesis and matrix regulation. *J Surg Res*. 1999;84:127-33.
- [114] Shotton DM. Confocal scanning optical microscopy and its applications for biological specimens. *J Cell Sci*. 1989;94:175-206.
- [115] Dumas D, Riquelme B, Werkmeister E, Isla ND, Stoltz JF. Multimodality of microscopy imaging applied to cartilage tissue engineering. Amsterdam: IOS Press; 2007.
- [116] Dorsey SM, Lin-Gibson S, Simon CG, Jr. X-ray microcomputed tomography for the measurement of cell adhesion and proliferation in polymer scaffolds. *Biomaterials*. 2009;30:2967-74.
- [117] van Lenthe GH, Hagenmüller H, Bohner M, Hollister SJ, Meinel L, Müller R. Nondestructive micro-computed tomography for biological imaging and

- quantification of scaffold-bone interaction *in vivo*. *Biomaterials*. 2007;28:2479-90.
- [118] Potter K, Sweet DE, Anderson P, Davis GR, Isogai N, Asamura S, *et al*. Non-destructive studies of tissue-engineered phalanges by magnetic resonance microscopy and X-ray microtomography. *Bone*. 2006;38:350-8.
- [119] Peptan IA, Hong L, Xu H, Magin RL. MR assessment of osteogenic differentiation in tissue-engineered constructs. *Tissue Eng*. 2006;12:843-51.
- [120] Mertsching H, Walles T, Hofmann M, Schanz J, Knapp WH. Engineering of a vascularized scaffold for artificial tissue and organ generation. *Biomaterials*. 2005;26:6610-7.
- [121] Zhang HF, Maslov K, Sivaramakrishnan M, Stoica G, Wang LV. Imaging of hemoglobin oxygen saturation variations in single vessels *in vivo* using photoacoustic microscopy. *Appl Phys Lett*. 2007;90:053901-3.
- [122] Kim C, Cho EC, Chen J, Song KH, Au L, Favazza C, *et al*. *In vivo* molecular photoacoustic tomography of melanomas targeted by bioconjugated gold nanocages. *ACS Nano*. 2010;4:4559-64.
- [123] Maslov K, Zhang HF, Hu S, Wang LV. Optical-resolution photoacoustic microscopy for *in vivo* imaging of single capillaries. *Opt Lett*. 2008;33:929-31.
- [124] Hu S, Maslov K, Wang LV. Second-generation optical-resolution photoacoustic microscopy with improved sensitivity and speed. *Opt Lett*. 2011;36:1134-6.
- [125] Zhang C, Maslov K, Wang LV. Subwavelength-resolution label-free photoacoustic microscopy of optical absorption *in vivo*. *Opt Lett*. 2010;35:3195-7.
- [126] Wang Y, Maslov K, Kim C, Hu S, Wang LV. Integrated photoacoustic and fluorescence confocal microscopy. *IEEE Trans Biomed Eng*. 2010;57:2576-8.
- [127] Li L, Maslov K, Ku G, Wang LV. Three-dimensional combined photoacoustic and optical coherence microscopy for *in vivo* microcirculation studies. *Opt Express*. 2009;17:16450-5.

- [128] Maslov K, Stoica G, Wang LV. *In vivo* dark-field reflection-mode photoacoustic microscopy. *Opt Lett*. 2005;30:625-7.
- [129] Jennifer YL, David EF. Melanocyte biology and skin pigmentation. *Nature*. 2007;445:843-50.
- [130] Zhang YS, Cai X, Choi S-W, Kim C, Wang LV, Xia Y. Chronic label-free volumetric photoacoustic microscopy of melanoma cells in three-dimensional porous Scaffolds. *Biomaterials*. 2010;31:8651-8.
- [131] Daniel R, Martin D, Claudio V, Rui M, Norbert P, Reinhard WK, *et al.* Multispectral opto-acoustic tomography of deep-seated fluorescent proteins *in vivo*. *Nat Photon*. 2009;3:412-7.
- [132] Filonov GS, Krumholz A, Xia J, Yao J, Wang LV, Verkhusha VV. Deep-tissue photoacoustic tomography of a genetically encoded near-infrared fluorescent probe. *Angew Chem Int Ed*. 2012;51:1448-51.
- [133] Li L, Zemp RJ, Lungu G, Stoica G, Wang LV. Photoacoustic imaging of lacZ gene expression *in vivo*. *J Biomed Opt*. 2007;12:020504.
- [134] Cai X, Li L, Krumholz A, Guo Z, Erpelding TN, Zhang C, *et al.* Multi-Scale Molecular Photoacoustic Tomography of Gene Expression. *PLoS One*. 2012;7:e43999.
- [135] Krumholz A, VanVickle-Chavez SJ, Yao J, Fleming TP, Gillanders WE, Wang LV. Photoacoustic microscopy of tyrosinase reporter gene *in vivo*. *J Biomed Opt*. 2011;16:080503.
- [136] Jokerst JV, Thangaraj M, Kempen PJ, Sinclair R, Gambhir SS. Photoacoustic imaging of mesenchymal stem cells in living mice via silica-coated gold nanorods. *ACS Nano*. 2012;6:5920-30.
- [137] Zhang YS, Wang Y, Wang L, Wang Y, Cai X, Zhang C, *et al.* Labeling human mesenchymal stem cells with Au nanocages for *in vitro* and *in vivo* tracking by two-photon microscopy and photoacoustic microscopy. *Theranostics*. 2013;3:532-43.

- [138] Zhang YS, Cai X, Wang Y, Zhang C, Li L, Choi S-W, *et al.* Noninvasive photoacoustic microscopy of living cells in two and three dimensions through enhancement by a metabolite dye. *Angew Chem Int Ed.* 2011;50:7359-63.
- [139] Altman FP. Tetrazolium salts and formazans. *Prog histochemistry cytochem.* 1976;9:1-51.
- [140] Mosmann T. Rapid colorimetric assay for cellular growth and survival: Application to proliferation and cytotoxicity assays. *J Immunol Methods.* 1983;65:55-63.
- [141] Seidler E. The tetrazolium-fomazan system: design and histochemistry. *Prog Histochem Cytochem.* 1991;24:1-79.
- [142] Berridge MV, Tan AS. Characterization of the cellular reduction of 3-(4,5-dimethylthiazol-2-yl)-2,5-diphenyltetrazolium bromide (MTT): subcellular localization, substrate dependence, and involvement of mitochondrial electron transport in MTT reduction. *Arch Biochem Biophys.* 1993;303:474-82.
- [143] Kobayashi T. *J-Aggregates.* Singapore: World Scientific Publishing Company; 1996.
- [144] Zhang YS, Yao J, Zhang C, Wang LV, Xia Y. *Histochemistry-enabled cell imaging by optical-resolution photoacoustic microscopy for tissue engineering and biomedical applications.* 2013.
- [145] Yao J, Maslov KI, Puckett ER, Rowland KJ, Warner BW, Wang LV. Double-illumination photoacoustic microscopy. *Opt Lett.* 2012;37:659-61.
- [146] Hofstraat JW. Polymer characterization by fluorescence spectroscopy. In: Craver C, Carraher C, editors. *Applied Polymer Science: 21st Century.* Amsterdam: Elsevier; 2000. p. 829-50.
- [147] Lovett M, Lee K, Edwards A, Kaplan DL. Vascularization strategies for tissue engineering. *Tissue Eng B.* 2009;15:353-70.
- [148] Schmidt C, Bezuidenhout D, Beck M, Van der Merwe E, Zilla P, Davies N. Rapid three-dimensional quantification of VEGF-induced scaffold neovascularisation by microcomputed tomography. *Biomaterials.* 2009;30:5959-68.

- [149] Perng C-K, Wang Y-J, Tsi C-H, Ma H. *In vivo* angiogenesis effect of porous collagen scaffold with hyaluronic acid oligosaccharides. *J Surg Res.* 2011;168:9-15.
- [150] Cai X, Zhang YS, Li L, Choi S-W, MacEwan MR, Yao J, *et al.* Investigation of neovascularization in 3D porous scaffolds *in vivo* by photoacoustic microscopy and optical coherence tomography. *Tissue Eng C.* 2013;13:196-204.
- [151] Zhang HF, Maslov K, Wang LV. Automatic algorithm for skin profile detection in photoacoustic microscopy. *J Biomed Opt.* 2009;14:024050.
- [152] Kalka C, Masuda H, Takahashi T, Kalka-Moll WM, Silver M, Kearney M, *et al.* Transplantation of *ex vivo* expanded endothelial progenitor cells for therapeutic neovascularization. *Proc Natl Acad Sci USA.* 2000;97:3422-7.
- [153] Levenberg S, Golub JS, Amit M, Itskovitz-Eldor J, Langer R. Endothelial cells derived from human embryonic stem cells. *Proc Natl Acad Sci USA.* 2002;99:4391-6.
- [154] L'Heureux N, Dusserre N, Konig G, Victor B, Keire P, Wight TN, *et al.* Human tissue-engineered blood vessels for adult arterial revascularization. *Nature Med.* 2006;12:361-5.
- [155] Kim K, Jeong CG, Hollister SJ. Non-invasive monitoring of tissue scaffold degradation using ultrasound elasticity imaging. *Acta Biomater.* 2008;4:783-90.
- [156] Artzi N, Oliva N, Puron C, Shitreet S, Artzi S, bon Ramos A, *et al.* *In vivo* and *in vitro* tracking of erosion in biodegradable materials using non-invasive fluorescence imaging. *Nat Mater.* 2011;10:704-9.
- [157] Zhang YS, Cai X, Yao J, Wang LV, Xia Y. Non-invasive and *in situ* characterization of the degradation of biomaterial scaffolds by photoacoustic microscopy. *Angew Chem Int Ed.* 2013.
- [158] Scudiero DA, Shoemaker RH, Paull KD, Monks A, Tierney S, Nofziger TH, *et al.* Evaluation of a soluble tetrazolium/formazan assay for cell growth and drug sensitivity in culture using human and other tumor cell lines. *Cancer Res.* 1988;48:4827-33.

- [159] Janousek L, Adamec M, Saudek F, Koznarova R, Boucek P, Lipar K, *et al.* Modulating amylase and lipase secretion in the pancreatic graft by somatostatin administration: preliminary results of a prospective, randomized trial. *Transplantation Proc.* 2004;36:1099-100.
- [160] Ma W-X, Yu T-S, Fan Y-Y, Zhang S-T, Ren P, Wang S-B, *et al.* Time-dependent expression and distribution of monoacylglycerol lipase during the skin-incised wound healing in mice. *Int J Legal Med.* 2011;125:549-58.
- [161] Song KH, Wang LV. Deep reflection-mode photoacoustic imaging of biological tissue. *J Biomed Opt.* 2007;12:060503.
- [162] Kim C, Erpelding TN, Jankovic L, Pashley MD, Wang LV. Deeply penetrating *in vivo* photoacoustic imaging using a clinical ultrasound array system. *Biomed Opt Express.* 2010;1:278-84.
- [163] Wang Y, Erpelding TN, Jankovic L, Guo Z, Robert J-L, David G, *et al.* *In vivo* three-dimensional photoacoustic imaging based on a clinical matrix array ultrasound probe. *J Biomed Opt.* 2012;17:0612081-5.
- [164] Yao J, Maslov KI, Shi Y, Taber LA, Wang LV. *In vivo* photoacoustic imaging of transverse blood flow by using Doppler broadening of bandwidth. *Opt Lett.* 2010;35:1419-21.
- [165] Yao J, Wang LV. Transverse flow imaging based on photoacoustic Doppler bandwidth broadening. *J Biomed Opt.* 2010;15:021304-5.
- [166] Wang Y, Hu S, Maslov K, Zhang Y, Xia Y, Wang LV. *In vivo* integrated photoacoustic and confocal microscopy of hemoglobin oxygen saturation and oxygen partial pressure. *Opt Lett.* 2011;36:1029-31.
- [167] Yao J, Maslov KI, Zhang Y, Xia Y, Wang LV. Label-free oxygen-metabolic photoacoustic microscopy *in vivo*. *J Biomed Opt.* 2011;16:076003-11.
- [168] Xing W, Wang L, Maslov K, Wang LV. Integrated optical-and acoustic-resolution photoacoustic microscopy based on an optical fiber bundle. *Opt Lett.* 2013;38:52-4.

- [169] Xie J, Willerth SM, Li X, Macewan MR, Rader A, Sakiyama-Elbert SE, *et al.* The differentiation of embryonic stem cells seeded on electrospun nanofibers into neural lineages. *Biomaterials*. 2009;30:354-62.
- [170] Discher DE, Janmey P, Wang Y-l. Tissue cells feel and respond to the stiffness of their substrate. *Science*. 2005;310:1139-43.
- [171] Engler AJ, Sen S, Sweeney HL, Discher DE. Matrix elasticity directs stem cell lineage specification. 2006;126:677-89.
- [172] Huebsch N, Arany PR, Mao AS, Shvartsman D, Ali OA, Bencherif SA, *et al.* Harnessing traction-mediated manipulation of the cell/matrix interface to control stem-cell fate. *Nat Mater*. 2010;9:518-26.
- [173] Taqvi S, Roy K. Influence of scaffold physical properties and stromal cell coculture on hematopoietic differentiation of mouse embryonic stem cells. *Biomaterials*. 2006;27:6024-31.
- [174] Oh SH, Kim TH, Im GI, Lee JH. Investigation of pore size effect on chondrogenic differentiation of adipose stem cells using a pore size gradient scaffold. *Biomacromol*. 2010;11:1948-55.
- [175] Im G, II, Ko J-Y, Lee JH. Chondrogenesis of adipose stem cells in a porous polymer scaffold: influence of the pore size. *Cell Transplant*. 2012;21:2397-405.
- [176] Burdick JA, Vunjak-Novakovic G. Engineered microenvironments for controlled stem cell differentiation. *Tissue Eng A*. 2008;15:205-19.
- [177] Dang SM, Gerecht- Nir S, Chen J, Itskovitz- Eldor J, Zandstra PW. Controlled, scalable embryonic stem cell differentiation culture. *Stem Cells*. 2004;22:275-82.
- [178] Reilly GC, Engler AJ. Intrinsic extracellular matrix properties regulate stem cell differentiation. *J biomech*. 2010;43:55-62.
- [179] Dawson E, Mapili G, Erickson K, Taqvi S, Roy K. Biomaterials for stem cell differentiation. *Adv Drug Delivery Rev*. 2008;60:215-28.

- [180] Lutolf MP, Gilbert PM, Blau HM. Designing materials to direct stem-cell fate. *Nature*. 2009;462:433-41.
- [181] Galperin A, Oldinski RA, Florczyk SJ, Bryers JD, Zhang M, Ratner BD. Integrated bi-layered scaffold for osteochondral tissue engineering. *Adv Healthcare Mater*. 2012. Doi: 10.1002/adhm.201200345.
- [182] Ochs M, Nyengaard JR, Jung A, Knudsen L, Voigt M, Wahlers T, *et al*. The number of alveoli in the human lung. *Am J Respir Crit Care Med*. 2004;169:120-4.
- [183] Turino GM, Cantor JO. Hyaluronan in respiratory injury and repair. *Am J Respir Crit Care Med*. 2003;167:1169-75.
- [184] Jiang D, Liang J, Noble PW. Hyaluronan in tissue injury and repair. *Annu Rev Cell Dev Biol*. 2007;23:435-61.
- [185] Chudakov DM, Lukyanov S, Lukyanov KA. Fluorescent proteins as a toolkit for *in vivo* imaging. *Trends Biotechnol*. 2005;23:605-13.
- [186] Hoffman RM. The multiple uses of fluorescent proteins to visualize cancer *in vivo*. *Nat Rev Cancer*. 2005;5:796-806.

## VITA

### YU SHRIKE ZHANG

ZHANG was born in Nanjing, Jiangsu, China in 1986. He attended Jinling High School in Nanjing, Jiangsu, received a B.Eng. in Biomedical Engineering from Southeast University, Nanjing in 2008. He then came to the United States of America and pursued his doctorate with Professor Younan Xia in the Department of Biomedical Engineering at Washington University in St. Louis, St. Louis, Missouri until December 2011, when he relocated with Professor Xia to the Wallace H. Coulter Department of Biomedical Engineering at Georgia Institute of Technology and Emory University to continue his doctoral studies. His research interests include biomaterials, tissue engineering and regenerative medicine, biomedical imaging, drug and cell delivery, cancer theranostics, lab-on-a-chip, and developmental biology. When he is not working on his researches, Mr. Zhang enjoys bird- and nature-watching, traveling, photography, and novel technologies. Website: [sites.google.com/site/shrikezhang](http://sites.google.com/site/shrikezhang)